

Article

Recent Progress on Irradiation-Induced Defect Engineering of Two-Dimensional 2H-MoS₂ Few Layers

Guang-Yi Zhao ^{1,*} , Hua Deng ² , Nathaniel Tyree ³, Michael Guy ³, Abdellah Lisfi ³, Qing Peng ⁴ , Jia-An Yan ⁵, Chungong Wang ⁶ and Yucheng Lan ^{3,*} 

¹ Nuclear Science and Technology Center, School of Physics, Jilin University, Changchun 130012, China

² Department of Chemistry, Morgan State University, Baltimore, MD 21251, USA; Hua.Deng@morgan.edu

³ Department of Physics and Engineering Physics, Morgan State University, Baltimore, MD 21251, USA; natyr1@morgan.edu (N.T.); miguy2@morgan.edu (M.G.); Abdellah.Lisfi@morgan.edu (A.L.)

⁴ Nuclear Engineering and Radiological Sciences, University of Michigan, Ann Arbor, MI 48109, USA; q@qpeng.org

⁵ Department of Physics, Astronomy, and Geosciences, Towson University, Towson, MD 21252, USA; jyan@towson.edu

⁶ School of Optical and Electronic Information, Huazhong University of Science and Technology, Wuhan 430074, China; apcdwang@hust.edu.cn

* Correspondence: zhaogy@jlu.edu.cn (G.Z.); yucheng.lan@morgan.edu (Y.L.); Tel.: +1-443-885-3752 (Y.L.)

Received: 14 January 2019; Accepted: 8 February 2019; Published: 16 February 2019



Abstract: Atom-thick two-dimensional materials usually possess unique properties compared to their bulk counterparts. Their properties are significantly affected by defects, which could be uncontrollably introduced by irradiation. The effects of electromagnetic irradiation and particle irradiation on 2H MoS₂ two-dimensional nanolayers are reviewed in this paper, covering heavy ions, protons, electrons, gamma rays, X-rays, ultraviolet light, terahertz, and infrared irradiation. Various defects in MoS₂ layers were created by the defect engineering. Here we focus on their influence on the structural, electronic, catalytic, and magnetic performance of the 2D materials. Additionally, irradiation-induced doping is discussed and involved.

Keywords: MoS₂; 2D material; irradiation; review

1. Introduction

With the discoveries of zero-dimensional buckyballs in the 1980s [1] and one-dimensional carbon nanotubes in the 1990s [2,3], various nanomaterials have been synthesized and characterized. Their physical and chemical properties are unique compared with counterpart bulks (graphite, diamond, and amorphous carbon) because of size-induced quantum effects, enabling their great potential in various fields. Two-dimensional (2D) graphene was reported in the 2000s [4] and excellent electrical behaviors were claimed. Since then investigations of 2D layers were initialized and rapidly developed in recent decades. At present, the 2D layer family spans conductors (such as graphene), insulators (such as hexagonal boron nitride), and semiconductors. Transition-metal dichalcogenide (TMDC) materials, including MoS₂, WS₂, MoSe₂, and WSe₂, are layered semiconductors and have been fabricated into 2D semiconducting layers. MoS₂ 2D layers have novel potential applications in novel nano-optoelectronics, optical sensors, catalysts, energy storages, and environments. Additionally, MoS₂ 2D layers show thickness-dependent semiconducting behaviors, being the most interesting and important among TMDC 2D layers. Bulk MoS₂ is a semiconductor with an indirect energy band gap of 1.2 eV while mono-layer MoS₂ is a direct band-gap semiconductor with an energy band gap of 1.9 eV

due to 2D quantum confinement. The MoS₂ layers have also important applications in valleytronics—a new type of electronics where information is encoded by wave quantum number of electrons.

MoS₂ low-dimensional materials have been investigated over the past 50 years. MoS₂ few-layers (4–5 layers) were first prepared by a peeling process from bulk crystals in the 1960s [5]. Tribological properties of MoS₂ films have been studied later in a vacuum or dry air as solid lubricants since the 1990s [6,7]. Compared with bulks, the friction coefficient of MoS₂ films was reduced, and the wear life of the films was enhanced. Catalytic properties of MoS₂ nanoparticles [8] and films [9,10] have been investigated from the 1980s. It is believed that edge sites of MoS₂ nanomaterials play important roles in electrochemical and catalytic behaviors. MoS₂ atomically thin materials, especially mono-layer MoS₂, have been widely investigated in recent years because of their sizable direct band gap, high charge-carrier mobility, and excellent mechanical flexibility [11,12]. The materials have potential applications in the next generation flexible electronics [11,13,14], elastic energy storage [12], field-effect transistors [15,16], electronic switches [13], electronic devices such as chemical biosensors [16,17], and optoelectronic devices [18] such as photodetectors and solar cells [19]. It was demonstrated that chemically active defects, such as sulfur vacancies, significantly control or tune their catalytic activities [20], electronic transports [21–23], and optical properties [24].

Various forms of irradiation and particle fluxes modulate the density of sulfur vacancies of chemical-vapor deposition (CVD) grown and mechanically exfoliated MoS₂ sheets, affecting their chemically active defects. Therefore, irradiation effects have been carried out in recent years. Additionally, these MoS₂ devices and sensors have been used in harsh environments, and it is necessary to investigate their tolerance under irradiation. Radiation effects on two-dimensional graphene were recently reviewed [25,26]. Defect engineering and defect-induced properties of other atom-thick mono-layers were summarized as well [26]. The impacts of irradiation on 2H MoS₂ two-dimensional materials are reviewed here.

1.1. MoS₂ 2D Materials

MoS₂ has two main types of natural phases: hexagonal structure (2H type) with the space group of P6₃/mmc (D_{6h}⁴, No. 194) and the trigonal structure (3R type) with the space group of R3m (C_{3v}⁵, No. 160). The 2H phase contains two layers per unit cell, $a = 3.15 \text{ \AA}$ and $c = 12.30 \text{ \AA}$. Similar to graphite, the 2H type crystals can be easily cleaved to form (0001) layers because of weaker van der Waals forces between (0001) layers. The 3R phase contains three layers per unit cell, stacking in rhombohedral symmetry with trigonal prismatic coordination, $a = 3.16 \text{ \AA}$ and $c = 18.33 \text{ \AA}$. A third metastable phase, 1T-MoS₂ with a tetragonal symmetry, was also artificially produced by intercalating 2H-MoS₂ with alkali metals [27–29]. The artificial 1T phase and natural 3R phase are metastable at room temperature and transform to the 2H phase on heating [27] or IR irradiation [30] or microwave irradiation [31]. This work focuses on the 2H MoS₂ phase. 1T and 3R polytypes will not be discussed.

Molybdenum disulfide (2H-MoS₂) is a transition-metal dichalcogenide with a melting point of 2375 °C. The bulk material is chemically stable in dilute acids and oxygen and insoluble in water. Figure 1a shows the crystallographic structure of 2H-MoS₂ bulks. There are two S-Mo-S layers per unit cell stacked in hexagonal symmetry. Each S-Mo-S layer consists of two hexagonal planes of sulfur atoms and an intermediate hexagonal plane of molybdenum atoms. The sandwiched molybdenum atom plane is coordinated through ionic-covalent interactions with the sulfur atoms, forming a stable MoS₂ mono-layer as shown in Figure 1b. The MoS₂ mono-layers are held together by weak van der Waals interactions. The forces between the mono-layers are not very strong [32], and the interatomic forces within a mono-layer are sufficient for thermodynamical stability [33]. Therefore, 2H-MoS₂ has been widely used as a dry lubricant under high temperature due to the microscaled chemical properties.

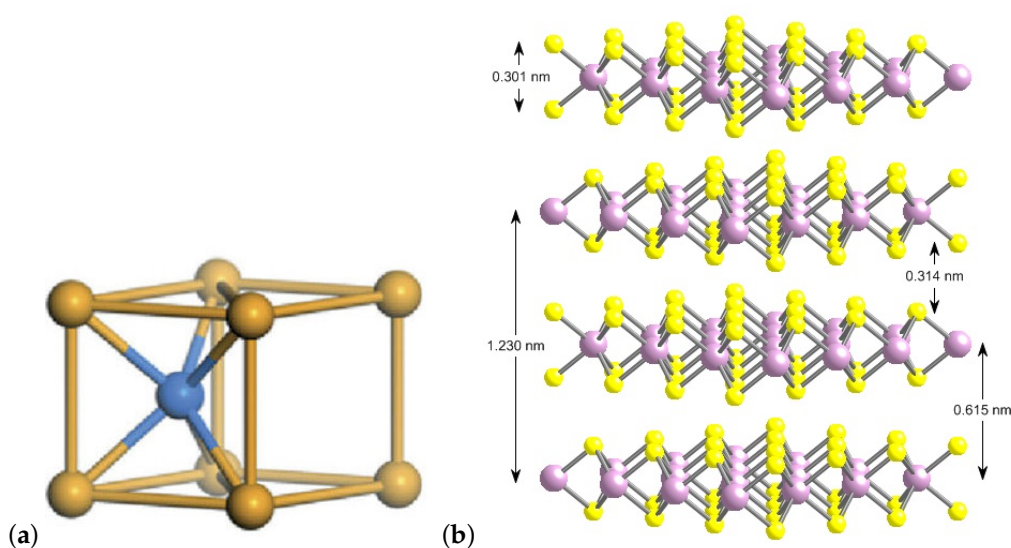


Figure 1. (a) Crystallographic structure of 2H-MoS₂ bulks and (b) Three-dimensional structure of 2H-MoS₂ mono-layers.

Figure 2 shows the calculated band gap of MoS₂ bulks and that of MoS₂ few-layers. The bulk 2H-MoS₂ crystal is an indirect band-gap semiconductor with a band gap of 1.23–1.29 eV [32,34–36]. MoS₂ bulks can be employed as cathode materials in batteries [29]. MoS₂ bulks show very poor catalytic activities for hydrogen evolution reactions. The band gap of MoS₂ is a function of layer thickness as shown in Figure 2b–d, and unperturbed by substrate interactions. The mono-layer MoS₂ has a direct band gap of 1.8 eV [37]. The band structure changes from the indirect-gap in bulks to the direct-gap in MoS₂ mono-layers, being confirmed from experiments [38,39]. The thickness-dependent electronic structure change is closely associated with many corresponding changes in chemical and physical properties. For example, the transition for indirect-to-direct band gap is correlated with changes in mechanical strength, spin density, bond energy, electrical conductivity, and the properties of transistor and sensor devices. MoS₂ nanoparticles can adsorb various compounds, including tetrahydrothiophene, thiophene, benzothiophene, dibenzothiophene, and their derivatives [40]. The chemical [29,41] and physical properties [42–44] of MoS₂ few-layers were recently reviewed. These novel properties of MoS₂ 2D materials make them suitable 2D candidates in environmental applications [45,46], catalysts (such as electrocatalysts [47–51] and photocatalysts [48–53]), energy storage (such as lithium ion batteries [48,49,54], supercapacitors [49,54], elastic energy [12], and solar cells [49]), as well as sensing [55]. MoS₂ mono-layers were also fabricated into ultrasensitive photodetectors [56,57], and integrated circuits to perform the NOR logic operation [58], besides being employed in drug delivery [59], thermoelectrics [60,61], piezotronics [62,63], osmotic nanopower generators [64], and valleytronics [65].

Because of the novel properties and wide applications of 2H-MoS₂ 2D layers, MoS₂ 2D layers have been prepared by various physical or chemical methods [41,44–46,66–69]. Individual MoS₂ layers were usually obtained by the micromechanical cleavage technique [70] because of weak interactions between sulfur layers and strong intralayer interactions of MoS₂ bulks. The mechanically cleaved MoS₂ layers are usually highly crystalline with low defect density. Massive MoS₂ layers have successfully been produced through the liquid-phase exfoliation [71,72]. MoS₂ few-layers can also be fabricated from CVD. Interested readers can refer to the references herein.

The MoS₂-based devices will be used in harsh environments from basic science to industry, such as near nuclear plants/reactors and nuclear medicine imaging. Radiations may damage MoS₂ layers by breaking atomic bonds and ionizing atoms. To use the MoS₂ devices reliably under irradiation, it is desirable to explore the irradiation effects on MoS₂ layers.

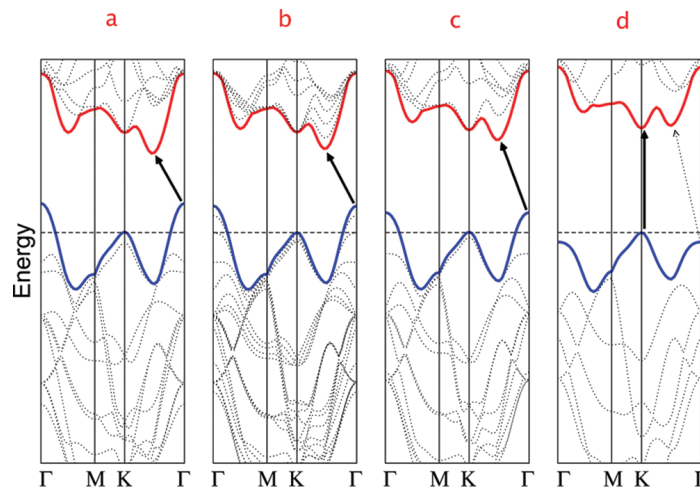


Figure 2. Calculated band structures of (a) bulk MoS₂, (b) quadri-layer MoS₂, (c) bi-layer MoS₂, and (d) mono-layer MoS₂ [39]. The solid arrows indicate the lowest energy transitions. Bulk MoS₂ is characterized by an indirect band gap. The direct excitonic transitions occur at high energies at K point. With reduced layer thickness, the indirect band gap becomes larger, while the direct excitonic transition barely changes. For mono-layer MoS₂ in (d), it becomes a direct band-gap semiconductor. The horizontal solid lines in each panel indicate the valence band maximum (VBM) and the dotted lines indicate the conduction band minimum (CBM). The solid blue arrows indicate the lowest energy transitions. Reprinted with permission from Reference [39]. Copyright © 2010 American Chemical Society.

1.2. Irradiation Sources

Figure 3 shows the spectrum of electromagnetic irradiation. Cosmic rays are composed of particularly high-energy particles and photons. Primary cosmic rays are composed primarily of 99% nuclei (about 90% protons, 9% alpha particles, and 1% nuclei of heavier elements) and about 1% solitary electrons. The energy of the cosmic rays is high up to 10²⁰ eV for the primary cosmic rays. When entering the Earth atmosphere, the primary cosmic rays collide with atoms and molecules to produce secondary cosmic particles with lower energy and electromagnetic waves, including gamma-ray, X-ray, neutrons, protons, electrons, and alpha particles. The energy of the generated gamma rays can be 50 MeV. These primary and secondary cosmic rays should damage microelectronic devices because of sufficient energy, causing soft errors in electronic integrated circuits, especially in small-scale devices. Here, several ion irradiation and electromagnetic irradiation from GeV to meV are reviewed on 2D MoS₂ few-layers. Physical properties of MoS₂ bulks and thick films are also covered for comparison with those of 2D MoS₂ few-layers.

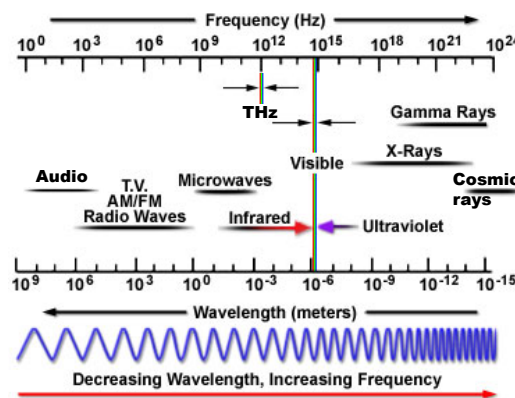


Figure 3. Spectrum of electromagnetic irradiation.

1.3. Irradiated MoS₂ Materials

Defects are created in MoS₂ few-layers when the layers are fabricated by exfoliation technique and vapor deposition growth when layers are transferred from substrate to substrate, and placed under electromagnetic radiation and energetic particle fluxes. The defects typically deteriorate the device quality of MoS₂ layers. On the other hand, defects in MoS₂ also have a beneficial impact on material properties. For instance, defects have been shown to be the dominant dopant in MoS₂, with natural defect variation allowing *n*-type and *p*-type regions to coexist across distinct regions of the same sample [73]. The sulfur vacancies can lower Schottky barrier heights of MoS₂ [73]. Therefore, it is crucial to fully understand defects in MoS₂ to develop a reliable MoS₂-based electronics. In this paper, irradiation-related defects of MoS₂ few-layers are focused on.

Up to now, MoS₂ 2D layers have been irradiated under different irradiation sources. Table 1 lists some typical irradiation effects of MoS₂ materials. The details are summarized in the following sections. The particle irradiation and electromagnetic irradiation will be reviewed first on structural properties and defects, then theoretical explanations of the irradiation mechanism are discussed. The irradiation-induced band structures, electric, catalytic, and magnetic properties will be summarized at the end. To understand the irradiation-induced defects well, the synthesis/preparation details of the as-prepared MoS₂ layers will be described in each section in addition to irradiation.

Table 1. Radiation Induced Defects in 2H MoS₂.

MoS ₂	Irradiation	Particle Energy	Dose/Fluence	Irradiation Source	Irradiation Conditions	Results	Ref.
200 μm thickness	electron	0.7 MeV	150–600 kGy	electron accelerator	RT	created S vacancies	[74]
200 μm thickness	electron	2.0 MeV	100–250 kGy	electron accelerator	RT	created S vacancies and Mo vacancies, diamagnetic to ferromagnetic phase transition	[74]
20 layer	electron	5 keV	50 nA for 15 min	SEM beam	in vacuum	formed crystalline islands	[75]
mono-layer	electron	60 keV	10 ⁶ –10 ⁹ electron /nm ²	STEM beam	400–700 °C in vacuum	induced 2H/1T phase transition	[76]
~10 layer	electron	3–15 keV	n/a	EPMA	in vacuum	broke the inversion symmetry	[77]
mono-layer	electron	80 keV	n/a	TEM beam	in vacuum	removed top and bottom S atoms	[78]
mono-layer	electron	200 keV	3000 electrons/nm ² /s	TEM beam	in vacuum	created S vacancies, increased electric resistance	[79]
mono-layer	electron	15 keV	280 μC/cm ²	EBL	in vacuum	produced local strain and changed band structure	[80]
mono-layer	electron	80 keV	40 A/cm ²	TEM beam	in vacuum	produced holes and Mo ₅ S ₃ nanoribbons	[81]
amorphous 5–7 layer	electron	1 keV	1–10 min	EBI	in vacuum	crystallized	[82]
mono-layer	U ²³⁸	1.14 GeV	4000 ions/cm ²	heavy ion accelerator	in vacuum	total damaged	[83]
micron thickness	Ar ⁺	500 eV	2.26 × 10 ¹⁵ ions/cm ²	plasma	UHV	produced S vacancies	[84]
bi-layer	Ar ⁺	500 eV	10 ¹⁴ –10 ¹⁵ ions/cm ²	plasma	UHV	produced S vacancies and MoS ₆ vacancy clusters	[84]
mono-layer	Ar ⁺	500 eV	2.26 × 10 ¹⁵ ions/cm ²	plasma	UHV	damaged	[84]
200 μm thickness	proton	3.5 MeV	5 × 10 ¹⁸ ions/cm ²	Singletron facility	RT	preserved lattice structure, produced defects, changed magnetic moments	[85]
few-layer	proton	10 MeV	10 ¹² –10 ¹⁴ ions/cm ²	MC-50 cyclotron	n/a	decreased electrical conductance	[86]
mono-layer	proton	100 keV	10 ¹² –10 ¹⁵ particles/cm ²	LEAF	n/a	created defects	[87]
bi-layer	proton	100 keV	6 × 10 ¹⁴ particles/cm ²	LEAF	n/a	created defects	[87]
bulk	He ²⁺	1.66 MeV	900 MGy	ion accelerator	n/a	changed Raman scattering slightly	[88]
nanosheet	He ²⁺	1.66 MeV	900 MGy	ion accelerator	n/a	invariant	[88]
few-layer	He ²⁺	30 keV	10 ¹⁸ ions/cm ²	FIB beam	in vacuum	milled or damaged	[89]
mono-layer	He ²⁺	3.04 MeV	8 × 10 ¹³ particles/cm ²	PTA	n/a	produced defects	[90]
mono-layer	He ⁺	30 keV	10 ¹² –10 ¹⁶ ions/cm ²	HIM	in vacuum	produced S vacancies	[91]
mono-layer	He ⁺	30 keV	10 ¹³ –10 ¹⁷ ions/cm ²	NFM	in vacuum	generated disorder	[92]
bulk	Ar ⁺	500 eV	3 × 10 ^{−3} ions/cm ²	STM	UHV	removed S atoms	[93]
micron thickness	Ar ⁺	500 eV	10 ¹⁴ –10 ¹⁵ ions/cm ²	n/a	UHV	produced S vacancies at low doses and Mo/MoS ₆ vacancies at high doses	[84]
powder	Ar ⁺	3 keV	0.1 A/cm ²	n/a	n/a	removed S atoms	[94]

Table 1. Cont.

MoS ₂	Irradiation	Particle Energy	Dose/Fluence	Irradiation Source	Irradiation Conditions	Results	Ref.
200 nm	Ar ⁺	180 keV	10 ¹⁵ –10 ¹⁷ ions/cm ²	IBAD	200 °C in vacuum	induced amorphization	[95]
bi-layer	Ar ⁺	500 eV	10 ¹⁴ –10 ¹⁵ ions/cm ²	n/a	UHV	produced S vacancies at low doses and Mo/MoS ₆ vacancies at high doses	[84]
mono-layer	Ar ⁺	500 eV	10 ¹⁴ –10 ¹⁵ ions/cm ²	n/a	UHV	produced S vacancies at low doses and Mo/MoS ₆ vacancies at high doses	[84]
mono-layer	Ar ⁺	500 eV	3–11 μA/cm ²	sputter beam	vacuum	selectively removed S atoms without significantly depleted Mo atoms	[96]
mono-layer	Ar ⁺	13.56 MHz	n/a	RF plasma	RT	produced 2H/1T phase transition	[97]
mono-layer	Ga ion	n/a	n/a	PAMBE	450 °C in vacuum	doped Ga, reduced binding energy	[98]
mono-layer	Ga ion	30 keV	10 ¹³ ion/cm ²	FIB beam	in vacuum	produced sub-nm pores and vacancies	[99]
bulk	Xe	91 MeV	10 ions/μm ²	GANIL	n/a	formed nano-hillocks	[100]
few-layer	Xe	91 MeV	15 ions/μm ²	GANIL	n/a	formed nano-incisions	[100]
mono-layer	Xe ion	91 MeV	15 ions/μm ²	GANIL	n/a	formed nano-incisions	[100]
mono-layer	Xe ion	25–30 keV	10 ¹⁰ ion/cm ²	EBIT	n/a	induced pits and hillocks	[101]
1–4 layer	Bi ion	0.45–1.23 GeV	10 ¹⁰ –10 ¹² ions/cm ²	HIRFL	vacuum, RT	formed hillocks	[102]
mono-layer	Mn ion	25 keV	10 ¹² –10 ¹⁴ ions/cm ²	TOF-SIMS	UHV	formed defects	[103]
bulk	C ₆₀	20–40 MeV	10 ⁹ –10 ¹¹ ions/cm ²	TA	RT	modified structures	[104]
micron thickness	γ-ray	n/a	5 × 10 ⁹ R	RGIF	in air	no damaging effects	[105]
50–132 layer	γ-ray	662 keV	5000 photons	¹³⁷ Cs source	RT in air	unaffected	[106]
5–8 layer	γ-ray	~1.2 MeV	120 Mrad	⁶⁰ Co source	RT in air	converted to MoO _x	[107]
1–3 layer	X-ray	10 keV	6 Mrad	XRD	RT in air	no noticeable degradation	[108]
film	UV	n/a	n/a	mercury lamp	in O ₂ (ozone)	formed oxygen-sulfur bonds	[109]
mono-layer and multilayer	UV	n/a	10 ¹⁰ –10 ¹³ photos/cm ²	deuterium lamp	vacuum	no structural damage, no oxidation	[110]
multilayer	laser	λ = 514 nm	1–20 mW for 1–100 s	laser	RT in air	stable or damage depending on laser power	[111]
few-layer	laser	λ = 532 nm	300 mW	diode laser	in air or vacuum	patterned and thinned	[112]
mono-layer	laser	λ = 800 nm	20–50 mJ/cm ²	Ti:sapphire laser	RT	damaged or unaffected depending on irradiation intensity	[113]

EBI: electron-beam irradiation; EBIT: electron-beam ion trap; EBL: electron-beam lithography system; EPMA: electron probe micro-analyzer; FIB: focused ion beam; GANIL: The Grand Accélérateur National d'Ions Lourds (Large Heavy Ion National Accelerator); HIM: helium-ion microscope; HIRFL: heavy ion Research facility in Lanzhou; IBAD: ion-beam assisted deposition; LEAF: low-energy accelerator facility; NFM: NanoFab microscope; PAMBE: plasma-assisted molecular beam epitaxy; PTA: Pelletron tandem accelerator; RF: radio frequency; RGIF: Reactor Gamma Irradiation Facility; RT: room temperature; S: sulfur; SEM: scanning electron microscope; STEM: scanning transmission electron microscope; STM: scanning tunneling microscope; TA: Tandem accelerator; TEM: transmission electron microscope; TOF-SIMS: time-of-flight secondary ion mass spectrometer; UHV: ultra-high vacuum; XRD: X-ray diffractometer.

2. Charged Particle Irradiation

2.1. Swift-Heavy Ion Irradiation

Swift-heavy ions are usually accelerated in particle accelerators to very high energies, typically in the MeV or GeV range. They have sufficient kinetic energy and mass to penetrate solid materials along straight lines. Therefore, heavy ions release sufficient energy to displace atoms, induce heating, permanently modify crystal structure, and leave tracks of heavily damaged structure.

2.1.1. Uranium-238 Ion Irradiation

Exfoliated MoS₂ mono-layers were irradiated by 1.14 GeV uranium (²³⁸U) ions [83]. It was found that its electrical properties were significantly changed and the MoS₂-based transistor was destroyed at a fluence of 4×10^{11} ions/cm² (4000 ions/μm²).

2.1.2. Gallium Ion Irradiation

Michra et al. [98] deposited *p*-type mono-layered MoS₂ on *c*-sapphire substrates using CVD technique and irradiated the layers at 450 °C for 30 s at a low Ga flux beam (equivalent pressure: 6×10^8 torr) in ultra-high vacuum (UHV) conditions. Ga ions were produced from a plasma-assisted MBE system. Figure 4 shows the Raman spectra and X-ray photoelectron spectroscopy (XPS) spectra of Ga-irradiated MoS₂ mono-layers. Raman peaks, especially A_{1g} mode, shifted after the Ga-irradiation. Mo-3d^{5/2} peaks shifted towards lower energies for Ga-irradiated samples relative to that of the pristine MoS₂ mono-layer. New Ga-2p^{1/2} and Ga-2p^{3/2} core levels were observed at 1117 eV and 1144 eV, respectively, revealing the incorporation of Ga into the MoS₂ layers. The Ga-irradiation reduced the value of binding energy of 0.2 eV. Room temperature photoluminescence (PL) spectroscopy indicated that the optical properties of the MoS₂ layers were changed.

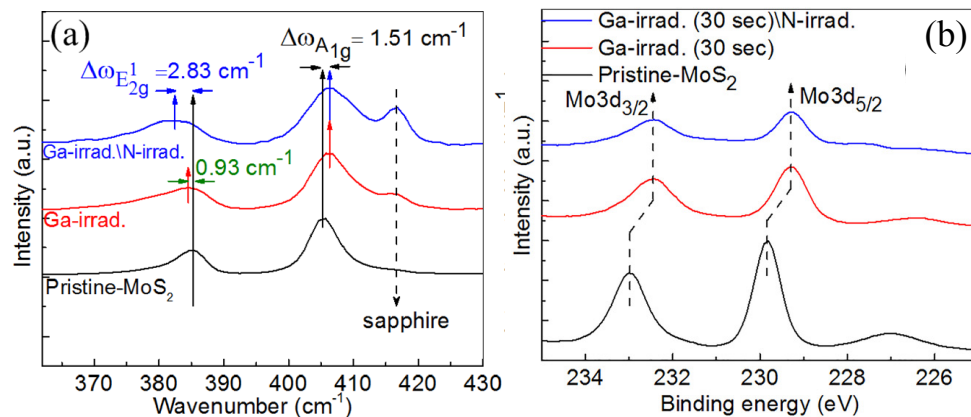


Figure 4. (a) Raman spectra and (b) Mo-3d XPS of pristine- and Ga-irradiated mono-layered MoS₂ samples [98]. Reprinted with permission from Reference [98], with the permission of AIP Publishing.

Thiruraman et al. [99] synthesized single-layer MoS₂ triangular-flakes via a halide-assisted powder vaporization method and transferred over holes. The suspending MoS₂ mono-layers were irradiated by Ga⁺ ions in a focused ion beam (FIB). The Ga⁺ ion dose varied from 6.25×10^{12} ions/cm² to 2.50×10^{13} ions/cm². Figure 5 shows high angle annular dark-field (HAADF) images of the MoS₂ mono-layers before and after Ga⁺ ion irradiation for different doses: 0 (pristine), 6.25×10^{12} ions/cm², 8.16×10^{12} ions/cm², 1.11×10^{13} ions/cm², 1.60×10^{13} ions/cm², and 2.50×10^{13} ions/cm². Statistical analysis showed that Ga⁺ ion irradiation produced pores with average and maximum diameters of 0.5 nm and 1.0 nm. Within the irradiation dose range, the nanopore density increased with increasing doses. With increasing ion doses, nanopores started to merge, resulting in larger and irregularly shaped pores. For the lowest dose (6.25×10^{12} ions/cm²),

most of the atomic pores were single-molybdenum-based vacancies, while the amount of missing sulfur varied. With an increasing Ga^+ ion dose, the number of double-molybdenum-based vacancies increased, and some triple-molybdenum-based vacancies were also found. When the Ga^+ ion dose reached to 2.50×10^{13} ions/ cm^2 , the density of larger pores (with diameter size > 0.8 nm) increased. Metal atomic vacancies were formed with sulfur vacancies while few topological defects and amorphous regions were observed.

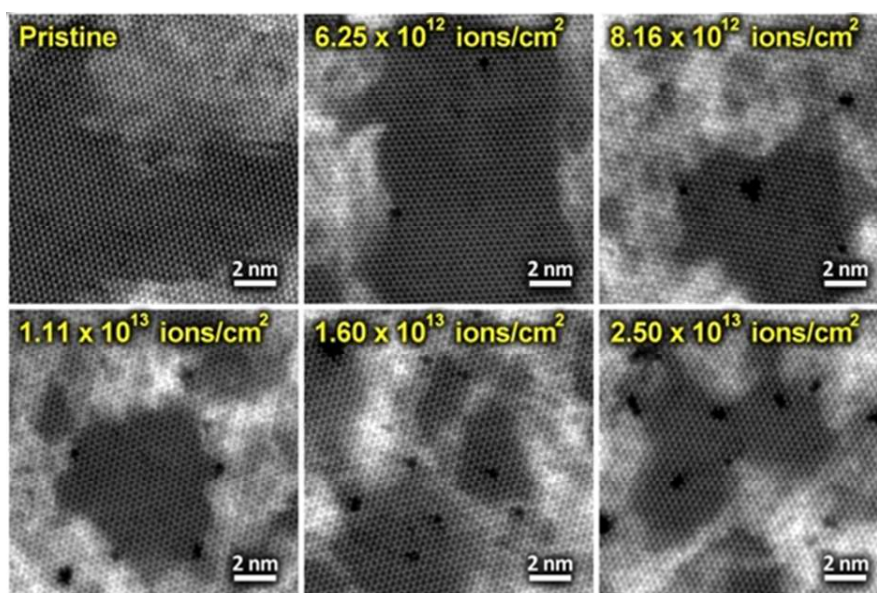


Figure 5. HAADF images of the pristine and the 30 keV Ga^+ ion-irradiated MoS_2 mono-layers with different ion doses [99]. Reprinted with permission from Reference [99]. Copyright © 2018 American Chemical Society.

2.1.3. Xenon Ion Irradiation

Madauβ et al. [100] fabricated ultra-thin mechanically exfoliated MoS_2 sheets on SiO_2 substrates and irradiated them using 91 MeV Xe ions. Figure 6a shows Atomic force microscopy (AFM) images of the track morphology in MoS_2 with various thicknesses. In the case of bulk-like MoS_2 , chains of nanosized hillocks were generated and protruded from the surface. For few-layer MoS_2 sheets (thickness under 10 nm), individual hillocks were created and mixed with incisions. In even thinner MoS_2 sheets, i.e., tri-layered, bi-layered, and mono-layered MoS_2 sheets, the major part of the surface track consisted of a continuous incision. The length of the incision varied among tri-layered (3L), bi-layered (2L), and single-layered (1L) sheets. Compared with the surface track length of mono-layers, the length of the incisions was reduced by $\sim 25\%$ for a bi-layer and by $\sim 50\%$ for a tri-layer. Additionally, the surface tracks in tri-layered and bi-layered MoS_2 were accompanied by protrusions before and after the central incision. Mono-layered MoS_2 surface tracks generally consisted only of incisions and no protrusions. Figure 6b shows lattice information around an incision (length 100 nm) created by a projectile. The extended incisions were oriented along the direction of the incoming ion beam and extremely narrow (less than 10 nm). The edges of the incision were relatively straight at an atomic scale. The surrounding lattice remained undisturbed while the violent atomic displacements took place inside the ion track core. Several mechanisms were proposed to explain the ion irradiation damages, such as electrostatic repulsion between the atoms in the ionized region, exciton self-trapping causing a local lattice distortion, non-thermal melting caused by significant changes of the interatomic potentials, and phase transitions such as melting due to a thermal spike. It was assumed that the hillock chains in bulk-like MoS_2 sheets consisted of nonstoichiometric MoS_2 which re-solidified after a phase transition caused by the thermal spike. The nanoscaled incisions should have originated from

the material evaporation. It was reported that the threshold for grazing incidence of Xe ions was 2.0 keV/nm.

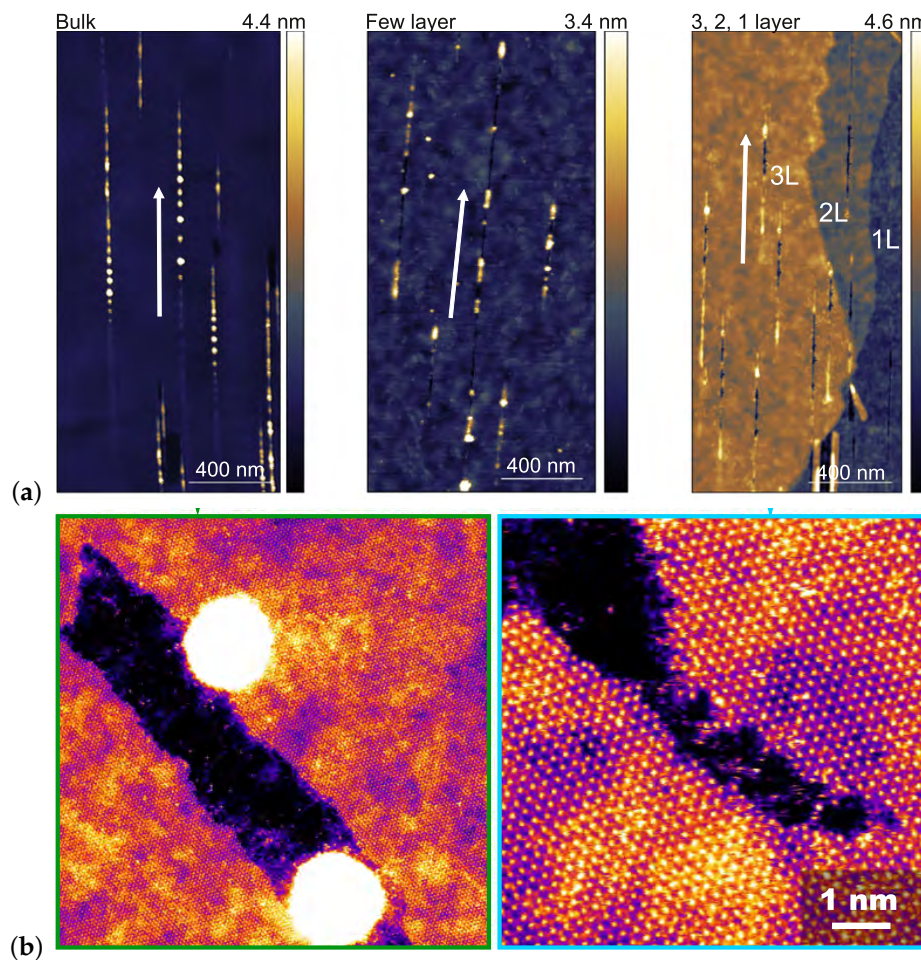


Figure 6. (a) AFM images of Xe irradiated MoS₂ with varying thicknesses from bulk-like down to single layer (grazing angle $\theta \leq 1^\circ$) deposited on SiO₂ substrates and (b) STEM images of irradiated freestanding MoS₂ mono-layers [100] (grazing angle $\theta \leq 0.2^\circ$), showing middle (left panel) and end (right panel) of an incision created by one ion. Energy of Xe ions: 91 MeV. Fluence: 10–15 ions/ μm^2 . The directions of the ion beam in (a) are marked by white arrows. The black stretches in (b) are parts of an incision cut into the MoS₂ mono-layer by the projectile. The round white spots in (b) are molybdenum clusters. Reprinted with permission from Reference [100]. 1L: mono-layer; 2L: bi-layer; 3L: tri-layer. Copyright © under the terms of the Creative Commons Attribution 3.0 license.

Hopster et al. [101] deposited MoS₂ mono-layers on KBr(100) substrates and irradiated them with highly charged Xe ions (Xe³⁵⁺ with kinetic energy of 25.4 keV and Xe⁴⁰⁺ with kinetic energy of 38.5 keV) in a vacuum at room temperature. The fluences ranged from 5×10^9 – 2×10^{10} ions/cm². Hillocks were observed on the MoS₂ mono-layer surfaces. The MoS₂ mono-layers were exfoliated from a single crystal under ambient condition while no details were provided, so it is hard to compare their results with other groups.

2.1.4. Bismuth Ion Irradiation

Guo et al. [102] deposited 1–4-layer-ed MoS₂ on silicon substrates capped with SiO₂. The mechanically exfoliated MoS₂ nanosheets were irradiated by ²⁰⁹Bi ions with energies of 0.45–1.23 GeV and fluences of 1×10^{10} – 3.6×10^{12} ions/cm² in a vacuum at room temperature under normal incidence. The hillock-like latent tracks were observed on the surface of irradiated MoS₂ few-layers and attributed

to the ionization and excitation of energy transfer from ^{209}Bi ions to the electron system. The induced damages shifted the Raman A_{1g} peak to a higher frequency and increased the intensity ratio between the A_{1g} and E_{2g}^1 modes.

2.1.5. Manganese Ion Irradiation

Mignuzzi et al. [103] mechanically exfoliated natural bulk MoS_2 and deposited it on Si substrates covered with SiO_2 . The exfoliated MoS_2 mono-layers were bombarded with Mn^+ (kinetic energy of 25 keV) with different ion doses (10^{12} – 10^{14} ions/ cm^2) in a UHV. The resulting average inter-defect distance ranged from 1 nm to 10 nm. The generated defects activated new Raman modes around 227 cm^{-1} , broadened Raman peaks, and shifted Raman modes.

2.1.6. Gold Ion Irradiation

Zhai et al. [114] bombarded MoS_2 (0001) bulk surfaces using Au ions with 13.4 MeV. Under ion doses of 1.0×10^{13} ions/ cm^2 , 1.0–3.5 nm craters were generated on the surface.

2.1.7. Silver Ion Irradiation

Bhattacharya et al. [115] irradiated magnetron-sputtered amorphous MoS_2 films of thicknesses 50–750 nm with a $5 \times 10^{15}\text{ cm}^{-2}$ dose of 2 MeV Ag ions. The sliding life of Ag ion-irradiated films increased ten-fold to thousand-fold compared to as-sputtered films. The improvement in wear life was correlated with a significant improvement in adhesion of the films with the substrates and a small increase in the density of the ion-irradiated films.

2.1.8. C_{60} Ion Irradiation

Henry et al. [104] irradiated MoS_2 bulks under 20–40 MeV C_{60} ions at 300 K. Irradiation was performed at normal incidence and at high fluences (3×10^{11} ions/ cm^2), as well at a grazing incidence of 20° and a low fluence of 10^9 ions/ cm^2 . The structural modifications occurred in the vicinity of the projectile paths.

2.2. Argon Ion Irradiation

Argon ion beams (500 eV) were employed as early as 1987 [9] to irradiate MoS_2 crystalline films (cleaved from a single crystal) with a thickness of 0.7 μm . The Ar bombardments created sulfur vacancies and reduced molybdenum of MoS_2 edge surfaces.

Inoue et al. [93] studied defects generated by Ar^+ ion irradiation of MoS_2 bulk surface by scanning tunneling microscopy (STM). A clean MoS_2 surface was prepared by cleaving the surface layers of a MoS_2 bulk crystal with Scotch tape. The cleaved clean MoS_2 was then degassed in a UHV chamber by electrical heating at 538 K for half an hour to provide a clean and contamination-free surface. The sample was irradiated with Ar^+ ions at an energy of 500 eV and an irradiation density of 75×10^{11} ions/ cm^2 . The incident angle of Ar^+ ion was ± 2 – 3° from the normal to the MoS_2 surface. The irradiated MoS_2 sample was heated at 583 K for an hour by direct current heating through the substrate to remove residual ions on the sample surface after irradiation. Low-density individual defects were observed. Some surface defects were formed by removal of sulfur atoms from the top MoS_2 surface. Some defects may originate from the hybridized dangling bond composed of the Mo-4d orbital and removal of MoS_2 layer fragments.

Bae et al. [84] MoS_2 prepared slabs with a thickness of several microns from MoS_2 crystals using the mechanical exfoliation method and then irradiated them with Ar^+ ions with an energy of 500 eV in an UHV, with fluences of 5.65×10^{14} ions/ cm^2 and 2.26×10^{15} ions/ cm^2 . The incident angle of Ar^+ was almost normal to the surface of the samples. Residual argon on sample surfaces was removed by heating at 583 K for one hour in an UHV after the irradiation process. Figure 7 shows the Raman spectra of Ar^+

irradiated samples. After Ar^+ irradiation, additional broad satellite peaks appeared in the lower-frequency side of both the E_{2g}^1 and A_{1g} peaks, located at $377\text{--}381\text{ cm}^{-1}$ and $404\text{--}406\text{ cm}^{-1}$ respectively.

The Raman satellite peaks shifted to lower wave-numbers while their intensity increased with increasing Ar^+ doses. First-principles calculation showed that new satellite modes were related to molybdenum vacancies, sulfur vacancies, or MoS_6 vacancy clusters. The lower shift of the satellites of the E_{2g}^1 mode should have come from the large cluster vacancy. The A_{1g} and E_{2g}^1 mode of MoS_2 materials remained unchanged before and after the irradiation. It is believed that the new peaks were induced by lattice defects introduced by Ar^+ irradiation. Additionally, the intensity of the satellite peaks increased with the increasing irradiation dose and dominated over the E_{2g}^1 and A_{1g} modes of pristine MoS_2 , indicating the formation of molybdenum vacancies or MoS_6 vacancies.

Baker et al. [94] irradiated MoS_2 powders under a 3 keV Ar^+ ion beam with a current density of $0.1\text{ }\mu\text{A}/\text{cm}^2$. The Ar^+ ion-beam bombardment caused the preferential sputtering of sulfur and produced an amorphous MoS_x phase of depth of 3.8 nm. The Mo/S ratio increased with increasing bombardment time, as shown in Figure 8.

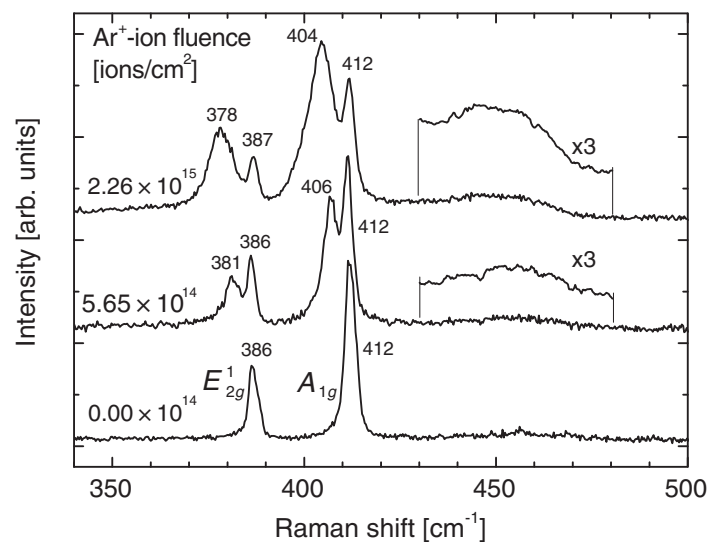


Figure 7. Raman spectra of (bottom) MoS_2 crystalline bulk, Ar^+ -irradiated MoS_2 micron crystals at fluences of (middle) 5.65×10^{14} ions/ cm^2 and (top) 2.26×10^{15} ions/ cm^2 [84]. Reprinted with permission from Reference [84]. Copyright © 2017 by the American Physical Society.

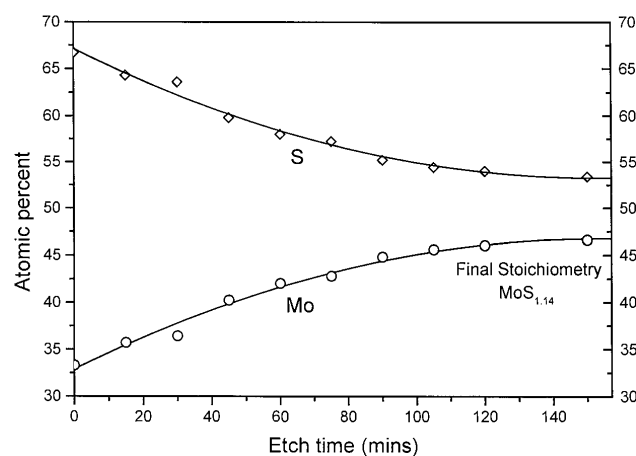


Figure 8. Surface composition of MoS_2 powders when exposed to a 3 keV Ar^+ ion beam [94]. The atomic percent was calculated from energy-dispersive X-ray spectroscopy. Reprinted from Reference [94]. Copyright ©1999, with permission from Elsevier.

Wahl et al. [95] deposited MoS₂ layers (roughly 200 nm) on steel and Si substrates via ion-beam assisted deposition. The produced MoS₂ layers were fully dense with basal-oriented microstructures. The deposited MoS₂ layers were then irradiated with 180 keV Ar²⁺ ions at doses of 1×10^{15} ions/cm², 1×10^{16} ions/cm², and 5×10^{16} ions/cm² at room temperature in a vacuum. Figure 9a shows X-ray diffraction (XRD) patterns of the as-deposited and ion-irradiated coatings. The intensity of the (002) main peak at 13.5° decreased with increasing irradiation doses. The basal plane peak ($2\theta = 11^\circ$) disappeared after the irradiation. Figure 9b shows Raman spectra of the samples. The main peaks of the Raman spectra were kept after the irradiation, while their intensity decreased with increasing doses. To explore the irradiation effects, the microstructure of the MoS₂ layers was characterized by high-resolution transmission electron microscopy (HRTEM) as shown in Figure 9c. The as-deposited MoS₂ consisted of basal-oriented and nanocrystalline MoS₂ with horizontal (002) fringes. After an irradiation dose of 1×10^{15} ions/cm², some regions became amorphous, and the surviving crystalline regions (still with the basal orientation) were embedded in the amorphous matrix. After a high irradiation dose of 5×10^{16} ions/cm², the MoS₂ regions were nearly amorphous, although few crystalline regions existed. The surviving crystalline regions oriented randomly after the high dose irradiation. The irradiation-reduced microstructural change degraded tribological behaviors of MoS₂ coatings, such as accelerated wear and eliminated lubrication.

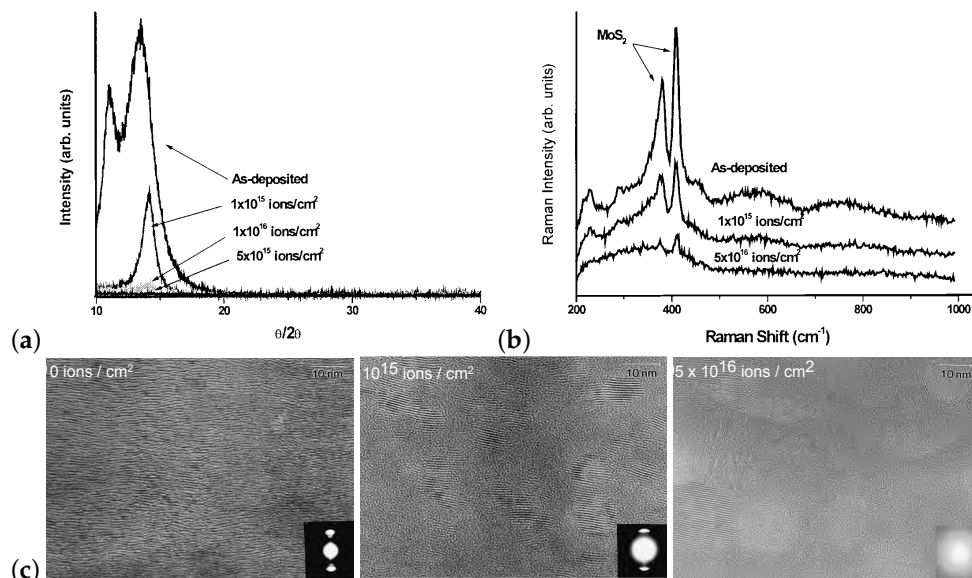


Figure 9. (a) XRD patterns, (b) Raman spectra, and (c) cross-sectional HRTEM images of MoS₂ coatings on Si substrates as-deposited and irradiated with 180 keV Ar²⁺-ions [95]. Insets: selected-area electron diffraction (SAED) patterns. Reprinted from Reference [95]. Copyright © 2000, with permission from Elsevier.

Murray et al. [116] irradiated mechanically exfoliated MoS₂ few-layers (5–15 layers) under low-energy Ar (200 eV and 1×10^{13} – 10^{15} ions /cm²). The electric resistance increased 100 times after a high dose of irradiation because of induced defects.

Bae et al. [84] also prepared MoS₂ bi-layers by chemical exfoliation from MoS₂ micron powders in a hexane solution of butyllithium. The prepared bi-layers were then irradiated by Ar⁺ ions with an energy of 500 eV in an UHV, with fluences of 5.65×10^{14} ions/cm² and 2.26×10^{15} ions/cm². Figure 10 shows Raman spectra of the MoS₂ bi-layers before and after Ar⁺ irradiation. The A_{1g} and E_{2g}^1 modes were broadened. It was claimed that a new broad peak emerged at approximately 373 cm^{-1} , which was 10 cm^{-1} away from the E_{2g}^1 peak. There was a broad feature at around 435 cm^{-1} . The mode was relatively enhanced after the irradiation. The new vibration mode was identified as a unique signature of the sulfur vacancies.

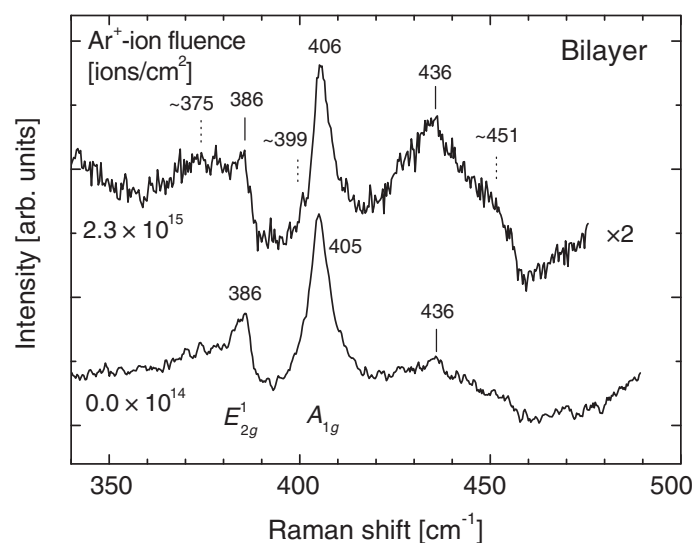


Figure 10. Raman spectra of MoS₂ bi-layers before (bottom) and after (top) Ar⁺ irradiation at the fluence of 2.26×10^{15} ions/cm² [84]. Reprinted with permission from Reference [84]. Copyright © 2017 by the American Physical Society.

Bae et al. [84] claimed that MoS₂ mono-layers were destroyed by Ar⁺ irradiation with 500 eV. Chen et al. [117] sputtered MoS₂ mono-layers with Ar⁺ ions (500 eV and emission current of 20 mA), defect peaks of Raman scattering were observed and its hydrogen evolution performance was enhanced. However, no details were reported in the literature.

Zhu et al. [97] treated CVD-grown MoS₂ mono-layers under radio-frequency (RF) argon plasma with 13.56 MHz at room temperature for 40 s. The very weak Ar plasma had enough kinetic energy to trench the S-Mo bond while no enough energy to etch molybdenum and sulfur atoms. Thus, the plasma treatments induced the lateral sliding of the top S layer and the 2H phase transitioned to the 1T phase.

Ma et al. [96] grew MoS₂ mono-layers on SiO₂ substrates and treated them in a vacuum under 500 eV Ar⁺ ions at room temperature. The beam current density was 3.1–11.2 μA/cm². The molybdenum content of the MoS₂ layers remained essentially constant while the amount of sulfur decreased significantly during irradiation. The sulfur content of the layers could be reduced to 50%. The average sputter yield was 0.03 sulfur atom per Ar⁺ ion. During the irradiation procedure, MoS₂ mono-layers were selectively de-sulfurized while the basic physical structure of the MoS₂ remained largely intact. The photoluminescence (PL) yield decreased as sulfur atoms were removed by the Ar⁺ irradiation.

Ar⁺ plasma was also employed to thin MoS₂ sheets at room temperature [118]. It was reported that the top MoS₂ layers were entirely removed by the Ar⁺ plasma while the bottom MoS₂ layers remained largely unaffected. Thus, MoS₂ multi-layers with controllable thickness, even MoS₂ single-layers, could be prepared reliably (with almost 100% success rate).

Chen et al. [117] prepared MoS₂ mono-layers using a liquid exfoliation method, and annealed them at 300–450 °C in a vacuum. The treated layers were then deposited on Au substrates and exposed to 0.5 keV Ar⁺ ions for 1 min. Defects were introduced into the MoS₂ layers, influencing the electronic structures of MoS₂. Figure 11 shows XPS spectra of irradiated MoS₂ mono-layers. Peaks shifted because of induced defects.

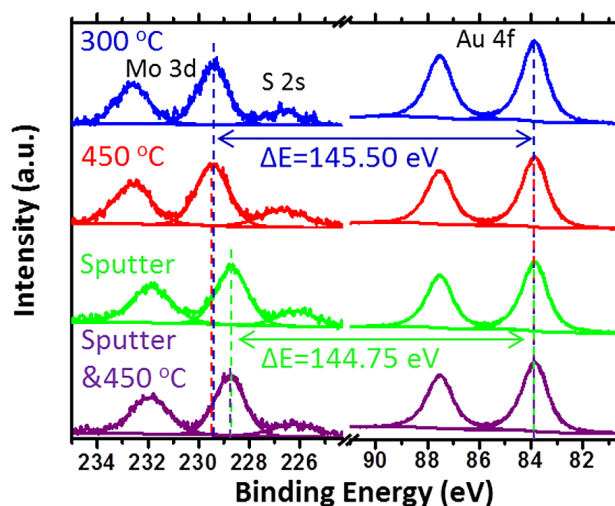


Figure 11. X-ray photoelectron spectra of the Mo-3d and S-2s in the MoS₂ mono-layers on Au substrates before and after Ar⁺ sputtering. XPS of Au-4f electrons were shown as a standard reference. Reprinted with permission from Reference [117]. Copyright © 2018 American Chemical Society.

2.3. Neon Ion Irradiation

Maguire et al. [92] also irradiated CVD-grown MoS₂ mono-layers with Ne⁺ ions with an energy of 30 keV. With increasing Ne⁺ ion doses, the A_{1g} and E_{2g} modes were quenched and broadened, indicating the growing disorder induced by the Ne⁺ ions.

2.4. Alpha-Particle/Helium-Ion Irradiation

Alpha particles consist of two protons and two neutrons which are tightly bound together, which is identical to a helium ion (He²⁺). They are produced either from particle accelerators in the form of helium-ion beams or from the process of alpha decay of alpha-particle-emitting radionuclides. Alpha particles have been widely studied in radiopharmaceutical therapy that is a promising treatment approach under active pre-clinical and clinical investigation [119,120]. Decayed alpha particles generally have a kinetic energy of about 5 MeV, which induce defects and even 'cut' the MoS₂ nanosheets.

Isherwood et al. [88] studied the effects of alpha-particle (helium nuclei) irradiation (1.66 MeV) on both bulk and liquid-phase exfoliated MoS₂ nanosheets using Raman spectroscopy and energy-dispersive X-ray spectroscopy. Liquid-phase exfoliated MoS₂ layers were often more defective than mechanically exfoliated MoS₂ and CVD-grown MoS₂ layers. Besides water, the solvent used during liquid exfoliation could be retained between the MoS₂ layers during ultrasonication and annealing/cleaning post-procedures. Raman spectroscopy showed a small blueshift of the E_{2g}¹ and A_{1g} modes in the MoS₂ bulk under a high total absorbed dose (~900 MGy), accompanied by a small broadening of both peaks. The exfoliated MoS₂ layers were less radiation tolerant than the bulk material. Both spectroscopies proved the presence of amorphous carbon in the exfoliated MoS₂ membranes, which could be formed by radiolytic amorphization of residual solvent and retained within the exfoliated nanosheets.

Fox et al. [89] irradiated freestanding mechanically exfoliated MoS₂ few-layers in a helium-ion microscope. Figure 12 shows HRTEM images of a MoS₂ few-layer. The hexagonal structure of the pristine MoS₂ was destroyed to an amorphous state. Energy-dispersive X-ray spectroscopy (EDX) indicated that preferential sputtering of sulfur occurred in the mechanically exfoliated MoS₂ few-layers. Its stoichiometry was modified by the preferential sputtering of sulfur at nanometer scales. It was believed that He²⁺ ions transfer more energy to sulfur atoms than to molybdenum atoms because of the lighter mass of sulfur atoms. Electric properties of the MoS₂ layers were altered to be semiconducting, metallic-like, or insulating depending on doses. When the dose was above

$(2.56 \pm 0.05) \times 10^{18}$ ion/cm², complete removal of material (milling) was observed. Figure 12c shows He²⁺-ion fabricated freestanding nanoribbons in MoS₂ few-layers. The edges of the milled regions may be amorphous or crystalline, depending on He²⁺ beam sizes. MoS₂ layers were milled when the dose was higher than $(1.30 \pm 0.03) \times 10^{18}$ ion/cm². When the dose was below $(1.00 \pm 0.02) \times 10^{17}$ ion/cm², MoS₂ layers were extensively damaged but not completely etched away.

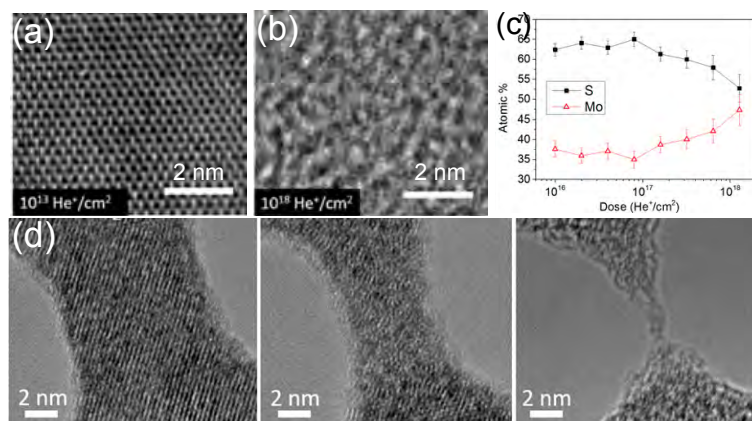


Figure 12. HRTEM image of (a) pristine and (b) He²⁺-irradiated $((1.00 \pm 0.02) \times 10^{18}$ He⁺/cm²) freestanding MoS₂ few-layers [89]. (c) Stoichiometry of an MoS₂ flake under different He²⁺ doses as calculated from EDX analysis. (d) HRTEM images of crystalline (left panel) and amorphous (middle and right panels) MoS₂ nanoribbons fabricated from He²⁺ milling. He²⁺ energy: 30 keV. Reprinted with permission from Reference [89]. Copyright © 2015 American Chemical Society.

Fox et al. [89] also irradiated MBE-grown pristine MoS₂ 6-layers supported on an MgO substrate. With increasing He²⁺ doses, the full width at half maximum (FWHM) of the E_{2g}¹ (the in-plane Mo-S vibration) increased, indicating more in-plane defects during irradiation. The FWHM of A_{1g} peaks decreased with increasing doses, inferring material removal with high He²⁺ doses.

Tongay et al. [90] irradiated mechanically exfoliated MoS₂ mono-layers with a high-energy He²⁺ beam (3.04 MeV) with doses up to 8×10^{13} ions/cm². Upon the He²⁺ particle irradiation at different doses, a new PL peak appeared at 1.78 eV and the integrated intensity of this new peak increased with the irradiation dose. The new peak became stronger and broader after thermal annealing at 500 °C, which thermally introduced sulfur vacancies. The integrated intensity of the main PL peak at 1.90 eV increased three-fold while the PL peak position shifted to a higher energy by 20 meV after the irradiation. Calculations estimated that approximately one defect per 100 unit cells was generated under the 8×10^{13} ions/cm² irradiation dose.

Klein et al. [91] employed 30 keV He²⁺ beams to irradiate MoS₂ mono-layers on SiO₂/Si substrates under various doses of 10¹²–10¹⁶ ions/cm² in a scanning helium-ion microscope. Helium-ion bombardments affected the intrinsic vibrational, luminescent, and valleytronic properties of the atomically thin MoS₂ sheets.

Maguire et al. [92] grew MoS₂ mono-layers on SiO₂ substrates by a CVD technique and irradiated them with He²⁺ at an energy of 30 keV and an angle of incidence of 0°. These irradiation doses ranged from 1×10^{13} ions/cm² to 1×10^{17} ions/cm². With increasing He²⁺ ion doses, the two characteristic Raman peaks quenched and broadened, reflecting the growing disorder with increasing irradiation. A new peak appeared at 227 cm⁻¹ after the irradiation and its intensity increased with increasing doses.

Helium-ion beams were also employed to mill MoS₂ layers [121]. Some regions of MoS₂ few-layers were thinned to mono-layers under 30 keV He²⁺ sub-nanometer ion beams.

2.5. Proton Irradiation

Mathew et al. [85] prepared MoS₂ flakes with a thickness of 200 μm and irradiated them at room temperature using a 3.5 MeV proton ion beam. The Raman spectra of the pristine and irradiated samples at a fluence of 5×10^{18} ions/cm² are shown in Figure 13. A new peak at 483 cm⁻¹ was clearly visible in the irradiated samples. The appearances of the mode at 483 cm⁻¹ along with the broadening of the mode at 452 cm⁻¹ indicated the presence of lattice defects due to proton irradiation of the samples. The FWHM of the E_{2g}¹ and A_{1g} modes did not increase in the irradiated MoS₂, indicating that the lattice structure was preserved in the near-surface region of the irradiated samples. The intensity ratio of A_{1g}/E_{2g} enhanced 16% after the proton irradiation, showing the enhanced interaction of electrons with A_{1g} phonons. X-ray photoelectron spectroscopy indicated there were zone-edge phonons in the irradiated samples and the molybdenum valence of irradiated samples was higher than +4. The irradiation-induced changes of structures and chemical states affected their magnetic moments.

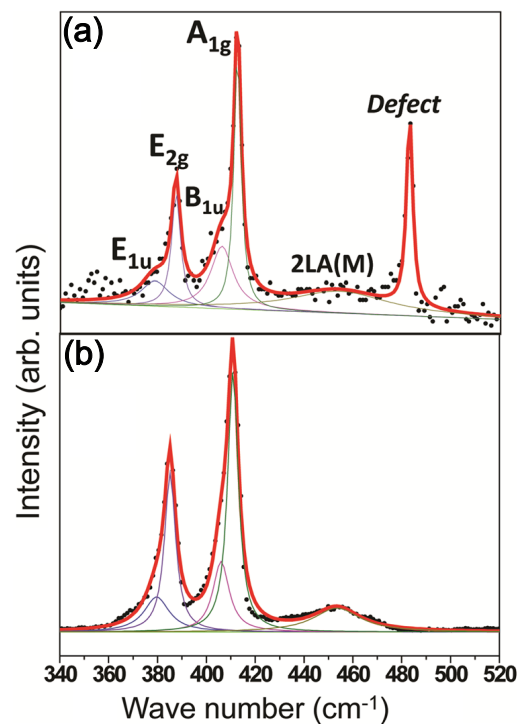


Figure 13. Raman spectra of (a) irradiated and (b) pristine MoS₂ nanosheets under a proton fluence of 5×10^{18} ions/cm² [85]. Reprinted from Reference [85], with the permission of AIP Publishing.

Kim et al. [86] micromechanically exfoliated MoS₂ few-layers from a bulk MoS₂ crystal and fabricated them into MoS₂ field-effect transistor (FET) devices on highly doped Si substrates coated with SiO₂. Source and drain electrodes were made by depositing Au/Ti electrodes. The FET devices were irradiated with a 10 MeV proton beam under fluences of 10^{12} , 10^{13} , and 10^{14} ions/cm². Sufficiently high irradiation fluences decreased the electrical current and conductance of the devices while low dose did not change them significantly. The threshold voltage was shifted towards the positive gate voltage direction under proton irradiation. However, these changes were recovered over a time scale of days. It was believed that proton irradiation changed the SiO₂/MoS₂ interface states, and the interface trap states at the SiO₂/MoS₂ interfaces affected the electrical behaviors of the FET devices.

Wang et al. [87] exfoliated MoS₂ bi-layers, transferred them to silicon nitride membranes, and irradiated them at 100 keV protons (H⁺) with a fluence of 6×10^{14} particles/cm². Figure 14a-b shows the PL spectra of the bi-layers. Both the suspended and substrate-supported bi-layers showed almost

complete suppression of the indirect emission (1.55–1.60 eV) after the irradiation and the emergence of a defect-induced sideband peak at around 1.70 eV. The direct band emission at 1.83 eV increased $1.6\times$ after irradiation while the substrate-supported direct band emission increased by a factor of 2.7. After being annealed at 300 °C for 1 h in argon, the defect-induced sideband peak disappeared for both kinds of bi-layers. The indirect band emission was suppressed after annealing, indicating that the bi-layers underwent an irreversible indirect-to-direct band-gap transition. Wang et al. [87] also examined MoS₂ tri-layers and four-layers. These multi-layers showed similar behaviors as bi-layers.

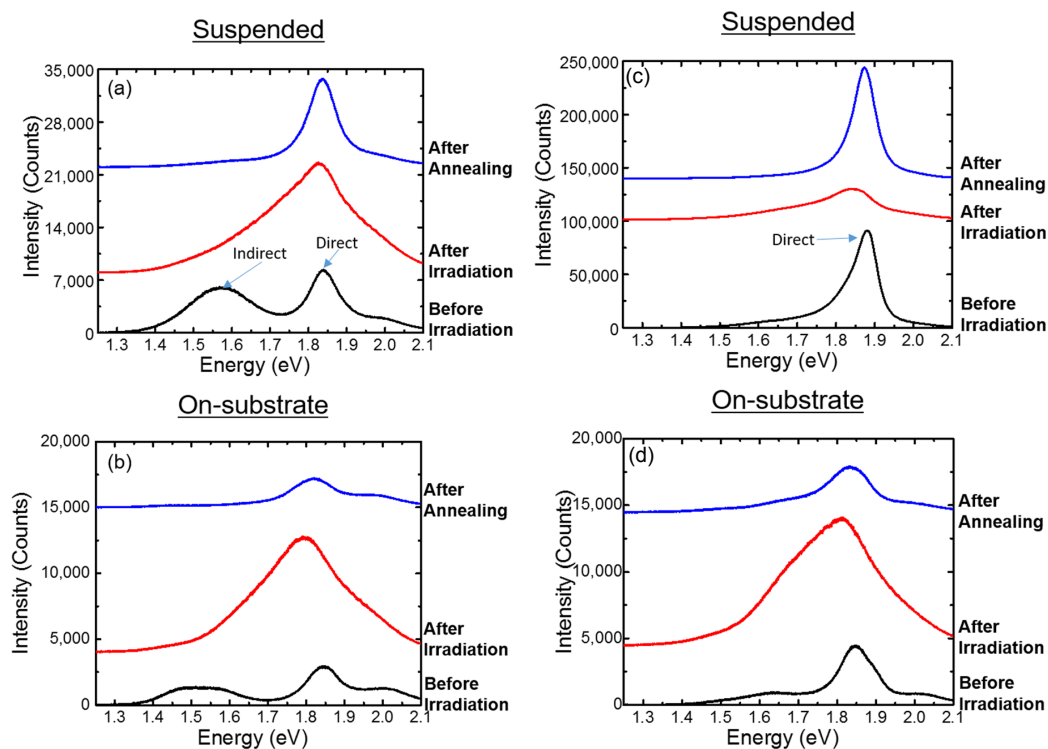


Figure 14. PL spectra of bi-layer MoS₂ (a) suspended over holes and (b) deposited on substrates, and mono-layer MoS₂ (c) suspended over holes and (d) deposited on substrates taken before and after 100 keV proton irradiation with a fluence of 6×10^{14} particles/cm², and after annealing [87]. Reprinted from [87], with the permission of AIP Publishing.

Wang et al. [87] also exfoliated MoS₂ mono-layers and transferred them to silicon nitride membranes with holes. The freestanding MoS₂ mono-layers were then irradiated at 100 keV protons (H⁺) with fluences ranging from 2×10^{12} particles/cm² to 6×10^{14} particles/cm². Figure 14c shows PL spectra of suspending MoS₂ mono-layers after proton irradiation with a fluence of 6×10^{14} particles/cm² with and without annealing, compared with those taken before the irradiation. The intensity of the direct band-gap emission of suspending mono-layers decreased two-fold after the irradiation due to the irradiation-induced defects. The defects caused non-radiative recombination and shortened the lifetime of the photo-excited carriers. On the contrary, the intensity of the direct band-gap emission at 1.85 eV increased after the irradiation for the substrate-supported regions, as shown in Figure 14d. After being annealed at 300 °C for 1 h in argon, the defect-induced sideband peak disappeared in the bi-layers and mono-layers, and the direct band emission reverted to its original pre-irradiated intensity for both kinds of MoS₂ layers.

2.6. Electron Irradiation

Han et al. [122] irradiated MoS₂ single crystals with a thickness of about 50 μm by using high-energy electrons in ambient conditions at room temperature. The electron dose was 300 kGy (6.70×10^{14} electrons/cm²) and the acceleration energy of electrons was 0.7 MeV. There was a

negligible reduction of sulfur XPS intensity compared to the molybdenum XPS intensity of the samples after the irradiation. However, 1T-like defects were generated in the MoS₂ surface, inducing a weak ferromagnetic state at room temperature and improving transport properties.

Han et al. [74] prepared single-crystalline MoS₂ lamellae with a thickness of 100 μm. The lamellae were electron-irradiated in ambient conditions at room temperature. Figure 15 shows HRTEM images of the irradiated samples, showing honeycomb lattices of the MoS₂. The vacancies depended on the acceleration energy and dose. Without irradiation, the lattice of crystalline MoS₂ was a honeycomb with few defects, shown in Figure 15a. After being electron-irradiated with 150 kilogray (kGy) dose at 0.7 MeV acceleration energy, additional defects were produced. Double-sulfur vacancies (V_{S_2}) were more frequently observed than the monosulfur vacancies (V_S) after electron irradiation. Slightly displaced molybdenum atoms were occasionally found, as marked by the red arrow in Figure 15b. Under electron irradiation with a 300 kGy dose at 0.7 MeV acceleration energy, the honeycomb lattice was heavily distorted (Figure 15c) and perfect honeycomb lattices were rarely observed. The numerous V_S and V_{S_2} vacancies distorted the honeycomb lattice and the irradiation considerably decreased the lattice parameters. V_{S_2} defects were more frequently observed under the electron irradiation with a 100 kGy dose at 2.0 MeV. With an increasing dose of 2.0 MeV electrons, the V_S and V_{S_2} concentration increased significantly. Molybdenum vacancies were produced too. The lattice parameters were also significantly increased. Under electron irradiation at higher energy of 10 MeV, different types of defects were produced. Under all irradiation, the vacancy densities increased with the electron irradiation dose and electron energy.

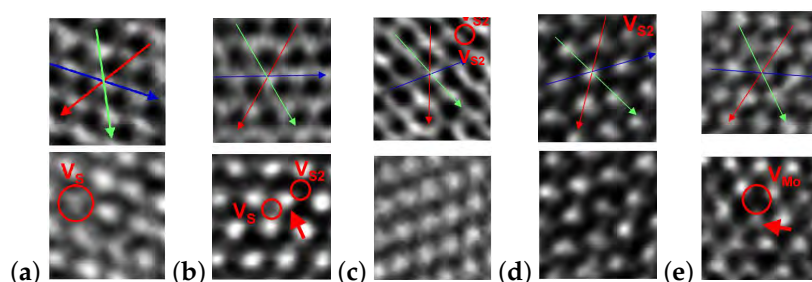


Figure 15. Zoomed HRTEM images of MoS₂ lamellae without electron irradiation (a) and with electron irradiation with (b) 150 kGy dose at 0.7 MeV energy, (c) 300 kGy dose at 0.7 MeV energy, (d) 100 kGy dose at 2.0 MeV energy, and (e) 250 kGy dose at 2.0 MeV energy [74]. The distance between two neighboring molybdenum atoms is 3.12 Å (a top panel), 3.24 Å (b top panel), 2.94 Å (c top panel), 3.23 Å (d top panel), and 3.22 Å (e top panel). Defects are circled. The V_S vacancies in the (a) bottom panel come from the irradiation of the electron beam during observations. Reprinted from [74], with the permission of AIP Publishing.

Rotunno et al. [75] mechanically exfoliated MoS₂ 20-layers and transferred them to carbon-coated copper grids. Figure 16a shows a transmission electron microscopy (TEM) image of a typical MoS₂ few-layer. The multi-layers were then irradiated under a scanning electron microscopy (SEM) beam with an accelerating voltage of 5 keV and an electron-beam current of 50 nA for 15 min. Many crystalline islands were formed throughout the multi-layers after the irradiation, as shown in Figure 16b. The selected-area electron diffraction (SAED) patterns indicated that the islands were metallic molybdenum. Under high-energy (200 keV) electron irradiation, the MoS₂ layers were drastically modified, and their sulfur stoichiometry was changed, inducing the formation of the molybdenum nanoislands, as shown in Figure 16c. In both cases, massive surface sulfur depletion was induced together with the consequent formation of molybdenum nanoislands.

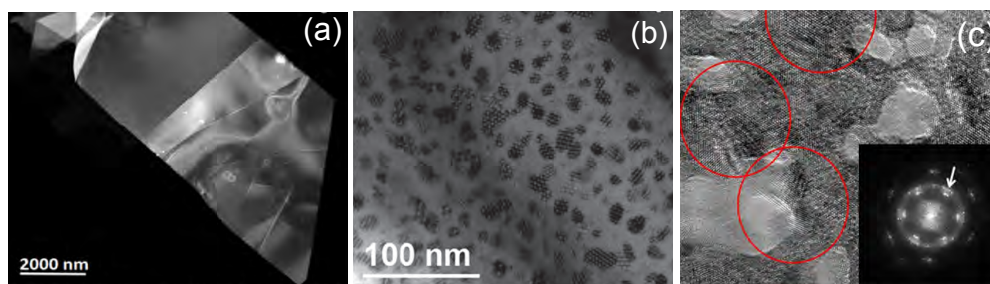


Figure 16. TEM images of (a) un-irradiated, (b) 5 keV electron-irradiated, and (c) 200 keV electron-irradiated MoS₂ 20-layers [75]. The strong reflection spots of the inset SAED come from the MoS_{0.6} layers while the weak ones from metallic Mo. Reproduced with permission under the Creative Commons license. Copyright © 2016 IOP Publishing.

Kim et al. [82] deposited five to seven atomic layers of MoS₂ on a SiO₂/Si wafer at room temperature using the RF magnetron sputtering method. The thickness of the deposited amorphous MoS₂ layers was about 4 nm. The films were then exposed under a collimated electron beam with an energy of 1 keV for 1–10 min at room temperature without any additional heating processes. HRTEM images indicated that the as-deposited MoS₂ was amorphous (left panel in Figure 17a). Under the electron beam irradiation (EBI) of 1 min, the random atoms re-arranged from amorphous to crystalline structure, forming MoS₂ crystal domains with a size about 5 nm (middle panel in Figure 17a). However, longer irradiation time would damage crystalline domains (right panel in Figure 17a) because of the Mo-S bond breaking. The amorphous-crystalline transformation was confirmed by Raman scattering, as shown in Figure 17b. The two prominent Raman peaks of MoS₂, the in-plane mode E_{2g}^1 and the out-of-plane mode A_{1g}^1 , did not appear in the as-deposited film because of its amorphous nature. The peak intensities of the E_{2g}^1 and A_{1g}^1 modes increased dramatically after the electron irradiation at room temperature. Their XPS measurements provided a stronger proof that the amorphous films crystallized under the 1 keV electron irradiation. Figure 17c shows the XPS spectra of MoS₂ samples characterized with an Al-K _{α} ray with an energy of 1486 eV. The Mo-3d peak was de-convoluted into three chemical bonding states of Mo-Mo, Mo-S, and Mo-O in the as-deposited sample. After 1 min of electron irradiation, the Mo-3d spectrum only consisted of two peaks originating from the states of the Mo-S and Mo-O bonds, with dramatically increased peak intensity of the Mo-S bonds. Similarly, the S-2p peak from the as-deposited sample were de-convoluted into S-S and S-Mo bonding while only the S-Mo bond remained in the 1 min electron-irradiated sample. The authors also checked the samples under TEM at 400 keV and then measured the Raman scattering with a 532 nm laser. It was not clear if the amorphous films were changed under the TEM electron-beam irradiation and laser irradiation.

Karmakar et al. [77] investigated the electron irradiation effect of MoS₂ few-layers through micro-Raman scattering. The few-layered MoS₂ samples were prepared by mechanical exfoliation and irradiated under a vacuum of 10×10^{-7} torr. The thickness of the few-layers was about 7 nm, which was equivalent to about ten layers of MoS₂. Figure 18 shows the Raman scattering before and after irradiation. In addition to the in-plane E_{2g}^1 and out-of-plane A_{1g}^1 modes, extra Raman modes appeared after being irradiated under 5 keV, 7 keV, and 10 keV, showing the maximum change under 10 keV irradiation. Obviously, the electron-irradiation-induced defects, resulting in the breaking of inversion symmetry. The 15 keV irradiation did not lead to any changes in the spectra because the electron beam passed the few-layers without creating any damage.

Matsunaga et al. [80] irradiated triangular-shaped MoS₂ mono-layers grown on SiO₂/Si substrates under an electron beam with an acceleration voltage of 15 kV and an areal dose of 280 $\mu\text{C}/\text{cm}^2$ charge. Figure 19a shows an optical image of a mono-layer MoS₂ crystal. The right half region was covered by polymethyl methacrylate (PMMA) and was not electron irradiated. Raman scattering indicated that both regions (with and without irradiation) exhibited the A_{1g}^1 and E_{2g}^1 peaks of MoS₂. However, the two peaks were blue-shifted in the exposed region, as shown in Figure 19b. It was suggested that the electron-beam exposure introduced a local compressive strain in the MoS₂ crystal. The induced

strain would further change the band structure. The PL peak of the exposed left region, ~ 1.85 eV, was blue-shifted 40–50 meV compared with that of unexposed right region (1.81 eV). Figure 19c shows the PL mapping of PL intensity. It was stated that the averaged PL spectrum of the unexposed region of the MoS₂ mono-layer could be characterized by a broad peak at 1.81 eV while the exposed region of the same MoS₂ sample showed a narrower feature at 1.85 eV, corresponding to a blue shift of 40–50 meV.

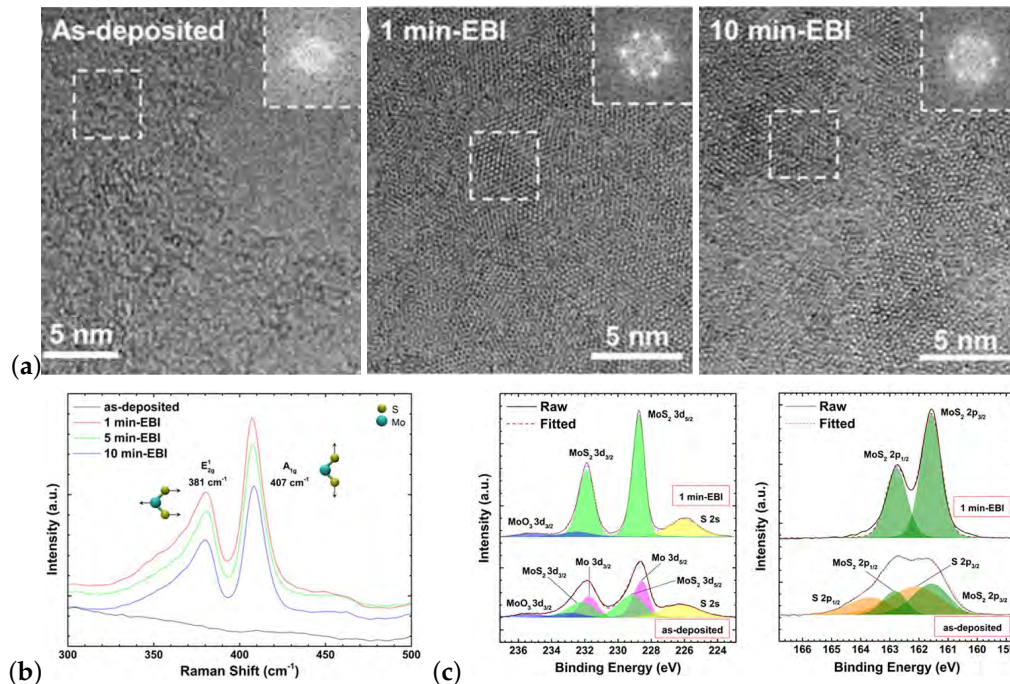


Figure 17. (a) Plan-view HRTEM images of the as-deposited sample, 1 min EBI-treated sample [82], and 10 min EBI-treated sample [82]. Insets show fast Fourier transformation (FFT) patterns of the areas marked as dashed squares. (b) Raman spectra of as-deposited and EBI-treated MoS₂ samples for an irradiation time of 1, 5, and 10 min [82]. (c) Mo-3d XPS spectrum (left panel) and S-2p XPS spectrum (right panel) from as-deposited and 1 min electron-irradiated samples [82]. Reproduced with permission under the Creative Commons Attribution 4.0 International license.

Liu et al. [81] prepared a MoS₂ mono-layer by micromechanical cleavage, as shown in Figure 20a. The well-crystalline MoS₂ mono-layer was then exposed in a vacuum under a 80 keV electron beam with an intensity of 40 A/cm². Initial defects and holes were induced in the MoS₂ sheet once exposed to the electron beam (Figure 20b). After a 81 second exposure under the electron irradiation, the small holes spread rapidly (Figure 20c) and extended into big holes with diameters of 3–6 nm (Figure 20d) after a 103 s irradiation. The MoS₂ mono-layer converted to Mo₅S₄ nanoribbons after long-term electron irradiation.

Komsa et al. [78] prepared freestanding single-layer MoS₂ samples by mechanical exfoliation of natural MoS₂ bulk crystals, and observed a MoS₂ sheet under an 80 keV electron beam in a vacuum on an aberration-corrected HRTEM. It was experimentally observed that the top and bottom sulfur atoms were removed under the 80 keV electron beam and vacancies were generated in the MoS₂ mono-layers under the electron irradiation. The sulfur vacancies agglomerated into line defects due to migration of the defects [123].

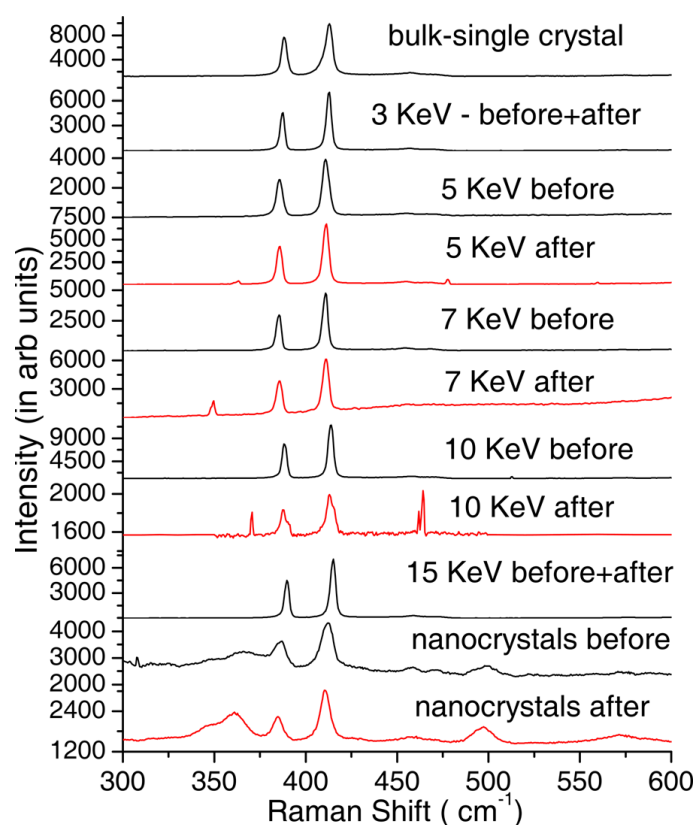


Figure 18. Micro-Raman spectra of 10-layered MoS₂ sheets before (black curves) and after (red curves) irradiation [77].

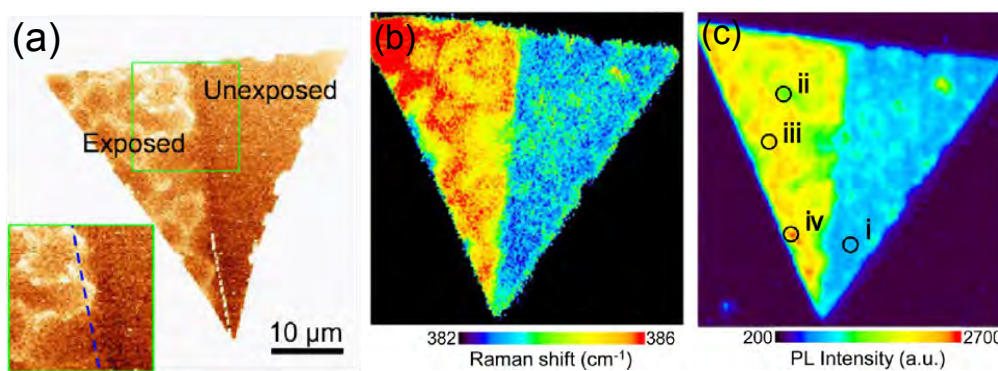


Figure 19. (a) Optical image of a mono-layer MoS₂ crystal. The electron-beam exposure was performed on only the left side of the crystal while the right side is covered to avoid electron exposure. (b) Raman mapping of the MoS₂ crystal shown in (a), indicating the Raman shift of the E_{2g}^1 peak as a function of position. (c) PL mapping of the MoS₂ crystal at a wavelength of 670 nm. Reprinted with permission from Reference [80]. Copyright © 2016 American Chemical Society.

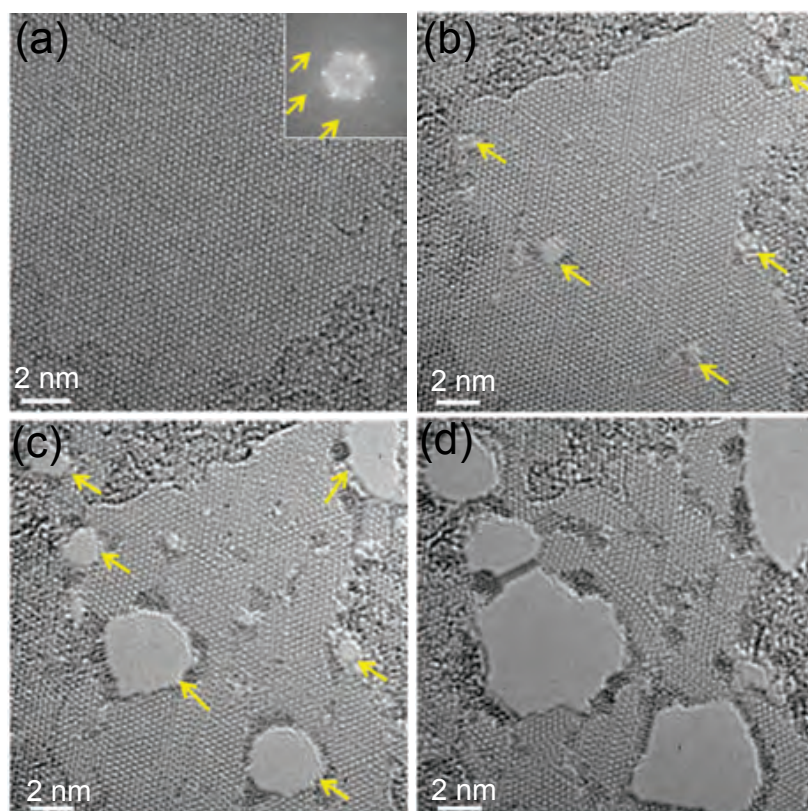


Figure 20. HRTEM images of a MoS₂ mono-layer under electron irradiation [81]. (a) MoS₂ mono-layer without irradiation. Inset: fast Fourier transformation (FFT) image. (b) The initial MoS₂ sheet with small irradiation-induced vacancies as highlighted by the arrows. (c) Large holes extended from the small vacancies upon electron irradiation of 108 s. (d) Larger holes extended from the small vacancies upon electron irradiation of 261 s. Reprinted with permission under a Creative Commons license.

Parkin et al. [79] prepared MoS₂ single-crystalline mono-layers by CVD method and irradiated them with 200 keV electrons in an aberration-corrected TEM. Most generated defects were single sulfur vacancies. The irradiation-induced defects were quantitatively related to the electron dose with the actual defect concentration. Figure 21 shows the defect-induced stoichiometry as a function of electron dose. The elemental composition within the illuminated region was measured by electron X-ray dispersive spectroscopy (EDS). The EDS measurements indicated that the S/Mo atomic ratio was very close to the stoichiometric 2:1 ratio before electron irradiation. The M/Mo ratio decreased with the irradiation dose because of the sulfur removal under electron irradiation. It should be noted that the EDS intensity of the molybdenum signal remains constant during the irradiation, supporting the fact that the main effect of irradiation was to create sulfur vacancies while molybdenum atoms were much more difficult to be sputtered.

Electron-irradiation-induced phase transformation of MoS₂ layers was also reported at high temperatures, such as 400–700 °C in a vacuum [76]. Electron irradiation initiated the phase transition of 2H-MoS₂ at high temperatures, and the transformation ratio increased with increasing electron doses above 40×10^6 – 100×10^6 electrons /nm², depending on the temperature. It was also found that MoS₂ layers were damaged when the total electron dose exceeded 5.0×10^8 – 1.1×10^9 electrons/nm² with the accelerating voltage of 60 kV.

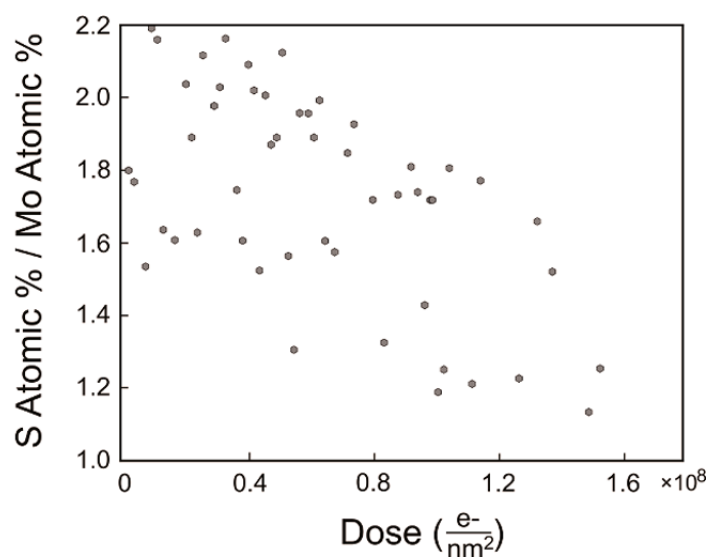


Figure 21. EDS measured stoichiometry, showing an initial value of $S/Mo = 2.01 \pm 0.07$, as expected for CVD-grown MoS_2 where a small amount of sulfur vacancy ($\sim 0.5\%$) can be present after growth [79]. Reprinted with permission from Reference [79]. Copyright © 2016 American Chemical Society.

2.7. Plasma Irradiation

Plasma has been employed to remove impurities and contaminants from surfaces by the collision energy of gas molecules and the chemical action on impurities and contaminants. Various gases (such as argon, oxygen, hydrogen, and nitrogen, as well as their mixtures) have been employed to carry out the cleaning procedures. The plasma is generated by using high-frequency voltages (typically kHz-MHz) to ionize the working gases. The activated species in plasma, including atoms, molecules, ions, electrons, free radicals, metastables, react with contaminants on surfaces. Short-wave ultraviolet (vacuum UV), whose energy is very effective to break most organic bonds of surface contaminants, is produced in plasma too. The technique has been utilized to modify surfaces of MoS_2 few-layers in recent years.

2.7.1. Active Nitrogen N_2^*

Michra et al. [98] investigated oxygen-plasma-irradiated MoS_2 mono-layers deposited on sapphires at $450^\circ C$. Figure 22 shows Raman scattering of irradiated MoS_2 mono-layers. Raman A_{1g} mode shifted 1.79 cm^{-1} towards a higher wavenumber and E_{2g}^1 1.11 cm^{-1} towards a lower wavenumber after 3 min of N_2 plasma irradiation. The peak intensity ratio $I_{A_{1g}}/I_{E_{2g}^1}$ and FWHM of the E_{2g}^1 peak increased with plasma irradiation time. XPS investigations indicated that N-Mo bonds formed during the irradiation and the binding energies (calculated from $Mo-3d^{5/2}$, $Mo-3p^{3/2}$, and $S-2p^{3/2}$ peaks) shifted towards lower binding energy after N_2^* irradiation. The valence band maximum (VBM) reduced to 0.9 eV after 1 min of irradiation and 0.5 eV after 3 min of irradiation from 1.0 eV of pristine MoS_2 mono-layer.

Azcatl et al. [124] doped MoS_2 with nitrogen through a remote N_2 plasma surface treatment. Nitrogen covalently bonded to MoS_2 upon nitrogen plasma exposures and substituted chalcogen sulfur of MoS_2 . The nitrogen doping converted MoS_2 to *p*-type and changed electrical properties. The nitrogen concentration in the doped MoS_2 was controlled through adjusting N_2 plasma exposure time. XPS measurements indicated that binding energies of $Mo-3d_{5/2}$ and $S-2p_{3/2}$ decreased with increasing exposure time.

Mono-layer MoS_2 heterojunctions, such as intrinsic GaN/*p*-type MoS_2 heterojunction, were also irradiated by N_2 plasma under UHV conditions [98]. The values of VBM were reduced to 0.5 eV for N_2^* irradiated MoS_2 layers.

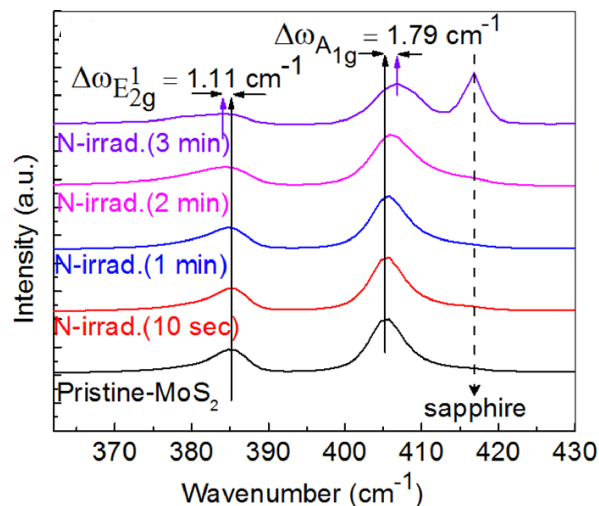


Figure 22. Raman spectra of pristine and N_2^* -irradiated MoS_2 mono-layers [98]. Reprinted from Reference [98], with the permission of AIP Publishing.

2.7.2. Active Oxygen O_2^*

Oxygen plasma species include ionized oxygen atoms O^+ , excited oxygen atoms O^* , ionized oxygen molecules O_2^+ , metastable excited oxygen molecules O_2^* , ozone O_3 , ionized ozone O_3^+ , excited ozone O_3^* , and free electrons. Therefore, oxygen plasma can effectively clean and etch MoS_2 2D materials, introducing defects and doping oxygen to MoS_2 2D layers.

Nan et al. [125] treated MoS_2 layers under oxygen plasma irradiation with 13.56 MHz and 5 W under 5 Pa. As shown in Figure 23 and the inset, the PL intensity increased with increasing plasma irradiation time. The PL enhancement could be increased as high as 100 times over. Considering the unchanged Raman scattering and XPS information, it was concluded that oxygen plasma introduced defects and oxygen bonding in MoS_2 , enhancing PL intensity.

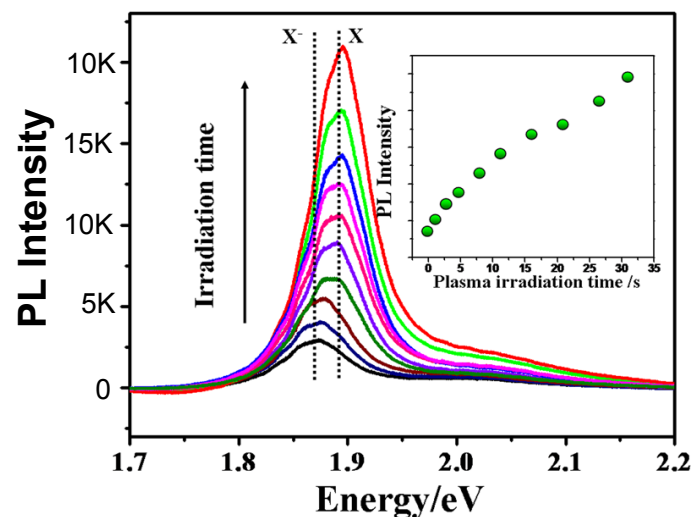


Figure 23. PL spectra of mono-layer MoS_2 after oxygen plasma irradiation with different durations [125]. The change of PL intensities with the plasma irradiation time is shown in the inset. Reprinted with permission from Reference [125]. Copyright © 2014 American Chemical Society.

Chen et al. [126] treated MoS_2 multi-layers under oxygen plasma in a reactive ion etcher. Initial n -type MoS_2 layers were selected-area doped to p -type, forming p - n junctions in MoS_2 . The fabricated

highly rectifying diodes exhibited high forward/reverse current ratios and a superior long-term stability at ambient conditions.

Kang et al. [127] treated MoS₂ mono-layers with oxygen plasma. The photoluminescence evolved from a higher intense to completely quenched with increasing plasma exposure time because of a direct-to-indirect band-gap transition. The MoS₂ lattice was distorted after oxygen bombardment and MoO₃ disordered regions were generated in the MoS₂ flakes.

Islam et al. [128] deposited MoS₂ mono-layers (mechanically exfoliated from crystals) on Si/SiO₂ wafers and exposed them under oxygen plasma for several seconds. The plasma treatments were carried out at a power of 100 W operating at 50 kHz, using a gas mixture of oxygen (20%) and argon (80%) with a pressure of 250–350 mTorr. Raman spectroscopy and XPS spectroscopy indicated that MoS₂ mono-layers were oxidized and MoO₃ was produced in the reaction, $2\text{MoS}_2 + 7\text{O}_2 \rightarrow 2\text{MoO}_3 + 4\text{SO}_2$. The resulting MoO₃-rich domains significantly decreased the mobility and conductivity of the fabricated MoS₂ mono-layer devices.

Ye et al. [129] exposed CVD-grown MoS₂ mono-layers under oxygen plasma at a pressure of 10 Torr with oxygen gas. Figure 24 shows the morphologies of MoS₂ exposed to oxygen plasma for 10 s, 20 s, and 30 s. After 10 s of oxygen plasma treatments, short and isolated cracks were observed on the continuous basal plane. Angles of those connected cracks were around 120°. After 20 s of oxygen plasma treatments, cracks became longer and were connected to each other, forming a continuous network. When treated for 30 s, the widths of the cracks were further enlarged, most angles between the interconnected cracks were 120°, and the MoS₂ was decomposed into even smaller fragments with a greater number of exposed edges. The structural change significantly decreased the intensity of A_{1g} and E_{2g}¹ Raman modes of the MoS₂ mono-layers, and shifted the A_{1g} mode to shorter wave-numbers and the E_{2g}¹ mode to longer wave-numbers. The exposure also decreased the PL intensity. The changes of the Raman and PL spectra indicated that oxygen plasma can lower the MoS₂ crystal symmetry and increase the lattice distortion, which can be attributed to the defects that may benefit MoS₂ as electrochemical catalyst.

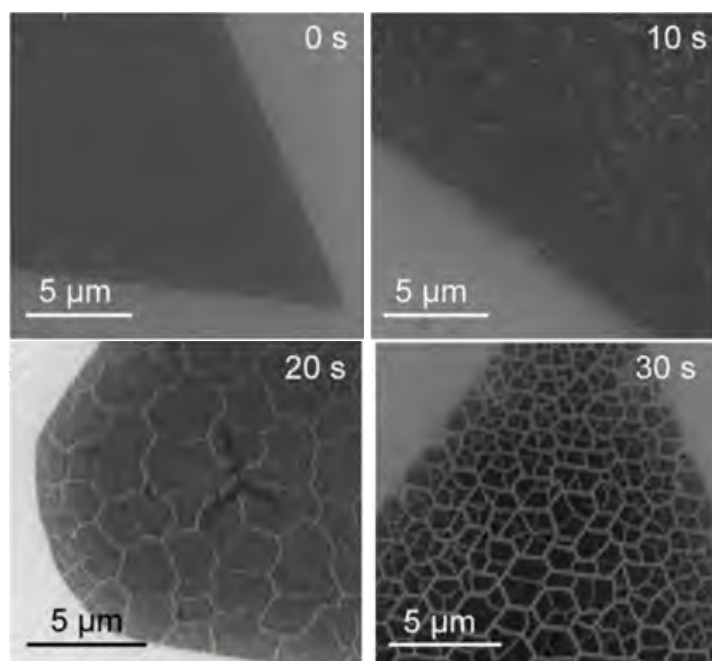


Figure 24. SEM images of CVD-grown MoS₂ mono-layers with oxygen plasma treatments for 0 s, 10 s, 20 s, and 30 s oxygen plasma exposure [129]. Both the density and width of the cracks increased with exposure time. Reprinted with permission from Reference [129]. Copyright © 2016 American Chemical Society.

Dhall et al. [130] treated MoS₂ few-layers (15 layers with approximately 12 nm thickness) in oxygen plasma for 3 min. The plasma was generated by flowing air past an electrode supplied with 20 W of RF power at 200 mTorr. The PL efficiency of the few-layers was increased after the plasma treatments.

Kim et al. [131] grew triangular MoS₂ mono-layers on SiO₂/Si substrates by CVD technique. The MoS₂ mono-layers were then subjected to plasma-oxygen treatment for times ranging from 10 s to 120 s. Ultra-high pure oxygen gas (99.9999%) was activated by a RF plasma cell, and the working pressure was 1.3×10^{-3} Pa under an ultra-high pure oxygen gas flow of 2 sccm. Optical properties of the mono-layers, such as PL and Raman scattering, changed with treatment time. Figure 25a shows optical images of the pristine MoS₂ mono-layer and these MoS₂ mono-layers treated with oxygen plasma for 10 s, 30 s, 60 s and 120 s. Figure 25b shows integrated PL intensity mapping images obtained from each of the mono-layers. The integrated PL intensity decreased with the oxygen plasma treatment time. Figure 25c shows the peak position of the main PL peak. The main peak position of the PL spectra gradually red-shifted from 674 nm to 692 nm with an increasing oxygen plasma treatment duration. It was suggested that shallow defect states were generated by the oxygen plasma treatments.

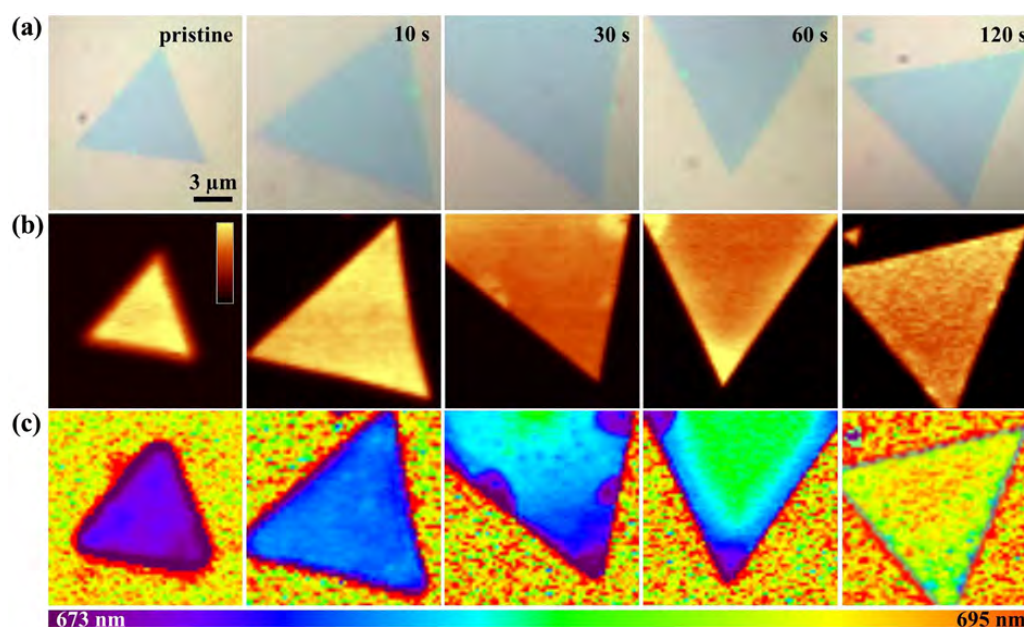


Figure 25. (a) Optical images, (b) confocal PL spectral intensity mapping images, and (c) spectral peak mapping images of pristine and treated MoS₂ mono-layers [131]. The color represents PL intensity in (b) and wavelength of PL peak in c. Reprinted from Reference [131]. Copyright © 2015, with permission from Elsevier.

2.7.3. Active Hydrogen H₂*

Ye et al. [129] exposed CVD-grown MoS₂ mono-layers in hydrogen plasma at different temperatures (400–700 °C), as shown in Figure 26. The MoS₂ mono-layer were treated to expose more active sites in the basal plane of MoS₂ and to improve catalytic activity. No significant changes were observed on the MoS₂ when the annealing temperature was 400 °C. The MoS₂ was then H₂-treated at 500 °C and small triangular holes with sizes around 1–4 μm appeared. High-density holes with sizes around 10–20 nm were omnipresent in the basal plane of MoS₂. High-density triangular-shaped holes became the prominent part in the original mono-layer MoS₂ at 600 °C. 700 °C H₂-treatments led to severe MoS₂ decomposition. The hydrogen plasma treatments decreased the peak intensities of Raman scattering and PL spectra, indicating that hydrogen treatments could increase the defects and edges in mono-layer MoS₂.

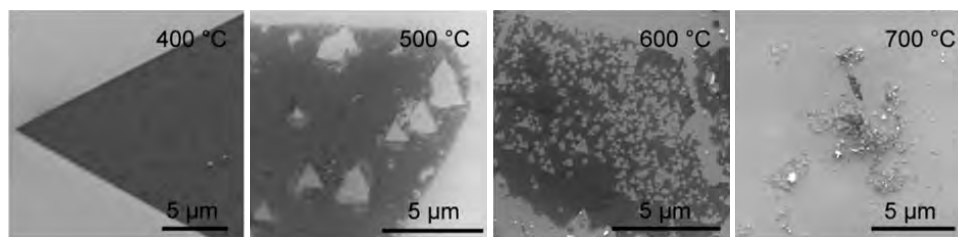


Figure 26. SEM images of mono-layer MoS₂ with 400 °C, 500 °C, 600 °C, and 700 °C H₂ annealing, respectively, showing the appearance of small triangle holes [129]. Reprinted with permission from Reference [129]. Copyright © 2016 American Chemical Society.

2.7.4. Other Molecules

Fluoride

Chen et al. [126] treated MoS₂ multi-layers under fluoride plasma (SF₆, CHF₃, and CF₄) for selected-area *p*-doping to form *p-n* MoS₂ junctions and diodes.

Chlorine

Murray et al. [116] irradiated exfoliated MoS₂ few-layers (5–15 layers) under low-energy Cl (200 eV and 1×10^{13} – 10^{15} ions/cm²). The natural *n*-type MoS₂ layers were doped to *p*-type and the electric conductivity was reduced after irradiation.

Phosphorus

Nipane et al. [132] reported a compatible, controllable, and area selective phosphorus plasma immersion ion implantation process for *p*-type doping of mechanically exfoliated MoS₂ layers using PH₃–He plasma. Homogeneous *p-n* MoS₂ junction diodes were fabricated.

Gallium

Mono-layer MoS₂ heterojunctions, such as intrinsic GaN/*p*-type MoS₂ heterojunction, were also irradiated by Ga plasma under UHV conditions [98]. The values of VBM were reduced to 0.2 eV for Ga-irradiated MoS₂ layers.

Combination

Jadwiszczak et al. [133] exposed mechanically exfoliated MoS₂ few-layers to an O₂–Ar plasma (O₂:Ar = 1:3) for 2–28 s. The frequency of the plasma was 13.52 MHz. An oxide phase was generated under the plasma exposure, changing the electrical conductivity and carrier mobility of the 2D materials.

Mishra et al. [98] irradiated MoS₂ under N₂^{*} plasma for 1–3 min and then under Ga flux. The VBM was changed.

Bhimanapati et al. [134] treated MoS₂ vertical layers in UV–ozone. The ozone treatment increased super wettability and enhanced hydrogen evolution reaction of the material by changing edge chemistry and surface defects.

Nguyen et al. [19] treated MoS₂ layers in UV–ozone and then fabricated the layers into organic photovoltaic cells. The open-circuit voltage, fill factor, and power conversion efficiency increased significantly compared with un-irradiated MoS₂-based solar cells.

3. Electromagnetic Irradiation

Electromagnetic irradiation refers to the waves of the electromagnetic field, including gamma rays, X-rays, ultraviolet, (visible) light, infrared, microwaves, and radio waves. The frequency and wavelength of the electromagnetic irradiation is shown in Figure 3.

3.1. Gamma-ray Irradiation

It is generally accepted that MoS₂ macroscopic materials are stiff under gamma-ray irradiation. There is little literature on γ -irradiated bulks. It was reported that MoS₂ powders were resistant to a γ -ray irradiation with a dose of 5×10^9 R (1.29×10^6 C/kg) [105].

Lee et al. [106] mechanically exfoliated MoS₂ 2D layers (50–132 layers) and exposed them to 5000 γ -ray photons with 662 keV. It was found that the resonance frequency of the layers upshifted immediately after γ -ray exposure and returned to their initial frequency after 60 h. The procedure was repeatable. It was assumed that γ -ray photons generated charges on MoS₂ and caused electrostatic forces between MoS₂ and substrates, resulting in electrostatic tension and deflection of MoS₂ layers. The MoS₂ multi-layers were stiff under the γ -ray and showed no irradiation damage.

Ozden et al. [107] prepared MoS₂ multi-layers (5–8 layers) through the vapor phase sulfurization and exposed the layers to a γ -ray irradiation of ⁶⁰Co source (γ -ray energy: 1.1732 MeV and 1.3324 MeV) with a dose of 120 Mrad. The irradiation was carried out at room temperature in an ambient atmosphere. The X-ray photoelectron spectra indicated that MoS₂ layers were converted to molybdenum oxide (MoO_x) after the irradiation. It is plausible that the γ -ray displaced or knocked out S atoms while leaving molybdenum atoms unaffected. Maybe the as-produced sulfur vacancies were filled with oxygen atoms to form MoO_x.

3.2. X-ray Irradiation

There are few reports on X-ray irradiation of MoS₂. Only one paper [108] reported that MoS₂ mono-layers were irradiated with 10 keV X-rays with varying total ionizing doses. It was reported that the MoS₂ mono-layers were robust to X-ray radiation, withstanding doses of up to 6 Mrad doses without any noticeable degradation of optical properties. It is generally accepted that X-rays do not affect MoS₂ few-layers.

Zhang et al. [135] fabricated single-layer MoS₂ FETs and irradiated them under 10 keV X-ray exposure. At room temperature in air, the drain current of the devices decreased significantly under X-ray irradiation up to 10 Mrad. Effective threshold voltage and mobility were degraded with X-ray irradiation dose. It stated that the degradation was consistent with the generation of negatively charged surface states during the X-ray exposure.

3.3. Ultraviolet Light Irradiation

Azcatl et al. [109] treated MoS₂ crystals under ultraviolet–ozone exposures at room temperature. Oxygen–sulfur bonds were formed at the top sulfur layer of the MoS₂ surface without breaking sulfur–molybdenum bonds. Li et al. [136] investigated optical behaviors of azobenzene-functionalized MoS₂ mono-layers and exfoliated multi-layers on Au substrates. It was reported that UV light could tune doping and the Fermi level of the hybrid structures. Lu et al. [137] irradiated liquid-exfoliated MoS₂ nanosheets in aqueous solutions and found that the MoS₂ layers were oxidatively etched because of photon-induced powerful OH* radicals.

Singh et al. [138] illustrated multilayer MoS₂ FETs under ultraviolet light in N₂ atmospheres. The multi-layers were micromechanically exfoliated from natural MoS₂ crystals and deposited on SiO₂ coated silicon. The wavelength of the UV light was 220 nm and the average intensity was 10 mW/cm². Nitrogen gas alone did not affect the electrical properties of MoS₂ nanosheets, but nitrogen gas in the presence of UV light remarkably affected the electrical properties of MoS₂ nanosheets. Charge-carrier mobility, carrier density, and drain current were enhanced after exposure to nitrogen gas under UV light irradiation because of a possible doping effect. Detailed investigations [139] showed that the charge-carrier density of single-layer, bi-layer, and few-layer MoS₂ nanosheets were reversibly tuned with nitrogen and oxygen gas in the presence of ultraviolet light. The device performance was adjusted by exposure to gases in the presence of UV light.

McMorrow et al. [110] fabricated single-layer and multilayer MoS₂ (mechanically exfoliated) on Si substrates into FETs. It was found that the electron mobility increased with UV exposure up to 3.4×10^{10} – 2.2×10^{13} photons/cm² in a vacuum. Raman spectroscopy showed no significant crystalline radiation damage or oxidation degradation under UV exposure. Irradiation-hard MoS₂ FET devices are expected.

3.4. Visible Light Irradiation

Liu et al. [140] tested photocatalytic performance of N-doped MoS₂ nanoflowers under visible light. It was reported that the N-doped MoS₂ nanoflowers showed excellent photocatalytic activities and durability on the elimination of the organic pollutants under visible light irradiation.

Laser has been widely employed in Raman scattering of MoS₂ few-layers. Laser has also been used to thin multilayered MoS₂ down to a single-layer two-dimensional crystal [141,142] (power density up to 80–140 mW/μm²) and generate ripples of MoS₂ [142,143]. It is reported that the upper atoms of MoS₂ layers can be removed by high-power lasers because of laser ablation [112,141].

Early investigation indicated that natural MoS₂ crystals do not undergo any kind of significant laser-assisted oxidation when exposed to high laser power (up to 32,000 W/cm²) (wavelength: 632.8 nm) [144] while their Raman mode intensity changes slightly with laser power. For microcrystalline MoS₂ powders, Raman scattering indicated that MoS₂ oxidized to MoO₃ under a high-power laser. Raman mode intensity and position were also significantly affected by the laser power.

Paradisanos et al. [113] mechanically exfoliated MoS₂ few-layers from a bulk natural crystal and subsequently deposited them on Si/SiO₂ wafers, irradiated the few-layers under a pulsed laser with 800 nm wavelength and 1 kHz repetition rate. No modification of MoS₂ mono-layers was observed up to a certain single-pulse fluence of 50 mJ/cm² (2.5 mW) while damage occurred beyond the fluence via the material ablation. Further work indicated that MoS₂ mono-layers were practically unaffected by a low-power (600 μW) pulsed laser irradiation when exposed to 10³ pulses at a fluence of 20 mJ/cm² (lower than the damage threshold). However, the MoS₂ mono-layers were damaged upon 10⁵ pulses at 20 mJ/cm². The A_{1g} and E_{2g} intensities were almost constant with pulse times, then rapidly decreased at a critical exposure time. The abrupt decrease possibly came from ablation and eventual sublimation of the MoS₂ atoms.

Gu et al. [111] in situ studied Raman scattering of MoS₂ layers during the laser thinning of MoS₂. Due to the high surface-area-to-volume ratio, thinner MoS₂ layers are less stable and easier to decompose under high-power laser irradiation because of laser-induced thermal effects and sublimation.

Tran Khac et al. [145] irradiated MoS₂ layers under laser power of 1 mW, 5 mW, and 10 mW for an exposure time of 60 s. No significant changes were observed in topographic images of the irradiated regions under the 1 mW laser. However, significant amounts of particles or adsorbates were formed on the MoS₂ surface after irradiated under 5 mW and 10 mW lasers.

To minimize thermal effects on atomically thin MoS₂ during Raman spectral measurements, low laser powers (0.14 mW to 2 mW) are usually employed [145] to avoid potential laser-induced local surface temperatures.

Lu et al. [112] employed a focused laser beam to directly pattern MoS₂ mono-layers and few-layers. Focused laser beam irradiation modified and thinned MoS₂ layers to create well-defined structures and controllable thickness.

Alrasheed et al. [146] used a 532 nm laser to irradiate mechanically exfoliated MoS₂ few-layers (less than 5 layers) on SiO₂/Si substrates. The power ranged between 0.93 and 8.3 mW and the treatment time was 0.01–180 s. In ambient conditions, MoS₂ nanosheets were etched and amorphous MoS₂ redeposited on the nanosheets at low laser powers while the few-layers were oxidized and MoS₂ nanoparticles formed at high laser powers. The nanoparticle formation and oxidation were dependent

on the number of layers and laser exposure time. The Raman intensity and Raman peak width changed with laser treatments, as shown in Figure 27.

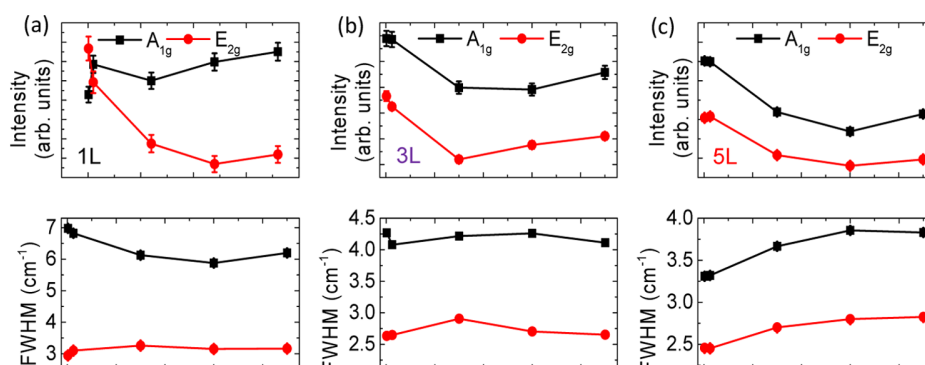


Figure 27. Raman intensity and linewidth (FWHM) of (a) mono-layer-ed (1L), (b) tri-layer-ed (3L), and (c) 5-layer-ed (5L) MoS₂ nanosheets laser-treated in ambient conditions. Reprinted with permission from Reference [146]. Copyright © 2018 American Chemical Society.

3.5. Infrared Light Irradiation

Fan et al. [30] irradiated lithium intercalated 1T MoS₂ layers with thickness of a few microns under a near-IR laser (780 nm) in air at ambient temperature. The MoS₂ layers were completely converted to 2H counterpart under the irradiation.

2H MoS₂ multi-layers were grown through pulsed mid-infrared laser deposition [147] (wavelength of 7.0–8.2 μm). No any IR damage was reported.

3.6. Terahertz Wave Irradiation

MoS₂ multi-layers were fabricated into terahertz modulators [148] applied in high-speed communications. Terahertz conductivities of MoS₂ few-layers were experimentally measured [149,150] from THz spectroscopy. However, there was no report on terahertz damage on MoS₂. Theoretical simulations indicated that the THz absorption of mono-layer MoS₂ was very low and the maximum THz absorption of mono-layer MoS₂ was approximately 5% [151]. The sum of reflection and absorption losses of mono-layer MoS₂ was lower than that of graphene by one to three orders of magnitude.

3.7. Microwave Irradiation

Few-layer MoS₂ were fabricated into two-dimensional nanoelectromechanical systems (NEMS) as ultralow-power, high-frequency tunable oscillators and ultrasensitive resonant transducers [152]. These devices can operate in the very high frequency band (up to ~120 MHz). Ultra-thin MoS₂ was also fabricated to MoS₂ transistors operating at gigahertz frequencies [153,154]. All these devices worked at microwave range. Therefore, it is necessary to characterize the microwave damages to MoS₂ few-layers.

It was reported that microwave can accelerate catalytic reactions [155] because of the formation of hot-spots within catalysts. However, no significant differences were detected between microwave irradiated MoS₂ catalysts (size in microns) and untreated MoS₂ during the sulfating reaction [155].

Zhao et al. [156] irradiated MoS₂ powders under a microwave (1 kW power, 2450 MHz) at 200 °C. It was reported that the (001) basal planes of the MoS₂ crystal structure were cracked into (100) edge planes under microwave irradiation, creating additional active edge sites. The Raman intensity of microwave irradiated materials increased significantly after microwave treatments. The irradiated MoS₂ could capture Hg⁰ efficiently because of the microwave-induced cracks.

Xu et al. [31] treated chemically exfoliated MoS₂ nanosheets in an inert nonpolar solvent of 1,2-dichlorobenzene under 2.45 GHz microwave irradiation at 130 °C in an inert atmosphere, with an output power of 500 W. 2H MoS₂ nanosheets converted to the 1T phase in minutes.

4. Other Irradiation

4.1. Ultrasonic Wave Irradiation

MoS₂ nanosheets have been prepared by ultrasonication through liquid exfoliation technique [19,41,46,71]. The physical properties were affected by ultrasonication conditions. For example, Gao et al. [157] sonicated MoS₂ powders in N,N-dimethylformamide for 2–10 h to chemically exfoliate MoS₂ nanosheets. Crystalline MoS₂ few-layers were produced after 2 h sonication and the size of the nanosheets decreased gradually with increasing sonication time. The exfoliated MoS₂ nanosheets showed ferromagnetic properties at room temperature, in contrast to pristine MoS₂ bulks which showed diamagnetism only. The saturation magnetizations of the ultrasonicated nanosheets increased with the ultrasonication time and the decreasing crystalline size.

MoS₂ nanomaterials were also prepared by ultrasonically slurrying molybdenum hexacarbonyl and sulfur in 1,2,3,5-tetramethylbenzene (isodurene) with a high-intensity ultrasound (20 kHz) under Ar atmosphere [158]. The nanostructured MoS₂ had a higher surface area and showed higher catalytic activities for thiophene hydrodesulfurization.

4.2. Thermal Irradiation

MoS₂ bulks sublime at 450 °C and melt at 2375 °C. MoS₂ crystals are not stable in the presence of oxygen, resulting in MoO₃. It was reported that the material oxidized at 315–375 °C in air and converts to MoO₃ at 400 °C [144].

MoS₂ mono-layers are not very stable at ambient conditions either. Peto et al. [159] examined atomic-resolution STM images of the basal plane of mechanically exfoliated MoS₂ mono-layers after one month and one year of ambient exposure (in air, at room temperature and ambient light). STM measurements clearly revealed modifications in the atomic structure of the MoS₂ basal plane during the ambient exposure. New point-defects were formed after one month of the ambient exposure and the defect concentration increased 20–30 times. The point-defects increased 100–500 times after one year of exposure. The oxidation of MoS₂ basal planes yielded 2D MoS_{2-x}O_x layers.

Chen et al. [117] annealed the liquid-exfoliated MoS₂ mono-layers on various substrates (SiO₂, Au, graphene, BN, and CeO₂) in a vacuum. Thermal annealing did not introduce any noticeable defects into MoS₂ layers up to 450 °C and MoS₂ remained stable, as shown in Figure 11. Other group reported that thermal annealing in a vacuum caused S vacancies in MoS₂ at 500 °C [90].

Donarelli et al. [160] annealed MoS₂ crystals in UHV. Single sulfur vacancies were generated in bulks while the S/Mo ratio in the bulk did not change with the annealing temperature up to 400 °C. They also examined the liquid-exfoliated MoS₂ few-layers. The S/Mo ratio of MoS₂ few-layers gradually decreased once the annealing temperature increased up to 400 °C. Two kinds of sulfur vacancies (single and double) were introduced in the molybdenite layers. The threshold for the formation of double vacancies typically occurred upon thermal annealing at 200 °C.

Nan et al. [125] mechanically exfoliated MoS₂ mono-layers from bulk crystals and transferred them to Si wafers with SiO₂ capping layer. The mono-layers were then annealed at temperature of 350 °C or 500 °C for 1 h in a vacuum (0.1 Pa). Figure 28a shows PL intensity image of an as-prepared MoS₂ mono-layer, which was uniform across the whole sample. After being annealed for 1 h at 350 °C in a vacuum, the PL intensity was enhanced by 6-fold (Figure 28b). At the same time, the PL peak blue-shifted after the annealing. Figures 28c-d show another MoS₂ mono-layer before and after annealing at 500 °C for 1 h in a vacuum. The PL image becomes highly inhomogeneous after the annealing. More detailed investigation indicated that the PL enhancement and inhomogeneity

should come from the reaction of oxygen (due to not very high vacuum condition) with MoS₂ at high temperature and followed chemical bonding of oxygen molecules to MoS₂.

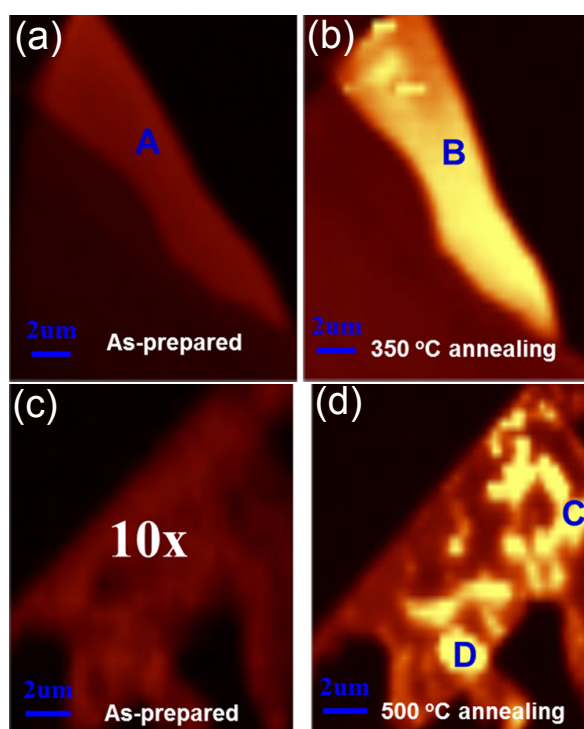


Figure 28. PL intensity images of as-prepared (a,c) and annealed MoS₂ mono-layers in a vacuum for 1 h at (b) 350 °C and (d) 500 °C [125]. Reprinted with permission from Reference [125]. Copyright © 2014 American Chemical Society.

Yamamoto et al. [161] mechanically exfoliated MoS₂ single-layers and few-layers from MoS₂ bulk crystals, deposited them onto 300 nm thick SiO₂/Si substrates. The MoS₂ layers were then exposed to an Ar/O₂ mixture at temperatures ranging from 27 °C to 400 °C. The flow rates of Ar and O₂ were 1.0 L/min and 0.7 L/min, respectively. Raman spectroscopy measurements indicated that the oxygen treatments led to triangular etch pits on the surfaces of the atomically thin MoS₂. MoS₂ was etched preferentially along the crystallographic directions of the zigzag edges with a preferential termination, resulting in uniform orientations of the pits, as shown in Figure 29a–e. The pit size increased with increasing oxidation exposure (Figure 29f), and the growth rate was larger at higher temperature. However, the numbers of etch pits per unit area was uncorrelated with oxidation time, oxidation temperature, and MoS₂ thickness but varied significantly from sample to sample. It was assumed that the oxidative etching in MoS₂ layers on SiO₂ was initiated at intrinsic defect sites. Additionally, oxygen exposure above 200 °C significantly diminished the electron density in MoS₂ single-layers and oxygen treatments at 400 °C resulted in conversion of MoS₂ layers to MoO₃ platelets. No molybdenum oxide (MoO₃) was detected after oxygen treatments below 340 °C.

Tongay et al. [162] annealed MoS₂ single-layers in a vacuum. Figure 30 shows room temperature PL spectra of a MoS₂ mono-layer annealed at 450 °C in a vacuum for different annealing time. A 40 min annealing at 450 °C enhanced the PL intensity by over 50 times. The FWHM of the PL peak decreased and the PL peak position shifted slightly with annealing time. The thermal annealing did not degrade the crystalline quality of the material.

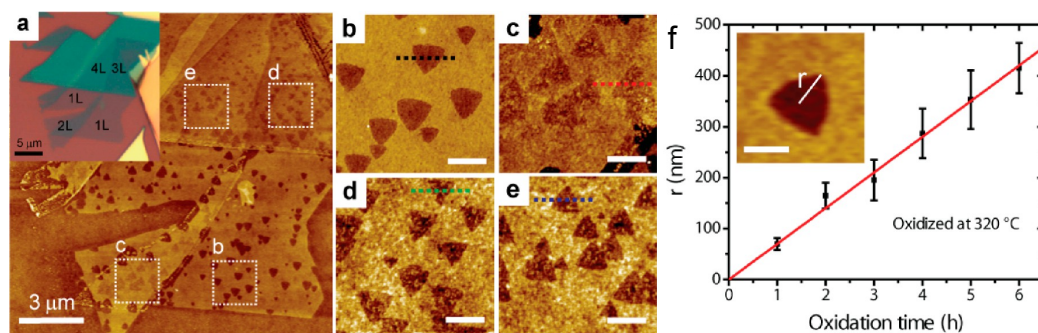


Figure 29. (a) AFM images of MoS₂ single-layer (1L), bi-layer (2L), tri-layer (3L), and four-layer (4L) on SiO₂ after oxidation at 320 °C for 3 h [161]. The inset shows an optical image of this flake before oxidation. (b–e) Close-up images of the areas surrounded by dashed lines on (b) 1L, (c) 2L, (d) 3L, and (e) 4L in the panel (a) [161]. The scale bars are 500 nm. (f) The average distance r from the center to the apex of triangular pits as a function of oxidation time [161]. The inset is an AFM image of a typical triangular pit formed on single-layer MoS₂ after oxidation for 4 h. The scale bar is 300 nm. Reprinted with permission from Reference [161]. Copyright © 2013 American Chemical Society.

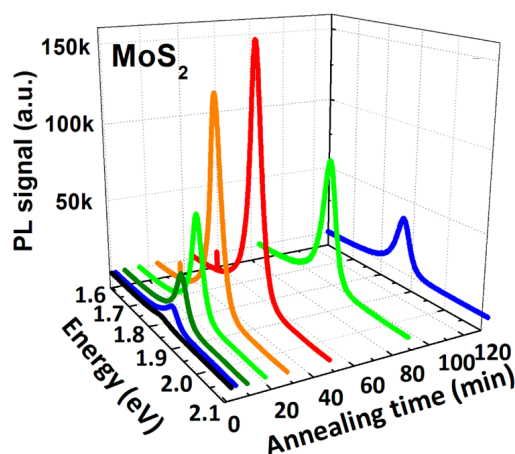


Figure 30. PL spectra of mono-layer MoS₂ for different annealing time [162]. The anneal temperature is 450 °C in a vacuum. Reprinted with permission from Reference [162]. Copyright © 2013 American Chemical Society.

4.3. Hybrid Irradiation: UV–Ozone Treatments

Ultraviolet–ozone cleaning technique is a dry-cleaning method to clean material surfaces by the decomposition of contaminants through ultraviolet irradiation and the chemical action of oxidation by ozone. During cleaning, surface organic compounds decompose to volatile substances by ultraviolet lights and by strong oxidation of ozone. The technique has been employed to irradiate 2D MoS₂ mono-layers [163,164] and few-layers [109,165–167].

Wang et al. [164] rapidly treated MoS₂ 1–3 layers that were mechanically exfoliated from crystals. There was no any change before and after the UV–ozone treatments. It was assumed that the irradiation effect was below detection because of the rapid treatment (30 s) and nitrogen protection that reduced high oxidation and mobility change. Le et al. [165] prepared MoS₂ nanosheets using a sonication exfoliation method and UV–ozone treated the MoS₂ multi-layers for 15–30 min. The MoS₂ layers were converted to MoO_x. Burman et al. [167] treated liquid-exfoliated MoS₂ few-layers (15–16 layers) in UV–ozone atmosphere for 1.5 h. It was found that the Mo/S atomic ratio decreased, and atomic percentage of oxygen increased with the expose time. Azcatl et al. [109] exposed the mechanically exfoliated MoS₂ layers under ultraviolet–ozone at room temperature. They found that oxygen–sulfur bonds were formed at the top sulfur layer while the sulfur–molybdenum bonds were kept besides removal of adsorbed carbon contamination from the MoS₂ surface.

The ultraviolet–ozone technique was also used to mill MoS₂ few-layers to mono-layers [166]. Compared to mechanically exfoliated MoS₂ single-layers, the PL intensity of the UV–ozone milled MoS₂ mono-layers was enhanced by 20–30 times.

5. Irradiation Mechanism and Theoretical Simulations

Besides the experimental work reviewed in the previous sections, there are lots of theoretical approaches to investigate the irradiation mechanism of MoS₂ 2D nanosheets.

Komsa et al. [78] calculated the displacement threshold energy and the minimum initial kinetic energy of the recoil atom to kick an atom from MoS₂ mono-layers, using the density-functional theory with the Perdew-Burke-Ernzerhof exchange-correlation function. The sulfur displacement threshold energy of MoS₂ was 6.9 eV, corresponding to incident-electron energies of about 90 keV. About 20 eV was required to displace one molybdenum atom from its site in MoS₂ mono-layer lattices, corresponding to an electron energy of 560 keV. Therefore, the sulfur sub-layers were easier destroyed while it was unlikely to generate molybdenum vacancies in molybdenum sub-layers under TEM observations (where 200 keV electron beams were employed). Figure 31 shows the calculated cross-section of sulfur atoms. Lattice vibrations were taken into account, assuming a Maxwell-Boltzmann velocity distribution. The cross denotes the experimentally determined cross-section for MoS₂. The inset shows the same data for a larger range of electron energies. The atom displacement cross-section was estimated from the electron threshold energy by using the McKinley-Feshbach formalism.

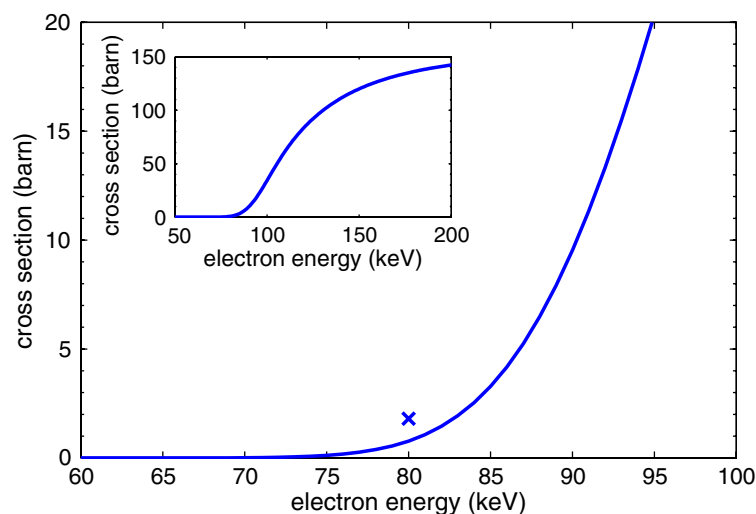


Figure 31. Cross-section for sputtering a sulfur atom from MoS₂ mono-layers as calculated through the McKinley-Feshbach formalism and the dynamical values of the displacement thresholds [78]. Reprinted with permission from Reference [78]. Copyright © 2012 by the American Physical Society.

The calculated displacement threshold energy was in agreement with experimental observations. Single sulfur vacancies (VS's) were frequently observed under transmission electron microscopes with an 200 kV acceleration voltage (the electron energy, 200 keV is higher than the displacement energy of sulfur atoms (90 keV) while lower than that of molybdenum atoms, 560 keV).

Table 2 compares formation thresholds of five kinds of defect configurations for MoS₂ bulks and mono-layers. The thresholds for single S vacancies were very low, both in bulk and mono-layers. Single-line S-vacancy and double-line S-vacancy configurations are generated with increasing single S-vacancy concentration by prolonged electron irradiation. In addition, the formation thresholds for Mo-vacancy and DIV are not very high (18–29 eV).

Table 2. Comparison of formation thresholds in eV for various vacancy configurations of MoS₂ bulks and mono-layers [77].

Configuration	Bulk (eV)	Mono-layer (eV)
single S-vacancy	14.4	5.7
single Mo-vacancy	24.8	18.8
single-line S-vacancy	39.2	30.5
double-line S-vacancy	66.2	62.3
DIV	28.8	23.3

DIV: di-vacancy comprised of nearest neighbor single sulfur vacancies and single molybdenum vacancies.

Kretschmer et al. [168] combined analytical potential molecular dynamics with Monte Carlo simulations to simulate helium and neon ion irradiation of MoS₂ nanosheets deposited on SiO₂ substrates. Their simulation indicated that substrates governed the defect production of irradiated MoS₂ layers. The irradiation-induced defect production was dominated by backscattered ions and sputtered substrate atoms, rather than by the direct helium and neon ion impacts.

Molecular dynamics simulations were also employed to study the production of defects in MoS₂ mono-layers under noble gas ion irradiation, such as He, Ne, Ar, Kr and Xe [169]. Sulfur atoms were sputtered away predominantly from the top or bottom layers by the ion irradiation, depending on the incident angle, ion type, and ion energy.

6. Irradiation-Induced Properties

Pure 2H-MoS₂ crystalline bulks are indirect band-gap semiconductors and show diamagnetic from 10 K to room temperature. Their physical properties are sensitive to structures and defects. Irradiation produces defects in MoS₂ few-layers and affects their properties significantly. Below, the optical properties, electronic properties, catalytic properties, and magnetic properties are summarized.

6.1. Band Structures

Bulk MoS₂ is a semiconductor with an indirect band gap of 1.23 eV [36,170]. The band gap of the material depends on thickness [171], as shown in Figure 2. Figure 32a shows the band structure of MoS₂ mono-layers without vacancies. MoS₂ mono-layers have a direct band gap of 1.8 eV, resulting in strong absorption, PL bands [38,39], and electroluminescence [172] near 680 nm.

Defects affect the band gap of MoS₂ layers significantly. Figure 32b–c shows calculated band structures of MoS₂ mono-layers with defects. Negative (S vacancies) and positive (Mo vacancies) charges transferred to the orbitals of nearest neighbor Mo or S atoms around the vacancies, resulting in additional states at the bonding level and at mid-gap of the band structures. The *K*-point direct band gap remained intact for MoS₂ mono-layers with S vacancies, while the gap value was reduced. The direct band gap at *K*-point was reduced too for MoS₂ mono-layers with Mo vacancies.

6.2. Electric Properties

The density-functional method and the Green's function approach indicated that structural defects and grain boundaries were principal contributors to electric transport properties of MoS₂ mono-layers [173]. Atomic vacancies could significantly reduce the conductance of the 2D layers. In experiments, MoS₂ 2D materials were deposited on various substrates and connected to metal electrodes to fabricate FETs to detect electric properties under irradiation.

Durand et al. [174] studied electrical transport properties of CVD-grown MoS₂ mono-layers on SiO₂/Si substrates. The carrier density was significantly increased, and the mobility was reduced under a low-energy electron irradiation (5.0 keV) in an UHV environment. It was believed that the electron-irradiation generated defects in MoS₂ layers and caused Coulomb potentials at the MoS₂/SiO₂ interfaces.

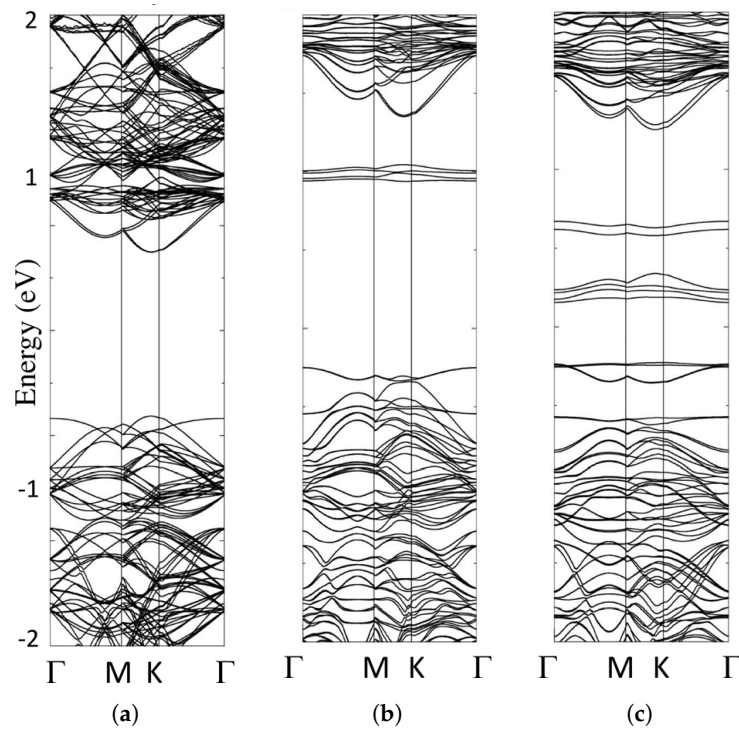


Figure 32. Total band structure for different vacancy configurations in MoS₂ mono-layers (a) without vacancy, (b) with single sulfur vacancies, and (c) single molybdenum vacancies along Γ -M-K- Γ high-symmetry directions of hexagonal Brillouin zone [77].

Lu et al. [175] grew MoS₂ single-crystalline few-layers on SiO₂/Si substrates at 700 °C through CVD method, and then transferred them to pre-patterned SiO₂/Si substrates with Au electrodes by the poly(methyl methacrylate)-assisted method. The fabricated MoS₂ devices were then electron-irradiated in a scanning electron microscope with a 30 keV electron beam. The electron dose was 100–1800 $\mu\text{C}/\text{cm}^2$. It was found that the threshold voltage shifted to the negative side and the mobility increased upon the increasing electron doses.

Parkin et al. [79] deposited single-crystalline MoS₂ mono-layers onto SiN_x membranes, contacted them to Au electrodes. The fabricated device was then irradiated under a TEM electron beam with 200 keV. It was found that the electrical resistance increased with the electron irradiation dose.

Kim et al. [86] prepared few-layer MoS₂ FETs, and investigated the effect of irradiation under 10 MeV proton exposures. The electrical properties of the devices were nearly unchanged in response to low fluence proton irradiation (10^{12} protons/cm²). The current and conductance of the devices significantly decreased after high fluence irradiation (10^{13} – 10^{14} protons/cm²). The electrical changes contributed to proton-irradiation-induced traps in the SiO₂ substrate layers and at the interfaces between the MoS₂ layers and the SiO₂ layers.

Islam et al. [128] measured electrical properties of MoS₂ mono-layers exposed under oxygen plasma. The plasma was generated from a gas mixture of oxygen (20%) and argon (80%) under a pressure of 250–350 mTorr at 50 kHz. Figure 33a shows the I_D - V_{DS} curves of the device at a back-gate voltage $V_G = 40$ V for various plasma exposure time. The I_D - V_{DS} curves were linear around the zero bias, showing Ohmic behaviors. Figure 33b demonstrates the exposure-time dependence of electric resistance. The resistance increased exponentially with increasing plasma exposure time. The drain current and mobility decreased exponentially with plasma exposure time, dropping more than four orders of magnitude after only a total of 6 s plasma exposure. It was claimed that the significant degradation of electronic properties was caused by the creation of insulating MoO₃-rich disordered domains in the MoS₂ sheet upon oxygen plasma exposure.

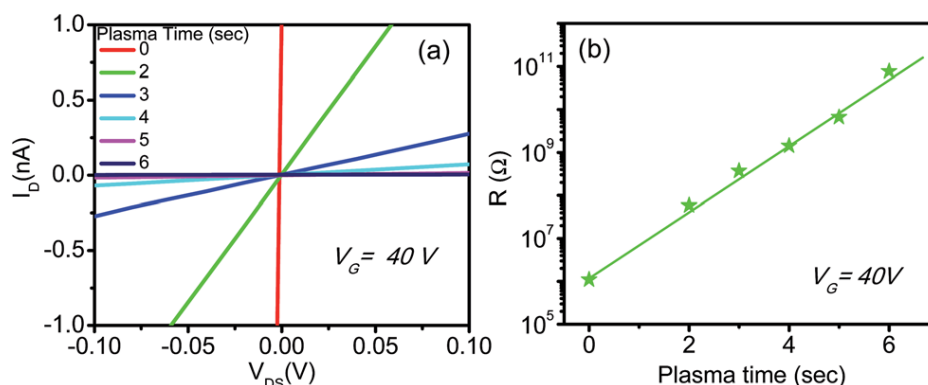


Figure 33. (a) I_D - V_{DS} curves of the single-layer MoS_2 device after different plasma exposure time [128]. (b) Resistance of the device as a function of plasma exposure time [128]. Republished with permission of RSC Publisher, from Reference [128]. © 2014. Permission conveyed through Copyright Clearance Center, Inc.

6.3. Catalytic Properties

Molybdenum is relatively abundant and cheaper than noble metals. Thus, molybdenum compounds have been used as electrocatalysts and photoelectrocatalysts to supersede noble metal catalysts. It was found that MoS_2 edges were catalytically active for hydrogen evolution reaction (HER) while the basal surfaces were catalytically inert. So MoS_2 nanomaterials have been employed as catalysts to generate hydrogen [69,176–179] because of more catalytic edges. MoS_2 nanoparticles were first used as photocatalysts [180] and electrocatalysts [181] to generate hydrogen in the 2000s. The catalytic properties were controlled by edge sites of the MoS_2 materials. MoS_2 2D films were more active and employed as photocatalysts [182] late in 2016 for water purification,

Irradiation can introduce defects in MoS_2 layers, which create more HER active sites. Sulfur vacancies can activate and optimize hydrogen evolution [20]. Additionally, electrical conductivity can be tuned by the introduced defects. Therefore, catalytic activities of MoS_2 HER can be significantly enhanced by irradiation defect engineering. Tao et al. [183] treated the CVD-grown MoS_2 thin films by Ar plasma. The active site density of MoS_2 thin films increased five times to $7.74 \times 10^{16} \text{ cm}^{-2}$ after the Ar plasma treatments. HER performance was enhanced significantly too. However, long-time Ar treatments etched MoS_2 , not benefited the HER behaviors. The MoS_2 sheets were also treated by O_2 plasma [183]. The O_2 plasma treatments led to the formation of both Mo-O and S-O bonds, generating more active sites with the increasing plasma time, enhancing the HER activity significantly.

6.4. Magnetic Properties

2H- MoS_2 bulks are temperature-dependent diamagnetic [184]. It was reported that irradiation improved magnetic ordering in single crystals of MoS_2 [85]. Karmakar et al. [77] investigated electron-irradiation-induced magnetic behaviors of MoS_2 crystals. The irradiation was carried out under 30 keV electrons with exposure time of 30 min. The effective magnetic moment of single crystals increased from $0.42 \mu_B$ per Mo-ion to $1.11 \mu_B$ per Mo-ion on account of irradiation.

Han et al. [74] investigated magnetism of electron-irradiated MoS_2 single crystals. The diamagnetic MoS_2 single crystals transformed into ferromagnetic state after irradiation up to room temperature, as shown in Figure 34. The irradiation-induced magnetic phase transition was largely attributed to the strain around the irradiation-induced vacancies.

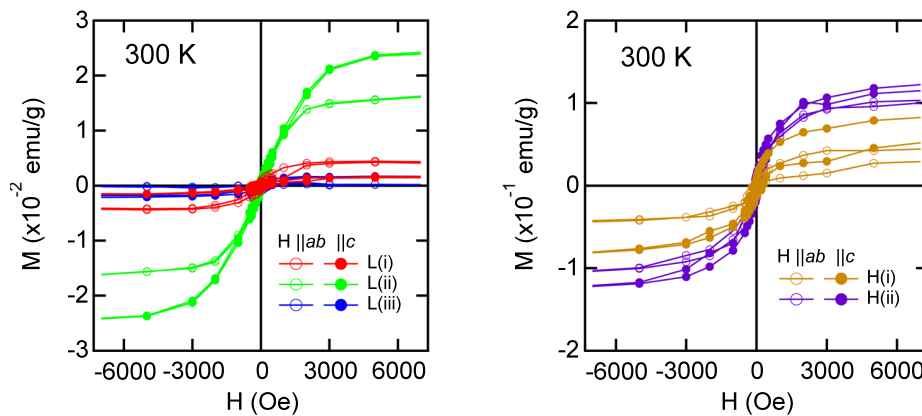


Figure 34. Magnetization curves of crystalline MoS₂ lamellae with a thickness of 100 microns after various electron irradiation [74]. Left panel: under low-energy electron irradiation. L(i): 150 kGy and 0.7 MeV; L(ii): 300 kGy and 0.7 MeV; L(iii): 600 kGy and 0.7 MeV. Right panel: under high-energy electron irradiation. H(i): 100 kGy and 2.0 MeV; H(ii): 250 kGy and 2.0 MeV. Magnetic fields were parallel to *ab*-plane or *c*-plane of the lamellae. Reprinted from Reference [74], with the permission of AIP Publishing.

Mathew et al. [85] irradiated MoS₂ sheets with a thickness of 200 μm at room temperature using a 3.5 MeV proton ion beam. The pristine sample was diamagnetic in nature. After irradiated at a fluence of 1×10^{18} ions/cm², ferromagnetic ordering was induced in the MoS₂, as shown in Figure 35a. More detailed work indicated that the induced magnetization depended on the irradiation dose. Figure 35b shows the magnetization of irradiated MoS₂ crystalline flakes that were measured at 300 K and 5 kOe as a function of proton ion fluence from 1×10^{17} ions/cm² to 5×10^{18} ions/cm². The magnetization of the pristine flakes was negative as well as in irradiated flakes at a fluence of 1×10^{17} ions/cm². The magnetization became positive after the sample was irradiated at a fluence of 2×10^{18} ions/cm² and increased with the irradiation doses. However, the magnetization decreased when the flakes were irradiated at a fluence of 5×10^{18} ions/cm².

Mathew et al. [85] also exposed MoS₂ crystals (200 μm thickness) under 0.5 MeV proton irradiation at an ion fluence of 1×10^{18} ions/cm² (same fluence at which magnetic ordering was observed using 2 MeV protons) while ferromagnetism was not observed in the low-energy proton irradiation. After annealing at 350 °C for 1 h in Ar flow, a weak magnetic hysteresis loop was observed. The weak magnetic signal was also observed in the irradiated samples at a lower fluence of 2×10^{17} ions/cm² and a lower energy of 0.5 MeV proton irradiation. Based on these phenomena, the appearance of observed magnetism in proton-irradiated MoS₂ flakes were due to a combination of defect moments arising from vacancies, interstitials, deformation and partial destruction of the lattice structure, such as the formation of edge states and reconstructions of the lattice.

Zhang et al. [185] reported weak ferromagnetism phenomenon in MoS₂ nanosheets and attributed the magnetic properties to the presence of unsaturated edge atoms. Later, first-principles computations and density-functional theory calculations were carried out to predict ferromagnetism in zigzag nanoribbons of MoS₂ [186–188], magnetism in MoS₂ clusters [189], and magnetic edge state of hydrodesulfurized MoS₂ particles [190]. It was generally accepted that [191] zigzag MoS₂ edges were ferromagnetic and metallic whereas armchair MoS₂ edges were nonmagnetic and semiconducting. The predication was experimentally approved in MoS₂ few-layers [192]. It stated that grain boundaries or defects in the nanosheets were responsible for the ferromagnetism of MoS₂ nanosheets.

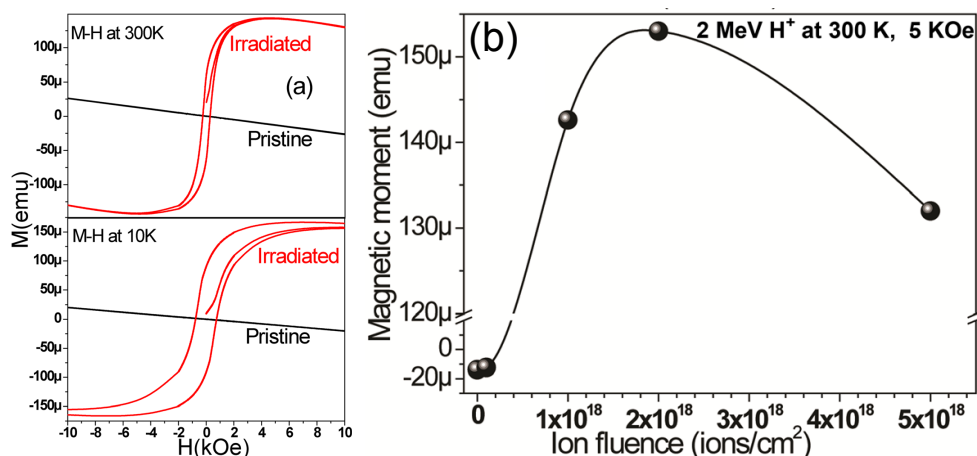


Figure 35. (a) M vs H curve for a pristine without irradiation and an irradiated MoS₂ micron-thick flake at a fluence of 5×10^{18} protons/cm² and (b) magnetization as a function of proton fluence from 1×10^{17} protons/cm² to 5×10^{18} protons/cm² [85]. Reprinted from Reference [85], with the permission of AIP Publishing.

Recent work stated that zigzag edges of MoS₂ few-layers can induce ferromagnetism. Therefore, defects, such as sulfur vacancies, can convert diamagnetic 2H-MoS₂ nanosheets ferromagnetism [193]. Irradiation could create numerous defects in MoS₂ 2D materials as discussed in the previous sections. So irradiation should affect magnetic properties of MoS₂ few-layers significantly. More fruitful outputs are expected in irradiated MoS₂ few-layers.

7. Conclusions and Outlook

Semiconducting MoS₂ 2D layers have unique transport properties and have been applied in various devices. Their band-gap, doping, photonic, electric, electronic, magnetic, chemical, and bio-properties can be tuned effectively and simply by defect engineering. Various irradiation exposures, including swift-heavy ions, argon ions, alpha particles, protons, electrons, electromagnetic waves, can significantly induce defects in MoS₂ few-layers to manipulate various properties essentially. Various defects, mainly sulfur vacancies and molybdenum vacancies, have been generated/created in MoS₂ layers. MoS₂ layers can be significantly activated, functionalized, and modified. The irradiation-induced defects are beneficial for several applications including: solar cells [19,194–196], batteries [54,197,198], supercapacitors [199], thin film transistors [15,16,80,86,110,138,200–205], sensors [17,55,56,106,206–210], hydrogen generators [8,47,50,69,134,176,177,183,211,212], and applications in thermoelectrics [213–216], piezotronics [63], valleytronics [65], and environments [45,49]. MoS₂ 2D layers were damaged simultaneously under the irradiation and lost their unique properties. Therefore, it is critical to control the irradiation exposure to tune MoS₂ properties by the irradiation-induced defect engineering while avoid potential damages.

Besides MoS₂ 2D layers, the irradiation techniques can be employed to tune physical properties of other disulfide 2D materials, such as NiS₂ urea-electrocatalysts [217], WS₂ hybrid catalysts [218], as well as selenide water-electrocatalysts [219], perovskite electrocatalytic nanoparticles [220], C₃N₄ catalytic materials [221], hydroxide nanosheet battery-electrodes [222], oxide photocatalysts [223], low-dimensional thermoelectric materials [224,225], graphene and carbon nanotubes [226–228], and even porous electrodes [229,230].

Author Contributions: G.Z. and Y.L. conceived the idea, designed and went through with the manuscript. H.D. wrote the section of alpha-particle irradiation. N.T. and Y.L. wrote the section of UV irradiation. M.G. and Y.L. wrote the section of proton irradiation. A.L. was in charge of the section of magnetic properties. Q.P. took charge of the theoretical analysis on irradiation. C.W. summarized background of MoS₂ materials. J.-A.Y. was in charge of Raman scattering. G..Z. and Y.L. wrote other sections. All authors provided constructive comments on the manuscript.

Funding: Y.L. is partially supported by the Army Research Laboratory under Cooperative Agreement Number W911NF-12-2-0022. A.L. is thankful to the financial support from the National Science Foundation through research grant NSF DMR 1206380. C.W. thanks the financial support from the National Natural Science Foundation of China (grants 51502099), the National Key Research and Development Program of China (Grant No. 2017YFE0120500), and the Hubei “Chu-Tian Young Scholar” program.

Acknowledgments: The views and conclusions contained in this document are those of the authors and should not be interpreted as representing the official policies, either expressed or implied, of the Army Research Laboratory or the U. S. Government. The U. S. Government is authorized to reproduce and distribute reprints for Government purposes notwithstanding any copyright notation herein.

Conflicts of Interest: The authors declare no conflict of interest.

Abbreviations

The following abbreviations are used in this document:

2D	two-dimensional
AFM	atomic force microscopy
CBM	conduction band minimum
CVD	chemical vapor deposition
EBI	electron-beam irradiation
EBIT	electron-beam ion trap
EBL	electron-beam lithography
EDS	electron X-ray dispersive spectroscopy
EDX	energy-dispersive X-ray spectroscopy
EPMA	electron probe micro-analyzer
FET	field effect transistor
FFT	fast Fourier transformation
FIB	focused ion beam
FWHM	full width at half maximum
GANIL	The Grand Accélérateur National d’Ions Lourds (Large Heavy Ion National Accelerator)
HAADF	high angle annular dark-field
HER	hydrogen evolution reaction
HIM	helium-ion microscopy
HIRFL	heavy ion Research facility in Lanzhou
HRTEM	high-resolution transmission electron microscopy
IBAD	ion-beam assisted deposition
LEAF	low-energy accelerator facility
MBE	molecular beam epitaxy
NEMS	nanoelectromechanical systems
PAMBE	plasma-assisted molecular beam epitaxy
PL	photoluminescence
RF	radio-frequency
RT	room temperature
SAED	selected-area electron diffraction
SEM	scanning electron microscopy
STEM	scanning transmission electron microscopy
STM	scanning tunneling microscope
TMDC	Transition-metal dichalcogenides
TEM	transmission electron microscopy
TOF-SIMS	time-of-flight secondary ion mass spectrometry
UV	ultraviolet
UHV	ultra-high vacuum
VBM	valence band maximum
VUV	vacuum ultraviolet
XPS	X-ray photoelectron spectroscopy
XRD	X-ray diffraction

References

1. Kroto, H.W.; Heath, J.R.; O'Brien, S.C.; Curl, R.F.; Smalley, R.E. C₆₀: Buckminsterfullerene. *Nature* **1985**, *318*, 162–163. [\[CrossRef\]](#)
2. Iijima, S.; Ichihashi, T. Single-shell carbon nanotubes of 1-nm diameter. *Nature* **1993**, *363*, 603–605. [\[CrossRef\]](#)
3. Bethune, D.S.; Kiang, C.H.; de Vries, M.S.; Gorman, G.; Savoy, R.; Vazquez, J.; Beyers, R. Cobalt-catalysed growth of carbon nanotubes with single-atomic-layer walls. *Nature* **1993**, *363*, 605–607. [\[CrossRef\]](#)
4. Novoselov, K.S.; Geim, A.K.; Morozov, S.V.; Jiang, D.; Zhang, Y.; Dubonos, S.V.; Grigorieva, I.V.; Firsov, A.A. Electric field effect in atomically thin carbon films. *Science* **2004**, *306*, 666–669. [\[CrossRef\]](#)
5. Frindt, R.F. Single crystals of MoS₂ several molecular layers thick. *J. Appl. Phys.* **1966**, *37*, 1928–1929. [\[CrossRef\]](#)
6. Spalvins, T. Lubrication with sputtered MoS₂ films: Principles, operation, and limitations. *J. Mater. Eng. Perform.* **1992**, *1*, 347–351. [\[CrossRef\]](#)
7. Chhowalla, M.; Amaratunga, G.A.J. Thin films of fullerene-like MoS₂ nanoparticles with ultra-low friction and wear. *Nature* **2000**, *407*, 164–167. [\[CrossRef\]](#) [\[PubMed\]](#)
8. Jaramillo, T.F.; Jørgensen, K.P.; Bonde, J.; Nielsen, J.H.; Horch, S.; Chorkendorff, I. Identification of active edge sites for electrochemical H₂ evolution from MoS₂ nanocatalysts. *Science* **2007**, *317*, 100–102. [\[CrossRef\]](#)
9. Roxlo, C.B.; Deckman, H.W.; Gland, J.; Cameron, S.D.; Chianelli, R.R. Edge surfaces in lithographically textured molybdenum disulfide. *Science* **1987**, *235*, 1629–1631. [\[CrossRef\]](#)
10. Chianelli, R.R.; Siadati, M.H.; De la Rosa, M.P.; Berhault, G.; Wilcoxon, J.P.; Bearden, R.; Abrams, B.L. Catalytic properties of single layers of transition metal sulfide catalytic materials. *Catal. Rev.* **2006**, *48*, 1–41. [\[CrossRef\]](#)
11. Wang, Q.H.; Kalantar-Zadeh, K.; Kis, A.; Coleman, J.N.; Strano, M.S. Electronics and optoelectronics of two-dimensional transition metal dichalcogenides. *Nat. Nanotechnol.* **2012**, *7*, 699–712. [\[CrossRef\]](#) [\[PubMed\]](#)
12. Peng, Q.; De, S. Outstanding mechanical properties of monolayer MoS₂ and its application in elastic energy storage. *Phys. Chem. Chem. Phys.* **2013**, *15*, 19427–19437. [\[CrossRef\]](#) [\[PubMed\]](#)
13. Fiori, G.; Bonaccorso, F.; Iannaccone, G.; Palacios, T.; Neumaier, D.; Seabaugh, A.; Banerjee, S.K.; Colombo, L. Electronics based on two-dimensional materials. *Nat. Nanotechnol.* **2014**, *9*, 768–779. [\[CrossRef\]](#) [\[PubMed\]](#)
14. Lembke, D.; Bertolazzi, S.; Kis, A. Single-layer MoS₂ electronics. *Acc. Chem. Res.* **2015**, *48*, 100–110. [\[CrossRef\]](#) [\[PubMed\]](#)
15. Radisavljevic, B.; Radenovic, A.; Brivio, J.; Giacometti, V.; Kis, A. Single-layer MoS₂ transistors. *Nat. Nanotechnol.* **2011**, *6*, 147–150. [\[CrossRef\]](#) [\[PubMed\]](#)
16. Sarkar, D.; Liu, W.; Xie, X.; Anselmo, A.C.; Mitragotri, S.; Banerjee, K. MoS₂ field-effect transistor for next-generation label-free biosensors. *ACS Nano* **2014**, *8*, 3992–4003. [\[CrossRef\]](#) [\[PubMed\]](#)
17. Kim, J.S.; Yoo, H.W.; Choi, H.O.; Jung, H.T. Tunable volatile organic compounds sensor by using thiolated ligand conjugation on MoS₂. *Nano Lett.* **2014**, *14*, 5941–5947. [\[CrossRef\]](#)
18. Yazyev, O.V.; Kis, A. MoS₂ and semiconductors in the flatland. *Mater. Today* **2015**, *18*, 20–30. [\[CrossRef\]](#)
19. Nguyen, T.P.; Van Le, Q.; Choi, K.S.; Oh, J.H.; Kim, Y.G.; Lee, S.M.; Chang, S.T.; Cho, Y.H.; Choi, S.; Kim, T.Y.; et al. MoS₂ nanosheets exfoliated by sonication and their application in organic photovoltaic cells. *Sci. Adv. Mater.* **2015**, *7*, 700–705. [\[CrossRef\]](#)
20. Li, H.; Tsai, C.; Koh, A.L.; Cai, L.; Contryman, A.W.; Fragapane, A.H.; Zhao, J.; Han, H.S.; Manoharan, H.C.; Abild-Pedersen, F.; et al. Activating and optimizing MoS₂ basal planes for hydrogen evolution through the formation of strained sulphur vacancies. *Nat. Mater.* **2016**, *15*, 48–53. [\[CrossRef\]](#)
21. Yu, Z.; Pan, Y.; Shen, Y.; Wang, Z.; Ong, Z.Y.; Xu, T.; Xin, R.; Pan, L.; Wang, B.; Sun, L.; et al. Towards intrinsic charge transport in monolayer molybdenum disulfide by defect and interface engineering. *Nat. Commun.* **2014**, *5*, 5290. [\[CrossRef\]](#) [\[PubMed\]](#)

22. Sim, D.M.; Kim, M.; Yim, S.; Choi, M.J.; Choi, J.; Yoo, S.; Jung, Y.S. Controlled doping of vacancy-containing few-layer MoS₂ via highly stable thiol-based molecular chemisorption. *ACS Nano* **2015**, *9*, 12115–12123.10.1021/acs.nano.5b05173. [[CrossRef](#)] [[PubMed](#)]
23. Nguyen, E.P.; Carey, B.J.; Ou, J.Z.; van Embden, J.; Gaspera, E.D.; Chrimes, A.F.; Spencer, M.J.S.; Zhuiykov, S.; Kalantar-zadeh, K.; Daeneke, T. Electronic tuning of 2D MoS₂ through surface functionalization. *Adv. Mater.* **2015**, *27*, 6225–6229.10.1002/adma.201503163. [[CrossRef](#)] [[PubMed](#)]
24. Cho, K.; Min, M.; Kim, T.Y.; Jeong, H.; Pak, J.; Kim, J.K.; Jang, J.; Yun, S.J.; Lee, Y.H.; Hong, W.K.; et al. Electrical and optical characterization of MoS₂ with sulfur vacancy passivation by treatment with alkanethiol molecules. *ACS Nano* **2015**, *9*, 8044–8053.10.1021/acs.nano.5b04400. [[CrossRef](#)] [[PubMed](#)]
25. Walker, R.C.; Shi, T.; Silva, E.C.; Jovanovic, I.; Robinson, J.A. Radiation effects on two-dimensional materials. *Phys. Status Solidi* **2016**, *213*, 3065–3077.10.1002/pssa.201600395. [[CrossRef](#)]
26. Peng, Q.; Crean, J.; Dearden, A.K.; Huang, C.; Wen, X.; Bordas, S.P.A.; De, S. Defect engineering of 2D monatomic-layer materials. *Mod. Phys. Lett. B* **2013**, *27*, 1330017.10.1142/S0217984913300172. [[CrossRef](#)]
27. Yang, D.; Sandoval, S.J.; Divigalpitiya, W.M.R.; Irwin, J.C.; Frindt, R.F. Structure of single-molecular-layer MoS₂. *Phys. Rev. B* **1991**, *43*, 12053–12056.10.1103/PhysRevB.43.12053. [[CrossRef](#)]
28. Wypych, F.; Schöllhorn, R. 1T-MoS₂, a new metallic modification of molybdenum disulfide. *J. Chem. Soc. Chem. Commun.* **1992**, *19*, 1386–1388.10.1039/C39920001386. [[CrossRef](#)]
29. Benavente, E.; Santa Ana, M.A.; Mendizábal, F.; González, G. Intercalation chemistry of molybdenum disulfide. *Coord. Chem. Rev.* **2002**, *224*, 87–109.10.1016/S0010-8545(01)00392-7. [[CrossRef](#)]
30. Fan, X.; Xu, P.; Zhou, D.; Sun, Y.; Li, Y.C.; Nguyen, M.A.T.; Terrones, M.; Mallouk, T.E. Fast and efficient preparation of exfoliated 2H MoS₂ nanosheets by sonication-assisted lithium intercalation and infrared laser-induced 1T to 2H phase reversion. *Nano Lett.* **2015**, *15*, 5956–5960.10.1021/acs.nanolett.5b02091. [[CrossRef](#)]
31. Xu, D.; Zhu, Y.; Liu, J.; Li, Y.; Peng, W.; Zhang, G.; Zhang, F.; Fan, X. Microwave-assisted 1T to 2H phase reversion of MoS₂ in solution: A fast route to processable dispersions of 2H-MoS₂ nanosheets and nanocomposites. *Nanotechnology* **2016**, *27*, 385604.10.1088/0957-4484/27/38/385604. [[CrossRef](#)] [[PubMed](#)]
32. Bromley, R.A.; Murray, R.B.; Yoffe, A.D. The band structures of some transition metal dichalcogenides. III. Group VIA: Trigonal prism materials. *J. Phys. C* **1972**, *5*, 759.10.1088/0022-3719/5/7/007. [[CrossRef](#)]
33. Wieting, T.J.; Verble, J.L. Infrared and Raman studies of long-wavelength optical phonons in hexagonal MoS₂. *Phys. Rev. B* **1971**, *3*, 4286–4292.10.1103/PhysRevB.3.4286. [[CrossRef](#)]
34. Mattheiss, L.F. Band structures of transition-metal-dichalcogenide layer compounds. *Phys. Rev. B* **1973**, *8*, 3719–3740.10.1103/PhysRevB.8.3719. [[CrossRef](#)]
35. Böker, T.; Severin, R.; Müller, A.; Janowitz, C.; Manzke, R.; Voß, D.; Krüger, P.; Mazur, A.; Pollmann, J. Band structure of MoS₂, MoSe₂, and α -MoTe₂: Angle-resolved photoelectron spectroscopy and ab initio calculations. *Phys. Rev. B* **2001**, *64*, 235305.10.1103/PhysRevB.64.235305. [[CrossRef](#)]
36. Kam, K.K.; Parkinson, B.A. Detailed photocurrent spectroscopy of the semiconducting group VIB transition metal dichalcogenides. *J. Phys. Chem.* **1982**, *86*, 463–467.10.1021/j100393a010. [[CrossRef](#)]
37. Yun, W.S.; Han, S.W.; Hong, S.C.; Kim, I.G.; Lee, J.D. Thickness and strain effects on electronic structures of transition metal dichalcogenides: 2H-MX₂ semiconductors (M = Mo, W; X = S, Se, Te). *Phys. Rev. B* **2012**, *85*, 033305.10.1103/PhysRevB.85.033305. [[CrossRef](#)]
38. Mak, K.F.; Lee, C.; Hone, J.; Shan, J.; Heinz, T.F. Atomically thin MoS₂: A new direct-gap semiconductor. *Phys. Rev. Lett.* **2010**, *105*, 136805.10.1103/PhysRevLett.105.136805. [[CrossRef](#)]
39. Splendiani, A.; Sun, L.; Zhang, Y.; Li, T.; Kim, J.; Chim, C.Y.; Galli, G.; Wang, F. Emerging photoluminescence in monolayer MoS₂. *Nano Lett.* **2010**, *10*, 1271–1275.10.1021/nl903868w. [[CrossRef](#)]
40. Yang, T.; Feng, J.; Liu, X.; Wang, Y.; Ge, H.; Cao, D.; Li, H.; Peng, Q.; Ramos, M.; Wen, X.D.; et al. A combined computational and experimental study of the adsorption of sulfur containing molecules on molybdenum disulfide nanoparticles. *J. Mater. Res.* **2018**, *33*, 3589–3603.10.1557/jmr.2018.309. [[CrossRef](#)]
41. Chhowalla, M.; Shin, H.S.; Eda, G.; Li, L.J.; Loh, K.P.; Zhang, H. The chemistry of two-dimensional layered transition metal dichalcogenide nanosheets. *Nat. Chem.* **2013**, *5*, 263–275.10.1038/nchem.1589. [[CrossRef](#)] [[PubMed](#)]
42. Ganatra, R.; Zhang, Q. Few-layer MoS₂: A promising layered semiconductor. *ACS Nano* **2014**, *8*, 4074–4099.10.1021/nn405938z. [[CrossRef](#)] [[PubMed](#)]
43. Jiang, J.W. Graphene versus MoS₂: A short review. *Front. Phys.* **2015**, *10*, 287–302. 015-0459-z. [[CrossRef](#)]

44. Wang, H.; Li, C.; Fang, P.; Zhang, Z.; Zhang, J.Z. Synthesis, properties, and optoelectronic applications of two-dimensional MoS₂ and MoS₂-based heterostructures. *Chem. Soc. Rev.* **2018**, *47*, 6101–6127.10.1039/C8CS00314A. [[CrossRef](#)] [[PubMed](#)]
45. Wang, Z.; Mi, B. Environmental applications of 2D molybdenum disulfide (MoS₂) nanosheets. *Environ. Sci. Technol.* **2017**, *51*, 8229–8244.10.1021/acs.est.7b01466. [[CrossRef](#)] [[PubMed](#)]
46. Zhang, X.; Lai, Z.; Tan, C.; Zhang, H. Solution-processed two-dimensional MoS₂ nanosheets: Preparation, hybridization, and applications. *Angew. Chem. Int. Ed.* **2016**, *55*, 8816–8838.10.1002/anie.201509933. [[CrossRef](#)] [[PubMed](#)]
47. Yang, L.; Liu, P.; Li, J.; Xiang, B. Two-dimensional material molybdenum disulfides as electrocatalysts for hydrogen evolution. *Catalysts* **2017**, *7*, 285.10.3390/catal7100285. [[CrossRef](#)]
48. Zhao, Y.; Zhang, Y.; Yang, Z.; Yan, Y.; Sun, K. Synthesis of MoS₂ and MoO₃ for their applications in H₂ generation and lithium ion batteries: A review. *Sci. Technol. Adv. Mater.* **2013**, *14*, 043501.10.1088/1468-6996/14/4/043501. [[CrossRef](#)]
49. Theerthagiri, J.; Senthil, R.A.; Senthilkumar, B.; Reddy Polu, A.; Madhavan, J.; Ashokkumar, M. Recent advances in MoS₂ nanostructured materials for energy and environmental applications—A review. *J. Solid State Chem.* **2017**, *252*, 43–71.10.1016/j.jssc.2017.04.041. [[CrossRef](#)]
50. Laursen, A.B.; Kegnæs, S.; Dahla, S.; Chorkendorff, I. Molybdenum sulfides—efficient and viable materials for electro- and photoelectrocatalytic hydrogen evolution. *Energy Environ. Sci.* **2012**, *5*, 5577–5591.10.1039/C2EE02618J. [[CrossRef](#)]
51. Ding, Q.; Song, B.; Xu, P.; Jin, S. Efficient electrocatalytic and photoelectrochemical hydrogen generation using MoS₂ and related compounds. *Chem* **2016**, *1*, 699–726.10.1016/j.chempr.2016.10.007. [[CrossRef](#)]
52. Li, Z.; Meng, X.; Zhang, Z. Recent development on MoS₂-based photocatalysis: A review. *J. Photochem. Photobiol. C* **2018**, *35*, 39–55.10.1016/j.jphotochemrev.2017.12.002. [[CrossRef](#)]
53. Han, B.; Hu, Y.H. MoS₂ as a co-catalyst for photocatalytic hydrogen production from water. *Energy Sci. Eng.* **2016**, *4*, 285–304.10.1002/ese3.128. [[CrossRef](#)]
54. Zhang, W.J.; Huang, K.J. A review of recent progress in molybdenum disulfide-based supercapacitors and batteries. *Inorg. Chem. Front.* **2017**, *4*, 1602–1620.10.1039/C7QI00515F. [[CrossRef](#)]
55. Huang, Y.; Guo, J.; Kang, Y.; Ai, Y.; Li, C.M. Two dimensional atomically thin MoS₂ nanosheets and their sensing applications. *Nanoscale* **2015**, *7*, 19358–19376.10.1039/C5NR06144J. [[CrossRef](#)]
56. Lopez-Sanchez, O.; Lembke, D.; Kayci, M.; Radenovic, A.; Kis, A. Ultrasensitive photodetectors based on monolayer MoS₂. *Nat. Nanotechnol.* **2013**, *8*, 497–501.10.1038/nnano.2013.100. [[CrossRef](#)] [[PubMed](#)]
57. Yin, Z.; Li, H.; Li, H.; Jiang, L.; Shi, Y.; Sun, Y.; Lu, G.; Zhang, Q.; Chen, X.; Zhang, H. Single-layer MoS₂ phototransistors. *ACS Nano* **2012**, *6*, 74–80.10.1021/nn2024557. [[CrossRef](#)]
58. Radisavljevic, B.; Whitwick, M.B.; Kis, A. Integrated circuits and logic operations based on single-layer MoS₂. *ACS Nano* **2011**, *5*, 9934–9938.10.1021/nn203715c. [[CrossRef](#)]
59. Liu, Y.; Liu, J. Hybrid nanomaterials of WS₂ or MoS₂ nanosheets with liposomes: Biointerfaces and multiplexed drug delivery. *Nanoscale* **2017**, *9*, 13187–13194.10.1039/C7NR04199C. [[CrossRef](#)]
60. Zhang, Z.; Xie, Y.; Peng, Q.; Chen, Y. Thermal transport in MoS₂/graphene hybrid nanosheets. *Nanotechnology* **2015**, *26*, 375402.10.1088/0957-4484/26/37/375402. [[CrossRef](#)]
61. Zhang, Z.; Xie, Y.; Peng, Q.; Chen, Y. A theoretical prediction of super high-performance thermoelectric materials based on MoS₂/WS₂ hybrid nanoribbons. *Sci. Rep.* **2016**, *6*, 21639.10.1038/srep21639. [[CrossRef](#)] [[PubMed](#)]
62. Wu, W.; Wang, L.; Li, Y.; Zhang, F.; Lin, L.; Niu, S.; Chenet, D.; Zhang, X.; Hao, Y.; Heinz, T.F.; et al. Piezoelectricity of single-atomic-layer MoS₂ for energy conversion and piezotronics. *Nature* **2014**, *514*, 470.10.1038/nature13792. [[CrossRef](#)] [[PubMed](#)]
63. Qi, J.; Lan, Y.W.; Stieg, A.Z.; Chen, J.H.; Zhong, Y.L.; Li, L.J.; Chen, C.D.; Zhang, Y.; Wang, K.L. Piezoelectric effect in chemical vapour deposition-grown atomic-monolayer triangular molybdenum disulfide piezotronics. *Nat. Commun.* **2015**, *6*, 7430.10.1038/ncomms8430. [[CrossRef](#)] [[PubMed](#)]
64. Feng, J.; Graf, M.; Liu, K.; Ovchinnikov, D.; Dumcenco, D.; Heiranian, M.; Nandigana, V.; Aluru, N.R.; Kis, A.; Radenovic, A. Single-layer MoS₂ nanopores as nanopower generators. *Nature* **2016**, *536*, 197–200.10.1038/nature18593. [[CrossRef](#)] [[PubMed](#)]

65. Cao, T.; Wang, G.; Han, W.; Ye, H.; Zhu, C.; Shi, J.; Niu, Q.; Tan, P.; Wang, E.; Liu, B.; et al. Valley-selective circular dichroism of monolayer molybdenum disulphide. *Nat. Commun.* **2012**, *3*, 887.10.1038/ncomms1882. [[CrossRef](#)]
66. Venkata Subbaiah, Y.P.; Saji, K.J.; Tiwari, A. Atomically thin MoS₂: A versatile nongraphene 2D material. *Adv. Funct. Mater.* **2016**, *26*, 2046–2069.10.1002/adfm.201504202. [[CrossRef](#)]
67. Dong, R.; Kuljanishvili, I. Review Article: Progress in fabrication of transition metal dichalcogenides heterostructure systems. *J. Vac. Sci. Technol. B* **2017**, *35*, 030803.10.1116/1.4982736. [[CrossRef](#)]
68. Sun, J.; Li, X.; Guo, W.; Zhao, M.; Fan, X.; Dong, Y.; Xu, C.; Deng, J.; Fu, Y. Synthesis methods of two-dimensional MoS₂: A brief review. *Crystals* **2017**, *7*, 198.10.3390/cryst7070198. [[CrossRef](#)]
69. Merki, D.; Hu, X. Recent developments of molybdenum and tungsten sulfides as hydrogen evolution catalysts. *Energy Environ. Sci.* **2011**, *4*, 3878–3888.10.1039/C1EE01970H. [[CrossRef](#)]
70. Novoselov, K.S.; Jiang, D.; Schedin, F.; Booth, T.J.; Khotkevich, V.V.; Morozov, S.V.; Geim, A.K. Two-dimensional atomic crystals. *Proc. Natl. Acad. Sci. USA* **2005**, *102*, 10451–10453.10.1073/pnas.0502848102. [[CrossRef](#)]
71. Coleman, J.N.; Lotya, M.; O'Neill, A.; Bergin, S.D.; King, P.J.; Khan, U.; Young, K.; Gaucher, A.; De, S.; Smith, R.J.; et al. Two-dimensional nanosheets produced by liquid exfoliation of layered materials. *Science* **2011**, *331*, 568–571.10.1126/science.1194975. [[CrossRef](#)]
72. Zhou, K.G.; Mao, N.N.; Wang, H.X.; Peng, Y.; Zhang, H.L. A mixed-solvent strategy for efficient exfoliation of inorganic graphene analogues. *Angew. Chem.* **2011**, *123*, 11031–11034.10.1002/ange.201105364. [[CrossRef](#)]
73. McDonnell, S.; Addou, R.; Buie, C.; Wallace, R.M.; Hinkle, C.L. Defect-dominated doping and contact resistance in MoS₂. *ACS Nano* **2014**, *8*, 2880–2888.10.1021/nn500044q. [[CrossRef](#)] [[PubMed](#)]
74. Han, S.W.; Park, Y.; Hwang, Y.H.; Lee, W.G.; Hong, S.C. Investigation of electron irradiation-induced magnetism in layered MoS₂ single crystals. *Appl. Phys. Lett.* **2016**, *109*, 252403.10.1063/1.4971192. [[CrossRef](#)]
75. Rotunno, E.; Fabbri, F.; Cinquanta, E.; Kaplan, D.; Longo, M.; Lazzarini, L.; Molle, A.; Swaminathan, V.; Salviati, G. Structural, optical and compositional stability of MoS₂ multi-layer flakes under high dose electron beam irradiation. *2D Mater.* **2016**, *3*, 025024.10.1088/2053-1583/3/2/025024. [[CrossRef](#)]
76. Lin, Y.C.; Dumcenco, D.O.; Huang, Y.S.; Suenaga, K. Atomic mechanism of the semiconducting-to-metallic phase transition in single-layered MoS₂. *Nat. Nanotechnol.* **2014**, *9*, 391–396.10.1038/nnano.2014.64. [[CrossRef](#)]
77. Karmakar, D.; Halder, R.; Padma, N.; Abraham, G.; Vaibhav, K.; Ghosh, M.; Kaur, M.; Bhattacharya, D.; Rao, T.V.C. Optimal electron irradiation as a tool for functionalization of MoS₂: Theoretical and experimental investigation. *J. Appl. Phys.* **2015**, *117*, 135701.10.1063/1.4916530. [[CrossRef](#)]
78. Komsa, H.P.; Kotakoski, J.; Kurasch, S.; Lehtinen, O.; Kaiser, U.; Krasheninnikov, A.V. Two-dimensional transition metal dichalcogenides under electron irradiation: Defect production and doping. *Phys. Rev. Lett.* **2012**, *109*, 035503.10.1103/PhysRevLett.109.035503. [[CrossRef](#)]
79. Parkin, W.M.; Balan, A.; Liang, L.; Das, P.M.; Lamparski, M.; Naylor, C.H.; Rodríguez-Manzo, J.A.; Johnson, A.T.C.; Meunier, V.; Drndić, M. Raman shifts in electron-irradiated monolayer MoS₂. *ACS Nano* **2016**, *10*, 4134–4142.10.1021/acsnano.5b07388. [[CrossRef](#)]
80. Matsunaga, M.; Higuchi, A.; He, G.; Yamada, T.; Krüger, P.; Ochiai, Y.; Gong, Y.; Vajtai, R.; Ajayan, P.M.; Bird, J.P.; et al. Nanoscale-barrier formation induced by low-dose electron-beam exposure in ultrathin MoS₂ transistors. *ACS Nano* **2016**, *10*, 9730–9737.10.1021/acsnano.6b05952. [[CrossRef](#)]
81. Liu, X.; Xu, T.; Wu, X.; Zhang, Z.; Yu, J.; Qiu, H.; Hong, J.H.; Jin, C.H.; Li, J.X.; Wang, X.R.; et al. Top-down fabrication of sub-nanometre semiconducting nanoribbons derived from molybdenum disulfide sheets. *Nat. Commun.* **2013**, *4*, 1776.10.1038/ncomms2803. [[CrossRef](#)] [[PubMed](#)]
82. Kim, B.H.; Gu, H.H.; Yoon, Y.J. Atomic rearrangement of a sputtered MoS₂ film from amorphous to a 2D layered structure by electron beam irradiation. *Sci. Rep.* **2017**, *7*, 3874.10.1038/s41598-017-04222-6. [[CrossRef](#)] [[PubMed](#)]
83. Ochedowski, O.; Marinov, K.; Wilbs, G.; Keller, G.; Scheuschner, N.; Severin, D.; Bender, M.; Maultzsch, J.; Tegude, F.J.; Schleberger, M. Radiation hardness of graphene and MoS₂ field effect devices against swift heavy ion irradiation. *J. Appl. Phys.* **2013**, *113*, 214306.10.1063/1.4808460. [[CrossRef](#)]
84. Bae, S.; Sugiyama, N.; Matsuo, T.; Raebiger, H.; Shudo, K.I.; Ohno, K. Defect-induced vibration modes of Ar⁺-irradiated MoS₂. *Phys. Rev. Appl.* **2017**, *7*, 024001.10.1103/PhysRevApplied.7.024001. [[CrossRef](#)]

85. Mathew, S.; Gopinadhan, K.; Chan, T.K.; Yu, X.J.; Zhan, D.; Cao, L.; Rusydi, A.; Breese, M.B.H.; Dhar, S.; Shen, Z.X.; et al. Magnetism in MoS₂ induced by proton irradiation. *Appl. Phys. Lett.* **2012**, *101*, 102103.10.1063/1.4750237. [[CrossRef](#)]
86. Kim, T.Y.; Cho, K.; Park, W.; Park, J.; Song, Y.; Hong, S.; Hong, W.K.; Lee, T. Irradiation effects of high-energy proton beams on MoS₂ field effect transistors. *ACS Nano* **2014**, *8*, 2774–2781.10.1021/nn4064924. [[CrossRef](#)] [[PubMed](#)]
87. Wang, B.; Yang, S.; Chen, J.; Mann, C.; Bushmaker, A.; Cronin, S.B. Radiation-induced direct bandgap transition in few-layer MoS₂. *Appl. Phys. Lett.* **2017**, *111*, 131101.10.1063/1.5005121. [[CrossRef](#)]
88. Isherwood, L.H.; Worsley, R.E.; Casiraghi, C.; Baidak, A. Alpha particle irradiation of bulk and exfoliated MoS₂ and WS₂ membranes. *Nucl. Instrum. Methods Phys. Res. Sect. B* **2018**, *435*, 180–189.10.1016/j.nimb.2018.01.018. [[CrossRef](#)]
89. Fox, D.S.; Zhou, Y.; Maguire, P.; O'Neill, A.; Ó'Coileáin, C.; Gatensby, R.; Glushenkov, A.M.; Tao, T.; Duesberg, G.S.; Shvets, I.V.; et al. Nanopatterning and electrical tuning of MoS₂ layers with a subnanometer helium ion beam. *Nano Lett.* **2015**, *15*, 5307–5313.10.1021/acs.nanolett.5b01673. [[CrossRef](#)]
90. Tongay, S.; Suh, J.; Ataca, C.; Fan, W.; Luce, A.; Kang, J.S.; Liu, J.; Ko, C.; Raghunathanan, R.; Zhou, J.; et al. Defects activated photoluminescence in two-dimensional semiconductors: Interplay between bound, charged, and free excitons. *Sci. Rep.* **2013**, *3*, 2657.10.1038/srep02657. [[CrossRef](#)]
91. Klein, J.; Kuc, A.; Nolinder, A.; Altzschner, M.; Wierzbowski, J.; Sigger, F.; Kreupl, F.; Finley, J.J.; Wurstbauer, U.; Holleitner, A.W.; et al. Robust valley polarization of helium ion modified atomically thin MoS₂. *2D Mater.* **2018**, *5*, 011007.10.1088/2053-1583/aa9642. [[CrossRef](#)]
92. Maguire, P.; Fox, D.S.; Zhou, Y.; Wang, Q.; O'Brien, M.; Jadwiszczak, J.; Cullen, C.P.; McManus, J.; Bateman, S.; McEvoy, N.; et al. Defect sizing, separation, and substrate effects in ion-irradiated monolayer two-dimensional materials. *Phys. Rev. B* **2018**, *98*, 134109.10.1103/PhysRevB.98.134109. [[CrossRef](#)]
93. Inoue, A.; Komori, T.; Shudo, K.I. Atomic-scale structures and electronic states of defects on Ar⁺-ion irradiated MoS₂. *J. Electron Spectrosc. Relat. Phenom.* **2013**, *189*, 11–18.10.1016/j.elspec.2012.12.005. [[CrossRef](#)]
94. Baker, M.A.; Gilmore, R.; Lenardi, C.; Gissler, W. XPS investigation of preferential sputtering of S from MoS₂ and determination of MoS_x stoichiometry from Mo and S peak positions. *Appl. Surf. Sci.* **1999**, *150*, 255–262.10.1016/S0169-4332(99)00253-6. [[CrossRef](#)]
95. Wahl, K.J.; Dunn, D.N.; Singer, I.L. Effects of ion implantation on microstructure, endurance and wear behavior of IBAD MoS₂. *Wear* **2000**, *237*, 1–11.10.1016/S0043-1648(99)00316-6. [[CrossRef](#)]
96. Ma, Q.; Odenthal, P.M.; Mann, J.; Le, D.; Wang, C.S.; Zhu, Y.; Chen, T.; Sun, D.; Yamaguchi, K.; Tran, T.; et al. Controlled argon beam-induced desulfurization of monolayer molybdenum disulfide. *J. Phys. Condens. Matter* **2013**, *25*, 252201.10.1088/0953-8984/25/25/252201. [[CrossRef](#)] [[PubMed](#)]
97. Zhu, J.; Wang, Z.; Yu, H.; Li, N.; Zhang, J.; Meng, J.; Liao, M.; Zhao, J.; Lu, X.; Du, L.; et al. Argon plasma induced phase transition in monolayer MoS₂. *J. Am. Chem. Soc.* **2017**, *139*, 10216–10219.10.1021/jacs.7b05765. [[CrossRef](#)] [[PubMed](#)]
98. Mishra, P.; Tangi, M.; Ng, T.K.; Hedhili, M.N.; Anjum, D.H.; Alias, M.S.; Tseng, C.C.; Li, L.J.; Ooi, B.S. Impact of N-plasma and Ga-irradiation on MoS₂ layer in molecular beam epitaxy. *Appl. Phys. Lett.* **2017**, *110*, 012101.10.1063/1.4973371. [[CrossRef](#)]
99. Thiruraman, J.P.; Fujisawa, K.; Danda, G.; Das, P.M.; Zhang, T.; Bolotsky, A.; Perea-López, N.; Nicolai, A.; Senet, P.; Terrones, M.; et al. Angstrom-size defect creation and ionic transport through pores in single-layer MoS₂. *Nano Lett.* **2018**, *18*, 1651–1659.10.1021/acs.nanolett.7b04526. [[CrossRef](#)]
100. Madauß, L.; Ochedowski, O.; Lebius, H.; Ban-d'Etat, B.; Naylor, C.H.; Johnson, A.T.C.; Kotakoski, J.; Schleberger, M. Defect engineering of single- and few-layer MoS₂ by swift heavy ion irradiation. *2D Mater.* **2017**, *4*, 015034.10.1088/2053-1583/4/1/015034. [[CrossRef](#)]
101. Hopster, J.; Kozubek, R.; Krämer, J.; Sokolovsky, V.; Schleberger, M. Ultra-thin MoS₂ irradiated with highly charged ions. *Nucl. Instrum. Methods Phys. Res. Sect. B* **2013**, *317*, 165–169.10.1016/j.nimb.2013.02.038. [[CrossRef](#)]
102. Guo, H.; Sun, Y.; Zhai, P.; Yao, H.; Zeng, J.; Zhang, S.; Duan, J.; Hou, M.; Khan, M.; Liu, J. Swift-heavy ion irradiation-induced latent tracks in few- and mono-layer MoS₂. *Appl. Phys. A* **2016**, *122*, 375.10.1007/s00339-016-9940-y. [[CrossRef](#)]

103. Mignuzzi, S.; Pollard, A.J.; Bonini, N.; Brennan, B.; Gilmore, I.S.; Pimenta, M.A.; Richards, D.; Roy, D. Effect of disorder on Raman scattering of single-layer MoS₂. *Phys. Rev. B* **2015**, *91*, 195411.10.1103/PhysRevB.91.195411. [[CrossRef](#)]
104. Henry, J.; Dunlop, A.; Della-Negra, S. Craters, bumps and onion structures in MoS₂ irradiated with MeV C₆₀ ions. *Nucl. Instrum. Methods Phys. Res. Sect. B* **1998**, *146*, 405–411.10.1016/S0168-583X(98)00516-3. [[CrossRef](#)]
105. Devine, M.J.; Lamson, E.R.; Bowen, J.H. Inorganic solid film lubricants. *J. Chem. Eng. Data* **1961**, *6*, 79–82.10.1021/je60009a018. [[CrossRef](#)]
106. Lee, J.; Krupcale, M.J.; Feng, P.X.L. Effects of γ -ray radiation on two-dimensional molybdenum disulfide (MoS₂) nanomechanical resonators. *Appl. Phys. Lett.* **2016**, *108*, 023106.10.1063/1.4939685. [[CrossRef](#)]
107. Ozden, B.; Khanal, M.P.; Park, J.; Uprety, S.; Mirkhani, V.; Yapabandara, K.; Kim, K.; Kuroda, M.; Bozack, M.J.; Choi, W.; et al. Raman and X-ray photoelectron spectroscopy investigation of the effect of gamma-ray irradiation on MoS₂. *Micro Nano Lett.* **2017**, *12*, 271–274.10.1049/mnl.2016.0712. [[CrossRef](#)]
108. Coleman, A.F.; Flores, R.L.; Xu, Y.Q. Effects of ozone plasma treatment and X-ray irradiation on optical properties of atomically thin molybdenum disulfide. *Young Sci.* **2014**, *4*, 4.10.1016/j.electacta.2018.12.043. [[CrossRef](#)]
109. Azcatl, A.; McDonnell, S.; Santosh, K. C.; Peng, X.; Dong, H.; Qin, X.; Addou, R.; Mordi, G.I.; Lu, N.; Kim, J.; et al. MoS₂ functionalization for ultra-thin atomic layer deposited dielectrics. *Appl. Phys. Lett.* **2014**, *104*, 111601.10.1063/1.4869149. [[CrossRef](#)]
110. McMorro, J.J.; Cress, C.D.; Arnold, H.N.; Sangwan, V.K.; Jariwala, D.; Schmucker, S.W.; Marks, T.J.; Hersam, M.C. Vacuum ultraviolet radiation effects on two-dimensional MoS₂ field-effect transistors. *Appl. Phys. Lett.* **2017**, *110*, 073102.10.1063/1.4976023. [[CrossRef](#)]
111. Gu, E.; Wang, Q.; Zhang, Y.; Cong, C.; Hu, L.; Tian, P.; Liu, R.; Zhang, S.L.; Qiu, Z.J. A real-time Raman spectroscopy study of the dynamics of laser-thinning of MoS₂ flakes to monolayers. *AIP Adv.* **2017**, *7*, 125329.10.1063/1.5008441. [[CrossRef](#)]
112. Lu, J.; Lu, J.H.; Liu, H.; Liu, B.; Chan, K.X.; Lin, J.; Chen, W.; Loh, K.P.; Sow, C.H. Improved photoelectrical properties of MoS₂ films after laser micromachining. *ACS Nano* **2014**, *8*, 6334–6343.10.1021/nn501821z. [[CrossRef](#)] [[PubMed](#)]
113. Paradisanos, I.; Kymakis, E.; Fotakis, C.; Kioseoglou, G.; Stratakis, E. Intense femtosecond photoexcitation of bulk and monolayer MoS₂. *Appl. Phys. Lett.* **2014**, *105*, 041108.10.1063/1.4891679. [[CrossRef](#)]
114. Zhai, P.; Lu, F.; Tang, X.; Wei, J.; He, J.; Shang, G.; Yao, J. Observation of radiation damage of energetic heavy ions impacts on MoS₂ surface by scanning tunneling microscopy. *Sci. China Ser. A* **1993**, *36*, 715–719.10.1360/ya1993-36-6-715. [[CrossRef](#)]
115. Bhattacharya, R.S.; Rai, A.K.; McCormick, A.W.; Erdemir, A. High energy (MeV) ion beam modifications of sputtered MoS₂ coatings on ceramics. *Tribol. Trans.* **1993**, *36*, 621–626.10.1080/10402009308983203. [[CrossRef](#)]
116. Murray, R.; Haynes, K.; Zhao, X.; Perry, S.; Hatem, C.; Jones, K. The effect of low energy ion implantation on MoS₂. *ECS J. Solid State Sci. Technol.* **2016**, *5*, Q3050–Q3053.10.1149/2.0111611jss. [[CrossRef](#)]
117. Chen, Y.; Huang, S.; Ji, X.; Adepalli, K.; Yin, K.; Ling, X.; Wang, X.; Xue, J.; Dresselhaus, M.; Kong, J.; et al. Tuning electronic structure of single layer MoS₂ through defect and interface engineering. *ACS Nano* **2018**, *12*, 2569–2579.10.1021/acsnano.7b08418. [[CrossRef](#)] [[PubMed](#)]
118. Liu, Y.; Nan, H.; Wu, X.; Pan, W.; Wang, W.; Bai, J.; Zhao, W.; Sun, L.; Wang, X.; Ni, Z. Layer-by-layer thinning of MoS₂ by plasma. *ACS Nano* **2013**, *7*, 4202–4209.10.1021/nn400644t. [[CrossRef](#)]
119. Elgqvist, J.; Frost, S.; Pouget, J.P.; Albertsson, P. The potential and hurdles of targeted alpha therapy—Clinical trials and beyond. *Front. Oncol.* **2014**, *3*, 324.10.3389/fonc.2013.00324. [[CrossRef](#)]
120. Sgouros, G.; Hobbs, R.F.; Song, H. Modelling and dosimetry for alpha-particle therapy. *Curr. Radiopharm.* **2011**, *4*, 261–265.10.2174/1874471011104030261. [[CrossRef](#)]
121. Zhang, H.; Maguire, P.; Fox, D.S.; Zhou, Y. Beam exfoliation of MoS₂ layers with a helium ion beam. In Proceedings of the European Microscopy Congress 2016, Lyon, France, 28 August–2 September 2016; p. 1.10.1002/9783527808465.EMC2016.6966. [[CrossRef](#)]
122. Han, S.W.; Park, Y.; Hwang, Y.H.; Jekal, S.; Kang, M.; Lee, W.G.; Yang, W.; Lee, G.D.; Hong, S.C. Electron beam-formed ferromagnetic defects on MoS₂ surface along 1 T phase transition. *Sci. Rep.* **2016**, *6*, 38730.10.1038/srep38730. [[CrossRef](#)] [[PubMed](#)]

123. Komsa, H.P.; Kurasch, S.; Lehtinen, O.; Kaiser, U.; Krashennnikov, A.V. From point to extended defects in two-dimensional MoS₂: Evolution of atomic structure under electron irradiation. *Phys. Rev. B* **2013**, *88*, 035301.10.1103/PhysRevB.88.035301. [[CrossRef](#)]
124. Azcatl, A.; Qin, X.; Prakash, A.; Zhang, C.; Cheng, L.; Wang, Q.; Lu, N.; Kim, M.J.; Kim, J.; Cho, K.; et al. Covalent nitrogen doping and compressive strain in MoS₂ by remote N₂ plasma exposure. *Nano Lett.* **2016**, *16*, 5437–5443.10.1021/acs.nanolett.6b01853. [[CrossRef](#)] [[PubMed](#)]
125. Nan, H.; Wang, Z.; Wang, W.; Liang, Z.; Lu, Y.; Chen, Q.; He, D.; Tan, P.; Miao, F.; Wang, X.; et al. Strong photoluminescence enhancement of MoS₂ through defect engineering and oxygen bonding. *ACS Nano* **2014**, *8*, 5738–5745.10.1021/nn500532f. [[CrossRef](#)] [[PubMed](#)]
126. Chen, M.; Nam, H.; Wi, S.; Ji, L.; Ren, X.; Bian, L.; Lu, S.; Liang, X. Stable few-layer MoS₂ rectifying diodes formed by plasma-assisted doping. *Appl. Phys. Lett.* **2013**, *103*, 142110.10.1063/1.4824205. [[CrossRef](#)]
127. Kang, N.; Paudel, H.P.; Leuenberger, M.N.; Tetard, L.; Khondaker, S.I. Photoluminescence quenching in single-layer MoS₂ via oxygen plasma treatment. *J. Phys. Chem. C* **2014**, *118*, 21258–21263.10.1021/jp506964m. [[CrossRef](#)]
128. Islam, M.R.; Kang, N.; Bhanu, U.; Paudel, H.P.; Erementchouk, M.; Tetard, L.; Leuenberger, M.N.; Khondaker, S.I. Tuning the electrical property via defect engineering of single layer MoS₂ by oxygen plasma. *Nanoscale* **2014**, *6*, 10033–10039.10.1039/C4NR02142H. [[CrossRef](#)]
129. Ye, G.; Gong, Y.; Lin, J.; Li, B.; He, Y.; Pantelides, S.T.; Zhou, W.; Vajtai, R.; Ajayan, P.M. Defects engineered monolayer MoS₂ for improved hydrogen evolution reaction. *Nano Lett.* **2016**, *16*, 1097–1103.10.1021/acs.nanolett.5b04331. [[CrossRef](#)]
130. Dhall, R.; Neupane, M.R.; Wickramaratne, D.; Mecklenburg, M.; Li, Z.; Moore, C.; Lake, R.K.; Cronin, S. Direct bandgap transition in many-layer MoS₂ by plasma-induced layer decoupling. *Adv. Mater.* **2015**, *27*, 1573–1578.10.1002/adma.201405259. [[CrossRef](#)]
131. Kim, M.S.; Nam, G.; Park, S.; Kim, H.; Han, G.H.; Lee, J.; Dhakal, K.P.; Leem, J.Y.; Lee, Y.H.; Kim, J. Photoluminescence wavelength variation of monolayer MoS₂ by oxygen plasma treatment. *Thin Solid Films* **2015**, *590*, 318–323.10.1016/j.tsf.2015.06.024. [[CrossRef](#)]
132. Nipane, A.; Karmakar, D.; Kaushik, N.; Karande, S.; Lodha, S. Few-layer MoS₂ *p*-type devices enabled by selective doping using low energy phosphorus implantation. *ACS Nano* **2016**, *10*, 2128–2137.10.1021/acs.nano.5b06529. [[CrossRef](#)] [[PubMed](#)]
133. Jadwiszczak, J.; O’Callaghan, C.; Zhou, Y.; Fox, D.S.; Weitz, E.; Keane, D.; Cullen, C.P.; O’Reilly, I.; Downing, C.; Shmeliov, A.; et al. Oxide-mediated recovery of field-effect mobility in plasma-treated MoS₂. *Sci. Adv.* **2018**, *4*, eaao5031.10.1126/sciadv.aao5031. [[CrossRef](#)]
134. Bhimanapati, G.R.; Hankins, T.; Lei, Y.; Vilá, R.A.; Fuller, I.; Terrones, M.; Robinson, J.A. Growth and tunable surface wettability of vertical MoS₂ layers for improved hydrogen evolution reactions. *ACS Appl. Mater. Interfaces* **2016**, *8*, 22190–22195.10.1021/acsami.6b05848. [[CrossRef](#)]
135. Zhang, C.X.; Newaz, A.K.M.; Wang, B.; Zhang, E.X.; Duan, G.X.; Fleetwood, D.M.; Alles, M.L.; Schrimpf, R.D.; Bolotin, K.I.; Pantelides, S.T. Electrical stress and total ionizing dose effects on MoS₂ transistors. *IEEE Trans. Nucl. Sci.* **2014**, *61*, 2862–2867.10.1109/TNS.2014.2365522. [[CrossRef](#)]
136. Li, J.; Wierzbowski, J.; Ceylan, O.; Klein, J.; Nisic, F.; Anh, T.L.; Meggendorfer, F.; Palma, C.A.; Dragonetti, C.; Barth, J.V.; et al. Tuning the optical emission of MoS₂ nanosheets using proximal photoswitchable azobenzene molecules. *Appl. Phys. Lett.* **2014**, *105*, 241116.10.1063/1.4904824. [[CrossRef](#)]
137. Lu, X.; Wang, R.; Hao, L.; Yang, F.; Jiao, W.; Peng, P.; Yuan, F.; Liu, W. Oxidative etching of MoS₂/WS₂ nanosheets to their QDs by facile UV irradiation. *Phys. Chem. Chem. Phys.* **2016**, *18*, 31211–31216.10.1039/C6CP06748D. [[CrossRef](#)] [[PubMed](#)]
138. Singh, A.K.; Andleeb, S.; Singh, J.; Eom, J. Tailoring the electrical properties of multilayer MoS₂ transistors using ultraviolet light irradiation. *RSC Adv.* **2015**, *5*, 77014–77018.10.1039/C5RA14509K. [[CrossRef](#)]
139. Singh, A.K.; Andleeb, S.; Singh, J.; Dung, H.T.; Seo, Y.; Eom, J. Ultraviolet-light-induced reversible and stable carrier modulation in MoS₂ field-effect transistors. *Adv. Funct. Mater.* **2014**, *24*, 7125–7132.10.1002/adfm.201402231. [[CrossRef](#)]
140. Liu, P.; Liu, Y.; Ye, W.; Ma, J.; Gao, D. Flower-like N-doped MoS₂ for photocatalytic degradation of RhB by visible light irradiation. *Nanotechnology* **2016**, *27*, 225403.10.1088/0957-4484/27/22/225403. [[CrossRef](#)]

141. Castellanos-Gomez, A.; Barkelid, M.; Goossens, A.M.; Calado, V.E.; van der Zant, H.S.J.; Steele, G.A. Laser-thinning of MoS₂: On demand generation of a single-layer semiconductor. *Nano Lett.* **2012**, *12*, 3187–3192.10.1021/nl301164v. [[CrossRef](#)]
142. Yoo, J.H.; Kim, E.; Hwang, D.J. Femtosecond laser patterning, synthesis, defect formation, and structural modification of atomic layered materials. *MRS Bull.* **2016**, *41*, 1002–1008.10.1557/mrs.2016.248. [[CrossRef](#)]
143. Pan, Y.; Yang, M.; Li, Y.; Wang, Z.; Zhang, C.; Zhao, Y.; Yao, J.; Wu, Q.; Xu, J. Threshold dependence of deep- and near-subwavelength ripples formation on natural MoS₂ induced by femtosecond laser. *Sci. Rep.* **2016**, *6*, 19571.10.1038/srep19571;. [[CrossRef](#)] [[PubMed](#)]
144. Windom, B.C.; Sawyer, W.G.; Hahn, D.W. A Raman spectroscopic study of MoS₂ and MoO₃: Applications to tribological systems. *Tribol. Lett.* **2011**, *42*, 301–310.10.1007/s11249-011-9774-x. [[CrossRef](#)]
145. Tran Khac, B.C.; Jeon, K.J.; Choi, S.T.; Kim, Y.S.; DelRio, F.W.; Chung, K.H. Laser-induced particle adsorption on atomically thin MoS₂. *ACS Appl. Mater. Interfaces* **2016**, *8*, 2974–2984.10.1021/acsami.5b09382. [[CrossRef](#)] [[PubMed](#)]
146. Alrasheed, A.; Gorham, J.M.; Tran Khac, B.C.; Alsaffar, F.; DelRio, F.W.; Chung, K.H.; Amer, M.R. Surface properties of laser-treated molybdenum disulfide nanosheets for optoelectronic applications. *ACS Appl. Mater. Interfaces* **2018**, *10*, 18104–18112.10.1021/acsami.8b04717. [[CrossRef](#)] [[PubMed](#)]
147. Goswami, A.; Dhandaria, P.; Pal, S.; McGee, R.; Khan, F.; Antić, Ž.; Gaikwad, R.; Prashanthi, K.; Thundat, T. Effect of interface on mid-infrared photothermal response of MoS₂ thin film grown by pulsed laser deposition. *Nano Res.* **2017**, *10*, 3571–3584.10.1007/s12274-017-1568-5. [[CrossRef](#)]
148. Cao, Y.; Gan, S.; Geng, Z.; Liu, J.; Yang, Y.; Bao, Q.; Chen, H. Optically tuned terahertz modulator based on annealed multilayer MoS₂. *Sci. Rep.* **2016**, *6*, 22899.10.1038/srep22899. [[CrossRef](#)]
149. Docherty, C.J.; Parkinson, P.; Joyce, H.J.; Chiu, M.H.; Chen, C.H.; Lee, M.Y.; Li, L.J.; Herz, L.M.; Johnston, M.B. Ultrafast transient terahertz conductivity of monolayer MoS₂ and WSe₂ grown by chemical vapor deposition. *ACS Nano* **2014**, *8*, 11147–11153.10.1021/nn5034746. [[CrossRef](#)]
150. Arcos, D.; Gabriel, D.; Dumcenco, D.; Kis, A.; Ferrer-Anglada, N. THz time-domain spectroscopy and IR spectroscopy on MoS₂. *Phys. Status Solidi (b)* **2016**, *253*, 2499–2504.10.1002/pssb.201600281. [[CrossRef](#)]
151. Deng, X.Y.; Deng, X.H.; Su, F.H.; Liu, N.H.; Liu, J.T. Broadband ultra-high transmission of terahertz radiation through monolayer MoS₂. *J. Appl. Phys.* **2015**, *118*, 224304.10.1063/1.4937276. [[CrossRef](#)]
152. Lee, J.; Wang, Z.; He, K.; Yang, R.; Shan, J.; Feng, P.X.L. Electrically tunable single- and few-layer MoS₂ nanoelectromechanical systems with broad dynamic range. *Sci. Adv.* **2018**, *4*, ea06653.10.1126/sciadv.aao6653. [[CrossRef](#)] [[PubMed](#)]
153. Krasnozhan, D.; Lembke, D.; Nyffeler, C.; Leblebici, Y.; Kis, A. MoS₂ transistors operating at gigahertz frequencies. *Nano Lett.* **2014**, *14*, 5905–5911.10.1021/nl5028638. [[CrossRef](#)]
154. Cheng, R.; Jiang, S.; Chen, Y.; Liu, Y.; Weiss, N.; Cheng, H.C.; Wu, H.; Huang, Y.; Duan, X. Few-layer molybdenum disulfide transistors and circuits for high-speed flexible electronics. *Nat. Commun.* **2014**, *5*, 5143.10.1038/ncomms6143. [[CrossRef](#)] [[PubMed](#)]
155. Zhang, X.; Hayward, D.O.; Lee, C.; Mingos, D.M.P. Microwave assisted catalytic reduction of sulfur dioxide with methane over MoS₂ catalysts. *Appl. Catal. B* **2001**, *33*, 137–148.10.1016/S0926-3373(01)00171-0. [[CrossRef](#)]
156. Zhao, H.; Mu, X.; Yang, G.; Zheng, C.; Sun, C.; Gao, X.; Wu, T. Microwave-induced activation of additional active edge sites on the MoS₂ surface for enhanced Hg⁰ capture. *Appl. Surf. Sci.* **2017**, *420*, 439–445.10.1016/j.apsusc.2017.05.161. [[CrossRef](#)]
157. Gao, D.; Si, M.; Li, J.; Zhang, J.; Zhang, Z.; Yang, Z.; Xue, D. Ferromagnetism in freestanding MoS₂ nanosheets. *Nanoscale Res. Lett.* **2013**, *8*, 129.10.1186/1556-276X-8-129. [[CrossRef](#)] [[PubMed](#)]
158. Mdleleni, M.M.; Hyeon, T.; Suslick, K.S. Sonochemical synthesis of nanostructured molybdenum sulfide. *J. Am. Chem. Soc.* **1998**, *120*, 6189–6190.10.1021/ja9800333. [[CrossRef](#)]
159. Pető, J.; Ollár, T.; Vancsó, P.; Popov, Z.I.; Magda, G.Z.; Dobrik, G.; Hwang, C.; Sorokin, P.B.; Tapasztó, L. Spontaneous doping of the basal plane of MoS₂ single layers through oxygen substitution under ambient conditions. *Nat. Chem.* **2018**, *10*, 1246–1251.10.1038/s41557-018-0136-2. [[CrossRef](#)]
160. Donarelli, M.; Bisti, F.; Perrozzi, F.; Ottaviano, L. Tunable sulfur desorption in exfoliated MoS₂ by means of thermal annealing in ultra-high vacuum. *Chem. Phys. Lett.* **2013**, *588*, 198–202.10.1016/j.cplett.2013.10.034. [[CrossRef](#)]

161. Yamamoto, M.; Einstein, T.L.; Fuhrer, M.S.; Cullen, W.G. Anisotropic etching of atomically thin MoS₂. *J. Phys. Chem. C* **2013**, *117*, 25643–25649.10.1021/jp410893e. [[CrossRef](#)]
162. Tongay, S.; Zhou, J.; Ataca, C.; Liu, J.; Kang, J.S.; Matthews, T.S.; You, L.; Li, J.; Grossman, J.C.; Wu, J. Broad-range modulation of light emission in two-dimensional semiconductors by molecular physisorption gating. *Nano Lett.* **2013**, *13*, 2831–2836.10.1021/nl4011172. [[CrossRef](#)] [[PubMed](#)]
163. Yang, H.I.; Park, S.; Choi, W. Modification of the optoelectronic properties of two-dimensional MoS₂ crystals by ultraviolet-ozone treatment. *Appl. Surf. Sci.* **2018**, *443*, 91–96.10.1016/j.apsusc.2018.02.256. [[CrossRef](#)]
164. Wang, J.; Li, S.; Zou, X.; Ho, J.; Liao, L.; Xiao, X.; Jiang, C.; Hu, W.; Wang, J.; Li, J. Integration of high-*k* oxide on MoS₂ by using ozone pretreatment for high-performance MoS₂ top-gated transistor with thickness-dependent carrier scattering investigation. *Small* **2015**, *11*, 5932–5938.10.1002/sml.201501260. [[CrossRef](#)] [[PubMed](#)]
165. Le, Q.V.; Nguyen, T.P.; Jang, H.W.; Kim, S.Y. The use of UV/ozone-treated MoS₂ nanosheets for extended air stability in organic photovoltaic cells. *Phys. Chem. Chem. Phys.* **2014**, *16*, 13123–13128.10.1039/C4CP01598C. [[CrossRef](#)] [[PubMed](#)]
166. Su, W.; Kumar, N.; Spencer, S.J.; Dai, N.; Roy, D. Transforming bilayer MoS₂ into single-layer with strong photoluminescence using UV-ozone oxidation. *Nano Res.* **2015**, *8*, 3878–3886.10.1007/s12274-015-0887-7. [[CrossRef](#)]
167. Burman, D.; Ghosh, R.; Santra, S.; Ray, S.K.; Guha, P.K. Role of vacancy sites and UV-ozone treatment on few layered MoS₂ nanoflakes for toxic gas detection. *Nanotechnology* **2017**, *28*, 435502.10.1088/1361-6528/aa87cd. [[CrossRef](#)]
168. Kretschmer, S.; Maslov, M.; Ghaderzadeh, S.; Ghorbani-Asl, M.; Hlawacek, G.; Krasheninnikov, A.V. Supported two-dimensional materials under ion irradiation: The substrate governs defect production. *ACS Appl. Mater. Interfaces* **2018**, *10*, 30827–30836.10.1021/acsami.8b08471. [[CrossRef](#)]
169. Ghorbani-Asl, M.; Kretschmer, S.; Spearot, D.E.; Krasheninnikov, A.V. Two-dimensional MoS₂ under ion irradiation: From controlled defect production to electronic structure engineering. *2D Mater.* **2017**, *4*, 025078.10.1088/2053-1583/aa6b17. [[CrossRef](#)]
170. Kobayashi, K.; Yamauchi, J. Electronic structure and scanning-tunneling-microscopy image of molybdenum dichalcogenide surfaces. *Phys. Rev. B* **1995**, *51*, 17085–17095.10.1103/PhysRevB.51.17085. [[CrossRef](#)]
171. Gusakova, J.; Wang, X.; Shiau, L.L.; Krivosheeva, A.; Shaposhnikov, V.; Borisenko, V.; Gusakov, V.; Tay, B.K. Electronic properties of bulk and monolayer TMDs: Theoretical study within DFT framework (GVJ-2e Method). *Phys. Status Solidi* **2017**, *214*, 1700218.10.1002/pssa.201700218. [[CrossRef](#)]
172. Sundaram, R.S.; Engel, M.; Lombardo, A.; Krupke, R.; Ferrari, A.C.; Avouris, P.; Steiner, M. Electroluminescence in single layer MoS₂. *Nano Lett.* **2013**, *13*, 1416–1421.10.1021/nl400516a. [[CrossRef](#)] [[PubMed](#)]
173. Ghorbani-Asl, M.; Enyashin, A.N.; Kuc, A.; Seifert, G.; Heine, T. Defect-induced conductivity anisotropy in MoS₂ monolayers. *Phys. Rev. B* **2013**, *88*, 245440.10.1103/PhysRevB.88.245440. [[CrossRef](#)]
174. Durand, C.; Zhang, X.; Fowlkes, J.; Najmaei, S.; Lou, J.; Li, A.P. Defect-mediated transport and electronic irradiation effect in individual domains of CVD-grown monolayer MoS₂. *J. Vac. Sci. Technol. B* **2015**, *33*, 02B110.10.1116/1.4906331. [[CrossRef](#)]
175. Lu, M.Y.; Wu, S.C.; Wang, H.C.; Lu, M.P. Time-evolution of the electrical characteristics of MoS₂ field-effect transistors after electron beam irradiation. *Phys. Chem. Chem. Phys.* **2018**, *20*, 9038–9044.10.1039/C8CP00792F. [[CrossRef](#)] [[PubMed](#)]
176. Voiry, D.; Salehi, M.; Silva, R.; Fujita, T.; Chen, M.; Asefa, T.; Shenoy, V.B.; Eda, G.; Chhowalla, M. Conducting MoS₂ nanosheets as catalysts for hydrogen evolution reaction. *Nano Lett.* **2013**, *13*, 6222–6227.10.1021/nl403661s. [[CrossRef](#)] [[PubMed](#)]
177. Geng, X.; Sun, W.; Wu, W.; Chen, B.; Al-Hilo, A.; Benamara, M.; Zhu, H.; Watanabe, F.; Cui, J.; Chen, T.P. Pure and stable metallic phase molybdenum disulfide nanosheets for hydrogen evolution reaction. *Nat. Commun.* **2016**, *7*, 10672.10.1038/ncomms10672. [[CrossRef](#)]
178. Shen, Y.; Ren, X.; Qi, X.; Zhou, J.; Huang, Z.; Zhong, J. MoS₂ nanosheet loaded with TiO₂ nanoparticles: An efficient electrocatalyst for hydrogen evolution reaction. *J. Electrochem. Soc.* **2016**, *163*, H1087–H1090.10.1149/2.1181613jes. [[CrossRef](#)]
179. Kim, Y.; Jackson, D.H.K.; Lee, D.; Choi, M.; Kim, T.W.; Jeong, S.Y.; Chae, H.J.; Kim, H.W.; Park, N.; Chang, H.; et al. In situ electrochemical activation of atomic layer deposition coated MoS₂ basal planes

- for efficient hydrogen evolution reaction. *Adv. Funct. Mater.* **2017**, *27*, 1701825.10.1002/adfm.201701825. [[CrossRef](#)]
180. Zong, X.; Yan, H.; Wu, G.; Ma, G.; Wen, F.; Wang, L.; Li, C. Enhancement of photocatalytic H₂ evolution on CdS by loading MoS₂ as cocatalyst under visible light irradiation. *J. Am. Chem. Soc.* **2008**, *130*, 7176–7177.10.1021/ja8007825. [[CrossRef](#)]
181. Hinnemann, B.; Moses, P.G.; Bonde, J.; Jørgensen, K.P.; Nielsen, J.H.; Horch, S.; Chorkendorff, I.; Nørskov, J.K. Biomimetic hydrogen evolution: MoS₂ nanoparticles as catalyst for hydrogen evolution. *J. Am. Chem. Soc.* **2005**, *127*, 5308–5309.10.1021/ja0504690. [[CrossRef](#)]
182. Liu, C.; Kong, D.; Hsu, P.C.; Yuan, H.; Lee, H.W.; Liu, Y.; Wang, H.; Wang, S.; Yan, K.; Lin, D.; et al. Rapid water disinfection using vertically aligned MoS₂ nanofilms and visible light. *Nat. Nanotechnol.* **2016**, *11*, 1098–1104.10.1038/nnano.2016.138. [[CrossRef](#)] [[PubMed](#)]
183. Tao, L.; Duan, X.; Wang, C.; Duan, X.; Wang, S. Plasma-engineered MoS₂ thin-film as an efficient electrocatalyst for hydrogen evolution reaction. *Chem. Commun.* **2015**, *51*, 7470–7473.10.1039/C5CC01981H. [[CrossRef](#)]
184. Tongay, S.; Varnoosfaderani, S.S.; Appleton, B.R.; Wu, J.; Hebard, A.F. Magnetic properties of MoS₂: Existence of ferromagnetism. *Appl. Phys. Lett.* **2012**, *101*, 123105.10.1063/1.4753797. [[CrossRef](#)]
185. Zhang, J.; Soon, J.M.; Loh, K.P.; Yin, J.; Ding, J.; Sullivan, M.B.; Wu, P. Magnetic molybdenum disulfide nanosheet films. *Nano Lett.* **2007**, *7*, 2370–2376.10.1021/nl071016r. [[CrossRef](#)] [[PubMed](#)]
186. Li, Y.; Zhou, Z.; Zhang, S.; Chen, Z. MoS₂ nanoribbons: High stability and unusual electronic and magnetic properties. *J. Am. Chem. Soc.* **2008**, *130*, 16739–16744.10.1021/ja805545x. [[CrossRef](#)] [[PubMed](#)]
187. Botello-Méndez, A.R.; López-Urías, F.; Terrones, M.; Terrones, H. Metallic and ferromagnetic edges in molybdenum disulfide nanoribbons. *Nanotechnology* **2009**, *20*, 325703.10.1088/0957-4484/20/32/325703. [[CrossRef](#)]
188. Shidpour, R.; Manteghian, M. A density functional study of strong local magnetism creation on MoS₂ nanoribbon by sulfur vacancy. *Nanoscale* **2010**, *2*, 1429–1435.10.1039/B9NR00368A. [[CrossRef](#)] [[PubMed](#)]
189. Murugan, P.; Kumar, V.; Kawazoe, Y.; Ota, N. Atomic structures and magnetism in small MoS₂ and WS₂ clusters. *Phys. Rev. A* **2005**, *71*, 063203.10.1103/PhysRevA.71.063203. [[CrossRef](#)]
190. Vojvodic, A.; Hinnemann, B.; Nørskov, J.K. Magnetic edge states in MoS₂ characterized using density-functional theory. *Phys. Rev. B* **2009**, *80*, 125416.10.1103/PhysRevB.80.125416. [[CrossRef](#)]
191. Pan, H.; Zhang, Y.W. Tuning the electronic and magnetic properties of MoS₂ nanoribbons by strain engineering. *J. Phys. Chem. C* **2012**, *116*, 11752–11757.10.1021/jp3015782. [[CrossRef](#)]
192. Zhang, R.; Li, Y.; Qi, J.; Gao, D. Ferromagnetism in ultrathin MoS₂ nanosheets: From amorphous to crystalline. *Nanoscale Res. Lett.* **2014**, *9*, 586.10.1186/1556-276X-9-586. [[CrossRef](#)] [[PubMed](#)]
193. Cai, L.; He, J.; Liu, Q.; Yao, T.; Chen, L.; Yan, W.; Hu, F.; Jiang, Y.; Zhao, Y.; Hu, T.; et al. Vacancy-induced ferromagnetism of MoS₂ nanosheets. *J. Am. Chem. Soc.* **2015**, *137*, 2622–2627.10.1021/ja5120908. [[CrossRef](#)] [[PubMed](#)]
194. Tsai, M.L.; Su, S.H.; Chang, J.K.; Tsai, D.S.; Chen, C.H.; Wu, C.I.; Li, L.J.; Chen, L.J.; He, J.H. Monolayer MoS₂ heterojunction solar cells. *ACS Nano* **2014**, *8*, 8317–8322.10.1021/nn502776h. [[CrossRef](#)] [[PubMed](#)]
195. Hao, L.Z.; Gao, W.; Liu, Y.J.; Han, Z.D.; Xue, Q.Z.; Guo, W.Y.; Zhu, J.; Li, Y.R. High-performance n-MoS₂/i-SiO₂/p-Si heterojunction solar cells. *Nanoscale* **2015**, *7*, 8304–8308.10.1039/C5NR01275A. [[CrossRef](#)] [[PubMed](#)]
196. Pradhan, S.K.; Xiao, B.; Pradhan, A.K. Enhanced photo-response in p-Si/MoS₂ heterojunction-based solar cells. *Sol. Energy Mater. Sol. Cells* **2016**, *144*, 117–127.10.1016/j.solmat.2015.08.021. [[CrossRef](#)]
197. Chen, Y.; Song, B.; Tang, X.; Lu, L.; Xue, J. Ultrasmall Fe₃O₄ nanoparticle/MoS₂ nanosheet composites with superior performances for lithium ion batteries. *Small* **2013**, *10*, 1536–1543.10.1002/smll.201302879. [[CrossRef](#)] [[PubMed](#)]
198. Veeramalai, C.P.; Li, F.; Xu, H.; Kim, T.W.; Guo, T. One pot hydrothermal synthesis of graphene like MoS₂ nanosheets for application in high performance lithium ion batteries. *RSC Adv.* **2015**, *5*, 57666–57670.10.1039/C5RA07478A. [[CrossRef](#)]
199. Wang, L.; Ma, Y.; Yang, M.; Qi, Y. Titanium plate supported MoS₂ nanosheet arrays for supercapacitor application. *Appl. Surf. Sci.* **2017**, *396*, 1466–1471.10.1016/j.apsusc.2016.11.193. [[CrossRef](#)]

200. Qiu, H.; Pan, L.; Yao, Z.; Li, J.; Shi, Y.; Wang, X. Electrical characterization of back-gated bi-layer MoS₂ field-effect transistors and the effect of ambient on their performances. *Appl. Phys. Lett.* **2012**, *100*, 123104.10.1063/1.3696045. [CrossRef]
201. Pu, J.; Yomogida, Y.; Liu, K.K.; Li, L.J.; Iwasa, Y.; Takenobu, T. Highly flexible MoS₂ thin-film transistors with ion gel dielectrics. *Nano Lett.* **2012**, *12*, 4013–4017.10.1021/nl301335q. [CrossRef]
202. Liu, H.; Neal, A.T.; Ye, P.D. Channel length scaling of MoS₂ MOSFETs. *ACS Nano* **2012**, *6*, 8563–8569.10.1021/nn303513c. [CrossRef] [PubMed]
203. Radisavljevic, B.; Kis, A. Mobility engineering and a metal–insulator transition in monolayer MoS₂. *Nat. Mater.* **2013**, *12*, 815–820.10.1038/nmat3687. [CrossRef] [PubMed]
204. Farimani, A.B.; Min, K.; Aluru, N.R. DNA base detection using a single-layer MoS₂. *ACS Nano* **2014**, *8*, 7914–7922.10.1021/nn5029295. [CrossRef]
205. Bertolazzi, S.; Bonacchi, S.; Nan, G.; Pershin, A.; Beljonne, D.; Samori, P. Engineering chemically active defects in monolayer MoS₂ transistors via ion-beam irradiation and their healing via vapor deposition of alkanethiols. *Adv. Mater.* **2017**, *29*, 1606760.10.1002/adma.201606760. [CrossRef] [PubMed]
206. Li, H.; Yin, Z.; He, Q.; Li, H.; Huang, X.; Lu, G.; Fam, D.W.H.; Tok, A.I.Y.; Zhang, Q.; Zhang, H. Fabrication of single- and multilayer MoS₂ film-based field-effect transistors for sensing NO at room temperature. *Small* **2011**, *8*, 63–67.10.1002/sml.201101016. [CrossRef]
207. Late, D.J.; Huang, Y.K.; Liu, B.; Acharya, J.; Shirodkar, S.N.; Luo, J.; Yan, A.; Charles, D.; Waghmare, U.V.; Dravid, V.P.; et al. Sensing behavior of atomically thin-layered MoS₂ transistors. *ACS Nano* **2013**, *7*, 4879–4891.10.1021/nn400026u. [CrossRef] [PubMed]
208. Lee, K.; Gatensby, R.; McEvoy, N.; Hallam, T.; Duesberg, G.S. High-performance sensors based on molybdenum disulfide thin films. *Adv. Mater.* **2013**, *25*, 6699–6702.10.1002/adma.201303230. [CrossRef]
209. Huang, J.; Dong, Z.; Li, Y.; Li, J.; Tang, W.; Yang, H.; Wang, J.; Bao, Y.; Jin, J.; Li, R. MoS₂ nanosheet functionalized with Cu nanoparticles and its application for glucose detection. *Mater. Res. Bull.* **2013**, *48*, 4544–4547.10.1016/j.materresbull.2013.07.060. [CrossRef]
210. Ramanathan, A.A. Defect Functionalization of MoS₂ nanostructures as toxic gas sensors: A review. *IOP Conf. Ser. Mater. Sci. Eng.* **2018**, *305*, 012001.10.1088/1757-899X/305/1/012001. [CrossRef]
211. Wang, H.; Lu, Z.; Xu, S.; Kong, D.; Cha, J.J.; Zheng, G.; Hsu, P.C.; Yan, K.; Bradshaw, D.; Prinz, F.B.; et al. Electrochemical tuning of vertically aligned MoS₂ nanofilms and its application in improving hydrogen evolution reaction. *Proc. Natl. Acad. Sci. USA* **2013**, *110*, 19701–19706.10.1073/pnas.1316792110. [CrossRef]
212. Hai, X.; Zhou, W.; Wang, S.; Pang, H.; Chang, K.; Ichihara, F.; Ye, J. Rational design of freestanding MoS₂ monolayers for hydrogen evolution reaction. *Nano Energy* **2017**, *39*, 409–417.10.1016/j.nanoen.2017.07.021. [CrossRef]
213. Buscema, M.; Barkelid, M.; Zwiller, V.; van der Zant, H.S.J.; Steele, G.A.; Castellanos-Gomez, A. Large and tunable photothermoelectric effect in single-layer MoS₂. *Nano Lett.* **2013**, *13*, 358–363.10.1021/nl303321g. [CrossRef] [PubMed]
214. Wu, J.; Schmidt, H.; Amara, K.K.; Xu, X.; Eda, G.; Özyilmaz, B. Large thermoelectricity via variable range hopping in chemical vapor deposition grown single-layer MoS₂. *Nano Lett.* **2014**, *14*, 2730–2734.10.1021/nl500666m. [CrossRef] [PubMed]
215. Huang, W.; Luo, X.; Gan, C.K.; Quek, S.Y.; Liang, G. Theoretical study of thermoelectric properties of few-layer MoS₂ and WSe₂. *Phys. Chem. Chem. Phys.* **2014**, *16*, 10866–10874.10.1039/C4CP00487F. [CrossRef] [PubMed]
216. Arab, A.; Li, Q. Anisotropic thermoelectric behavior in armchair and zigzag mono- and fewlayer MoS₂ in thermoelectric generator applications. *Sci. Rep.* **2015**, *5*, 13706.10.1038/srep13706. [CrossRef] [PubMed]
217. Xiong, P.; Ao, X.; Chen, J.; Li, J.G.; Lv, L.; Li, Z.; Zondode, M.; Xue, X.; Lan, Y.; Wang, C. Nickel diselenide nanoflakes give superior urea electrocatalytic conversion. *Electrochim. Acta* **2019**, *297*, 833–841.10.1016/j.electacta.2018.12.043. [CrossRef]
218. Zhou, H.; Yu, F.; Sun, J.; He, R.; Wang, Y.; Guo, C.F.; Wang, F.; Lan, Y.; Ren, Z.; Chen, S. Highly active and durable self-standing WS₂/graphene hybrid catalysts for the hydrogen evolution reaction. *J. Mater. Chem. A* **2016**, *4*, 9472–9476.10.1039/C6TA02876D. [CrossRef]
219. Zhang, J.; Lv, L.; Tian, Y.; Li, Z.; Ao, X.; Lan, Y.; Jiang, J.; Wang, C. Rational design of cobalt-iron selenides for highly efficient electrochemical water oxidation. *ACS Appl. Mater. Interfaces* **2017**, *9*, 33833–33840.10.1021/acsami.7b08917. [CrossRef]

220. Li, Z.; Lv, L.; Wang, J.; Ao, X.; Ruan, Y.; Zha, D.; Hong, G.; Wu, Q.; Lan, Y.; Wang, C.; et al. Engineering phosphorus-doped $\text{LaFeO}_{3-\delta}$ perovskite oxide as robust bifunctional oxygen electrocatalysts in alkaline solutions. *Nano Energy* **2018**, *47*, 199–209.10.1016/j.nanoen.2018.02.051. [CrossRef]
221. Wang, A.; Wang, C.; Fu, L.; Wong-Ng, W.; Lan, Y. Recent advances of graphitic carbon nitride-based structures and applications in catalyst, sensing, imaging, and LEDs. *Nano-Micro Lett.* **2017**, *9*, 47.10.1007/s40820-017-0148-2. [CrossRef]
222. Lv, L.; Xu, K.; Wang, C.; Wan, H.; Ruan, Y.; Liu, J.; Zou, R.; Miao, L.; Ostrikov, K.K.; Lan, Y.; et al. Intercalation of glucose in NiMn-layered double hydroxides nanosheets: An effective path way towards battery-type electrodes with enhanced performance. *Electrochim. Acta* **2016**, *216*, 35–43.10.1016/j.electacta.2016.08.149. [CrossRef]
223. Lan, Y.; Lu, Y.; Ren, Z. Mini review on photocatalysis of titanium dioxide nanoparticles and their solar applications. *Nano Energy* **2013**, *2*, 1031–1045.10.1016/j.nanoen.2013.04.002. [CrossRef]
224. Lan, Y.; Minnich, A.J.; Chen, G.; Ren, Z. Enhancement of thermoelectric figure-of-merit by a bulk nanostructuring approach. *Adv. Funct. Mater.* **2010**, *20*, 357–376.10.1002/adfm.200901512. [CrossRef]
225. Dampare, J.; Zondode, M.; Liou, S.C.; Ozturk, B.; Yu, H.; Lan, Y. EELS investigations of carbon-rich boron carbide nanomaterials. *Microsc. Microanal.* **2018**, *24*, 1756–1757.10.1017/S1431927618009261. [CrossRef]
226. Lan, Y.; Wang, Y.; Ren, Z.F. Physics and applications of aligned carbon nanotubes. *Adv. Phys.* **2011**, *60*, 553–678.10.1080/00018732.2011.599963. [CrossRef]
227. Cao, Q.; Geng, X.; Wang, H.; Wang, P.; Liu, A.; Lan, Y.; Peng, Q. A review of current development of graphene mechanics. *Crystals* **2018**, *8*, 357.10.3390/cryst8090357. [CrossRef]
228. Lan, Y.; Zondode, M.; Deng, H.; Yan, J.A.; Ndaw, M.; Lisfi, A.; Wang, C.; Pan, Y.L. Basic concepts and recent advances of crystallographic orientation determination of graphene by Raman spectroscopy. *Crystals* **2018**, *8*, 375.10.3390/cryst8100375. [CrossRef]
229. Zhou, H.; Wang, Y.; He, R.; Yu, F.; Sun, J.; Wang, F.; Lan, Y.; Ren, Z.; Chen, S. One-step synthesis of self-supported porous NiSe_2/Ni hybrid foam: An efficient 3D electrode for hydrogen evolution reaction. *Nano Energy* **2016**, *20*, 29–36.10.1016/j.nanoen.2015.12.008. [CrossRef]
230. Guo, C.F.; Lan, Y.; Sun, T.; Ren, Z. Deformation-induced cold-welding for self-healing of super-durable flexible transparent electrodes. *Nano Energy* **2014**, *8*, 110–117.10.1016/j.nanoen.2014.05.011. [CrossRef]



© 2019 by the authors. Licensee MDPI, Basel, Switzerland. This article is an open access article distributed under the terms and conditions of the Creative Commons Attribution (CC BY) license (<http://creativecommons.org/licenses/by/4.0/>).